

Abstract

Novel Pulse Sequences Exploiting the Effects of Hard π -pulses

Rona G. Ramos

2010

In magnetic resonance and other spectroscopies, the strong pulses used to control coherent spin evolution are often approximated as instantaneous delta function rotations. However, small corrections to the delta function model can cause surprising departures from the conventional theory in standard multipulse NMR experiments using strong π -pulses. In this dissertation, we report the exploration of the small correction terms resulting from the finite duration of realistic pulses, however strong, using average Hamiltonian theory. Investigation of role these terms could play in standard NMR experiments led to the design and demonstration of a new class of spin echoes. We present analogs of the original free induction decay (FID), Hahn echo, and CPMG echoes whose experimental design is based on terms typically ignored when strong pulses are used. Variants on the original magic echo are demonstrated as well as the quadratic echo, based on both the zeroth- and first-order average Hamiltonian expressions and which has no classic NMR spin echo analog. Finally, we present alternative approaches to overcoming the line broadening effect of dipolar interactions in solids. Using a variation on the quadratic echo pulse sequence as a building block, we develop a new approach to line-narrowing and magnetic resonance imaging of solids which allows control of both the Zeeman and dipolar phase wrapping.

Novel Pulse Sequences Exploiting the Effects of Hard π -pulses

A Dissertation
Presented to the Faculty of the Graduate School
of
Yale University
in Candidacy for the Degree of
Doctor of Philosophy

by
Rona G. Ramos

Dissertation Director: Professor Sean E. Barrett

April 2010

© 2010 by Rona G. Ramos

All rights reserved.

Contents

Table of Contents	iii
List of Figures	v
List of Tables	vii
Glossary of Symbols and Acronyms	viii
Words of Acknowledgment	xiii
Introduction	1
1 Spin Basics	5
1.1 Classical Spins	6
1.1.1 Larmor Precession	6
1.1.2 The Rotating Frame	7
1.1.3 Bloch Equations and Spin Relaxation	8
1.2 Quantum Mechanical Spins	9
1.2.1 Larmor Frequency	10
1.2.2 Quantum Mechanical Equation of Motion	11
1.2.3 Density Matrix Representation	11

2	NMR Experimental Details	14
2.1	Pulsed NMR Spectrometer	14
2.1.1	Transmitter	15
2.1.2	Receiver	15
2.2	Tank Circuits	16
2.3	Superconducting Magnet	18
3	NMR Measurements and Unexpected Spin Echoes	21
3.1	Unexpected Echoes	21
3.2	Internal Hamiltonian	23
3.2.1	Zeeman Hamiltonian	23
3.2.2	Dipolar Hamiltonian	24
3.3	Delta Function Pulse Approximation	26
3.4	Measuring T_2	27
3.4.1	Hahn Echo Two Pulse Sequence	27
3.4.2	Carr-Purcell-Meiboom-Gill Multiple π -Pulse Sequence	30
3.5	More Unexpected Echoes with Multiple Pulse Experiments	32
3.5.1	Even-odd Effect	33
3.5.2	Pulse Sequence Sensitivity	35
3.6	Beyond the Delta Function Approximation	37
3.6.1	Experimental Sources	37
3.6.2	Exact Calculations for Finite Pulses	43
3.6.3	Finding the Long Tail in Simulations	46
4	Average Hamiltonian Theory	49
4.1	Averaging in the Interaction Frame	50
4.2	Truncation of Internal Hamiltonians	53

4.3	Average Hamiltonian for Finite Pulses	56
4.3.1	Toggling Frame Hamiltonians	57
4.3.2	Average Hamiltonians for the four pulse sequences	62
4.3.3	Simulations Using Average Hamiltonian Expressions	64
5	Exploring the AHT Model: Coherence Control using $\bar{\mathcal{H}}^{(0)}$	67
5.1	FID of the Echo Train	68
5.2	Hahn Echo Analog	71
5.3	Quadrature Detection in the Echo of Echoes	76
5.4	Magic Echo Analog	80
5.4.1	Manipulating the Dipolar Term	80
5.4.2	Magic Echo Analog	83
5.4.3	Optimized Magic Echo	90
6	Quadratic Echo: Coherence Control using $\bar{\mathcal{H}}^{(0)} + \bar{\mathcal{H}}^{(1)}$	94
6.1	Building the Quadratic Echo Sequence	95
6.2	Linear Echo	103
7	Applications of the AHT model	106
7.1	The Composite Block	107
7.2	Time Suspension Sequence	108
7.3	MRI sequence	113
7.3.1	High Resolution MRI Sequence	114
7.4	Comparison to Current Methods and Future Challenges	121
7.4.1	Concluding Remarks	123
A	Phase Transients	124
	Bibliography	128

List of Figures

1.1	Larmor Precession	7
2.1	High Frequency and Low Frequency Tank Circuits	17
3.1	Hahn Echo versus the CPMG Echo Train in Silicon	22
3.2	Hahn Echo Experiment	28
3.3	CPMG Multiple π Pulse Experiment	31
3.4	Even-Odd Effect in Si:P	34
3.5	Pulse Sequence Sensitivity in Silicon	36
3.6	NMR Measurements using a Single Crystal	39
3.7	Proton (H^1) NMR Spectrum in Adamantane	41
3.8	Tail Height Dependence on τ in Adamantane	42
3.9	Pulse Sequence Sensitivity in Adamantane	42
3.10	Comparison of Exact Calculations with Experimental Data in ^{29}Si	45
3.11	Exact Calculations Using Strong But Finite π Pulses	47
4.1	General $\{\phi_1, \phi_2\}$ Pulse Sequence Diagram	57
4.2	Simulations Using Average Hamiltonian Expressions	65
5.1	APCPMG vs. CPMG	70
5.2	Hahn Echo Analog Experiments	73
5.3	CPMG of the Echo Train	75

5.4	Pancake and Racetrack Echoes	78
5.5	Quadrature Detection in the Hahn Echo Analog	80
5.6	Magic Echo Analog Pulse Sequences	86
5.7	Magic Echo Analog Experiment and Simulated Phase Angles	89
5.8	Magic Echo Analog Dependence on Burst Length	92
6.1	Quadratic and Linear Echo Pulse Sequences	98
6.2	Quadratic Echo Dependence on Resonance Offset	100
6.3	Quadratic Echo and Simulated Phase Angle	102
6.4	Virtual Echo and Simulated Phase Angle	103
6.5	Linear Echo Dependence on Resonance Offset	105
7.1	Schematic of the Composite Block Pulse Sequence $\{N, \delta, \psi_1, \psi_2\}$	107
7.2	Line Narrowing Sequence on ^{13}C in C_{60}	109
7.3	Time Suspension Sequence on Teeth and Bone Samples	111
7.4	Time Suspension Sequence on Teeth with Upgraded Equipment	112
7.5	MRI Box Top in C_{60} Sample	114
7.6	MRI Pulse Sequence and Resonance Offset Jump Pattern	116
7.7	High Resolution MRI Pulse Sequence	118
7.8	High Resolution MRI Box Top in C_{60} Sample	119
7.9	High Resolution MRI Box Top in Human Tooth Sample	120
7.10	Magic Echo Analog in Adamantane	122
A.1	Measured Pulse Transients	125
A.2	Phase Transient Experiment	126

List of Tables

4.1	Toggling Frame Hamiltonians for the $\{Y, Y\}$, $\{\bar{Y}, Y\}$, $\{X, X\}$ and $\{\bar{X}, X\}$ Pulse Sequences	61
-----	---	----

Glossary of Symbols and Acronyms

AHT	Average Hamiltonian Theory	2
B_0	Externally applied magnetic field	6
B_1	Transverse magnetic field	6
γ	Gyromagnetic ratio	6
ω_0	Larmor precession frequency	6
rf	Radio frequency	6
T_1	Spin-lattice (or longitudinal) relaxation time	8
T_2	Spin-spin (or transverse) relaxation time	9
L	Inductance of the sample coil	18
C_t	Tuning capacitance of the tank circuit	18

C_m	Matching capacitance of the tank circuit	18
\mathcal{H}_{int}	Internal Hamiltonian of the spin system	25
\mathcal{H}_Z	Zeeman Hamiltonian: $\mathcal{H}_Z = \Omega_z I_{zT}$	23
\mathcal{H}_{zz}	Secular dipolar Hamiltonian: $\mathcal{H}_{zz} = \sum_{i=1}^N \sum_{j>i}^N B_{ij} (3I_{z_i} I_{z_j} - \vec{I} \cdot \vec{I})$	25
B_{ij}	Dipolar coupling constant: $B_{ij} = \frac{1}{2} \frac{\gamma^2 \hbar^2}{r_{ij}^3} (1 - 3 \cos^2 \theta_{ij})$	25
Ω_z	Zeeman energy shift: $\Omega_z = -\gamma \hbar \delta B^{loc}$	23
δB^{loc}	Local magnetic field shift within a macroscopic sample	23
\mathcal{H}_{P_ϕ}	Pulse field Hamiltonian: $\mathcal{H}_{P_\phi} = -\hbar \omega_1 I_{\phi T}$	26
t_p	Pulse duration for a 180° pulse according to $\pi = \omega_1 t_p$	26
FID	Free Induction Decay	29
T_2^*	Apparent decay time of the FID	29
PSS	Pulse Sequence Sensitivity	37

DR	Disorder Realization	44
CP	Carr-Purcell multiple π -pulse sequence	35
CPMG	Carr-Purcell-Meiboom-Gill multiple π -pulse sequence	30
APCP	Alternating-Phase CP multiple π -pulse sequence	35
APCPMG	Alternating-Phase CPMG multiple π -pulse sequence	35
$\{X, X\}$	CP repeating block: $(\tau - 180_X - 2\tau - 180_X - \tau)$	35
$\{Y, Y\}$	CPMG repeating block: $(\tau - 180_Y - 2\tau - 180_Y - \tau)$	35
$\{\bar{X}, X\}$	APCP repeating block: $(\tau - 180_{\bar{X}} - 2\tau - 180_X - \tau)$	35
$\{\bar{Y}, Y\}$	APCPMG repeating block: $(\tau - 180_{\bar{Y}} - 2\tau - 180_Y - \tau)$	35
$\tilde{\mathcal{H}}(t)$	Hamiltonian in the time dependent toggling frame	51
$\bar{\mathcal{H}}^{(i)}$	i th order average Hamiltonian term	52
α	Dimensionless constant: $\alpha = \frac{4\tau}{t_c}$	69
β	Dimensionless constant: $\beta = \frac{t_p}{t_c}$	69

λ	Dimensionless constant: $\lambda = \frac{4t_p}{\pi t_c}$ 69
κ^2	Constant from $\bar{\mathcal{H}}_{\{X,X\}}^{(1)}$: $\kappa^2 = \frac{t_p(8\tau+2t_p)}{2\pi\hbar t_c}$ 95
$\bar{\mathcal{H}}^{(0)}$	Zeroth order second average Hamiltonian 84
FWHM	Full Width at Half Maximum of a spectrum 68
t_c	Cycle time of a repeating pulse sequence 51
Ω_P	Global resonance offset 98
ν_P	Pulse transmitter frequency setting: $\nu_P = -\frac{\Omega_P}{h}$ 98
$\{N, \delta, \psi_1, \psi_2\}$	Composite block: $(\Delta + \delta)-90_{\psi_1}-\{X, X\}^{\frac{N}{2}}\{\bar{X}, \bar{X}\}^{\frac{N}{2}}-90_{\psi_2}-(\Delta - \delta)$.107
Δ	Time interval in the block $\{N, \delta, \psi_1, \psi_2\}$: $\Delta = \frac{Nt_c}{4}$ 107
δ	Time interval in the block $\{N, \delta, \psi_1, \psi_2\}$: $0 \leq \delta < \Delta$ 107

Words of Acknowledgment

When I first started looking for a research group to join, high on my priority list were friendly and intelligent people to work with and interesting questions to answer. I found both in abundance in Sean Barrett's lab and it has been a privilege to be a part of this research family.

I joined the lab at a time when it was unclear where this work would go, and if, in fact, it would go anywhere at all. It was Sean's boundless enthusiasm and unyielding persistence that encouraged us all to keep moving forward despite the mounting skepticism about our experiments. I am extremely grateful for his kindness, support and his Bloch sphere pantomimes which the casual observer could easily have mistaken for semaphore flag signaling. His approachable manner, optimistic outlook and kind spirit are beyond compare.

Although the occasional discouraging and dismissing comment from the scientific community was hard to bear, I always found solace in the humor, kindness and camaraderie of our lab. My lab mentors, Dr. Anatoly Dementyev, Dr. Dale Li and Dr. Yanqun Dong, taught me everything I needed to know about NMR. I want to give special thanks to Dale, poker buddy, fellow Cal alumni and good friend. I have vivid memories of asian snack night, Quantum wine and rock climbing in New Hampshire. As Yanqun and I sat for many years side by side at our desks our relationship grew into a strong friendship. We worked closely on many parts of this project and I am

grateful for all her theoretical guidance. It was good to have another female voice in the lab, as well as someone to talk to not only about science, but also the life that exists outside of science. I would also like to thank our undergraduate researcher John Murray, whose tenure in the lab was short but contributions significant and bat wrangling much appreciated. I am forever indebted to all my lab colleagues. Without their hard work, guidance and friendship, this dissertation would not be possible.

I would like to thank Steven Girvin, Kurt Zilm and Jack Sandweiss for their suggestions, opinions and helpful feedback on our work. In particular, I want to thank Charlie Slichter and Michel Devoret for all their support and kind words about the importance of this project. Although we were told by others that we were investigating an area where “everything is already understood,” they not only believed us when we said that there was still room for new discoveries, but were our best advocates.

Lastly, to my friends and family, a sincere heartfelt thanks. Without your love and support, I would have crumbled away years ago.

Introduction

The work reported in this dissertation, as well as much of the work of my fellow lab mates before me, had its genesis in the simple question, “What is the T_2 of ^{29}Si in crystalline silicon?” Much to our surprise, this has not been easy question to answer.

The question arose as part of a proposal to use nuclear spins in semi-conductors as qubits for quantum computation [1]. The pursuit of the answer has led us unexpectedly in a different, but fortuitous direction. The puzzling results we found at the start of this project eventually lead to a unique method of spin control applicable in large spin systems and more immediately useful in extreme line narrowing and magnetic resonance imaging of solids.

The first stumbling block to determining the transverse spin relaxation time, T_2 , of silicon was a stark discrepancy between two standard experimental methods of measurement [2], one which used a single π -pulse to produce each data point and another that acquired all data points in a single experiment using multiple π -pulses. These two experimental methods should agree in the limit of delta function pulses, when very strong π -pulses are used. Although suspicion was first cast on experimental artifacts or the accumulation of pulse error over many pulses, an exhaustive set of experiments [3, 4] are strong evidence that an extrinsic source was not the reason for the errant behavior.

Ruling out an extrinsic cause was an important step towards legitimizing the

effect. However, it was still difficult to explain why the multiple π -pulse experiments gave a much longer coherence time when, in the strong pulse limit, it should agree with the single pulse experiment. Since this expectation was based on the delta function pulse approximation, we revisited this assumption. Surprisingly, numerical simulations under certain conditions [3, 5] showed that these effects could come from the finite duration of the π -pulses. Although this provided additional support for an intrinsic cause of the behavior, with just these calculations it was hard to gain any insight into the physical mechanism causing the long coherence time observed in the multiple pulse experiments.

To help us develop a better physical picture, Average Hamiltonian Theory (AHT) was used to extract the leading order correction terms coming from the the non-zero duration pulses. Concentrating our efforts on these terms allowed us to begin building the theoretical model that is the focus of this dissertation. Believing these terms to be major contributors to the anomalous behavior, we designed experiments to amplify the effect of these terms in a more controlled way. These explorations eventually lead to the design and demonstration of new and unique classes of spin echoes inspired by classic NMR spin echo experiments. Through these experiments, distinguishing themselves from the classic experiments by their use of terms typically ignored when strong pulses are used, and through numerical simulations [3, 5], we discovered that these terms, although small, could have large impact over the application of many pulses.

Convinced of the validity of this model and finally able to achieve some predicted results, we pushed the model further, turning to the development of possible applications. In the most recent years of this project, we have turned our focus to developing pulse sequences based on this model which show promise in the line narrowing and imaging in solids. MRI imaging in solids has not seen the rapid growth and level

of sophistication that liquid state MRI has seen because of the difficulties in overcoming dipolar dephasing. Since our method provides another way to refocus dipolar dephasing, we hope to make contributions in advancing this field. Currently, our lab is working towards this goal.

The following is a brief chapter by chapter synopsis to guide the reader who wishes to skip ahead.

To begin, Chapter 1 presents a brief review of basic spin physics, both classical and quantum mechanical, and some fundamental concepts in NMR theory. Although elementary in nature, this simple picture of non-interacting spins is far reaching in NMR and can be used to intuitively address many questions regarding spectral line shapes and the experimental design presented in later chapters.

Chapter 2 introduces the necessary tools used in high resolution NMR. For the interested graduate student there are descriptions of the resonant tank circuits we use in the probe and their corresponding capacitance formulas. These formulas can help estimate the necessary parameters to tune the probe to the desired frequency and impedance. Also of practical importance to future students is a detailed description of how to properly adjust the superconducting magnet to obtain a homogeneous and stable field.

Chapter 3 outlines two standard methods used to measure T_2 . The two methods are compared on a theoretical basis to show why the measurements are expected to agree under our experimental conditions. A few of the more salient examples of surprising data [2, 3, 4], given the long standing and well established NMR principles we based our expectations on, are shown as well as our attempts to understand the behavior beyond the delta function pulse approximation.

A brief overview of Average Hamiltonian Theory is presented in Chapter 4, followed by a more detailed analysis as it pertains to the multiple pulse sequences we

first used in our experiments.

Chapter 5 chronicles our exploration of the average Hamiltonian model of the previous chapter. The expressions calculated for the basic multiple pulse experiments presented in Chapter 4 are tested quantitatively for their validity. Using this model up to zeroth order in the average Hamiltonian and guided by classic NMR experiments, we designed analogs to classic NMR experiments based on terms usually ignored when strong pulses are used. Experiments inspired by the original free induction decay (FID), Hahn echo, rotary echo, CPMG echoes and magic echo experiments, which would not be possible in the delta function pulse limit are presented.

Described in Chapter 6 is the extension of this model to include the first order average Hamiltonian term. Although much weaker in magnitude, it was clear from computer simulations that certain conditions would allow the first order average Hamiltonian term to have large impact as many π -pulses are applied. By incorporating phase coherent frequency jumping into our pulse sequences, we demonstrate that higher order terms can also be used in coherence control. A new type of echo, the “quadratic” echo, with behavior that is quantitatively well described by our model and has no classical analog, is demonstrated.

Chapter 7 shows the possible application of this method of coherence control in imaging of solids. One of the difficulties in solid-state NMR imaging is overcoming the line broadening effect of dipolar interactions. Our new approach to line-narrowing and magnetic resonance imaging of solids, which allows control of both Zeeman and dipolar phase wrapping, is outlined here. Data in biological samples, as well as a discussion of the advantages and limitations of this method compared to other imaging methods is presented.

Chapter 1

Spin Basics

In 1946 nuclear magnetic resonance (NMR) in bulk matter was discovered independently and virtually simultaneously by a team led by Edward Purcell at Harvard University [6] and a team led by Felix Bloch at Stanford University [7, 8]. Edward Purcell and Felix Bloch later shared the Nobel Prize for their discovery six years later. At many levels, magnetic resonance can be understood from both a classical and quantum mechanical standpoint [9, 10, 11], so it is perhaps fitting that the two groups viewed the phenomenon from these two approaches.

For the material presented in this dissertation, the classical description of non-interacting spins is far reaching and will be used to address many questions regarding spectral line shapes and optimum experimental design. However, the dipolar solids under investigation cannot be simply or adequately described with classical tools. Each dipole not only reacts to both the large external field and the dipolar fields of neighboring spins, but produces its own field that is felt by its neighbors. The influence of the central spin on the motion of neighboring spins produces time dependent fields that effect the motion of the central spin, and in that way the central spin reacts back on itself. For this complicated behavior, more rigorous quantum mechanical machinery will be required to properly describe the system.

1.1 Classical Spins

1.1.1 Larmor Precession

Bloch's group at Stanford took a classical approach to understand the effects of a magnetic field on a collection of non-interacting magnetic moments [7, 8]. Each nucleus contributing to the total magnetic moment of the system possesses a magnetic moment $\vec{\mu}$. The magnetic fields exert a torque on the magnetic moments causing a reorientation of the total magnetic moment vector. If each magnetic moment was a simple bar magnet allowed to reorient freely, it would tend to line up along the direction of $\vec{B}_0 = B_0 \hat{z}$, where B_0 is the magnitude of the externally applied magnetic field. However, if the moment has angular momentum \vec{J} , it will precess according to the equation of motion

$$\frac{d\vec{J}}{dt} = \vec{\mu} \times \vec{B}_0. \quad (1.1)$$

Using $\vec{\mu} = \gamma \vec{J}$, where γ is the gyromagnetic ratio of the nucleus, this can be rewritten as

$$\frac{d\vec{\mu}}{dt} = \gamma \vec{\mu} \times \vec{B}_0. \quad (1.2)$$

If $\vec{\mu}$ is not aligned with the external magnetic field ($\vec{\mu} \cdot \vec{B}_0 \neq 0$), then it will precess at the Larmor frequency, $\omega_0 = \gamma B_0$, on a cone along a fixed angle, θ (Figure 1.1).

To observe nuclear magnetic resonance, the system under study is placed in small solenoid perpendicular to the large external field \vec{B}_0 . A signal will only be observed if the spins are tipped away from the \hat{z} -axis and allowed to precess. Since the equilibrium state of the system has total magnetization vector, \vec{M} , aligned along \hat{z} , the magnetic moments can be reoriented and manipulated by applying a radio frequency (rf) field with the same frequency as the rate of spin precession. By applying an rf field, \vec{B}_1 , at the Larmor frequency, the spins along \hat{z} in thermal equilibrium are driven towards

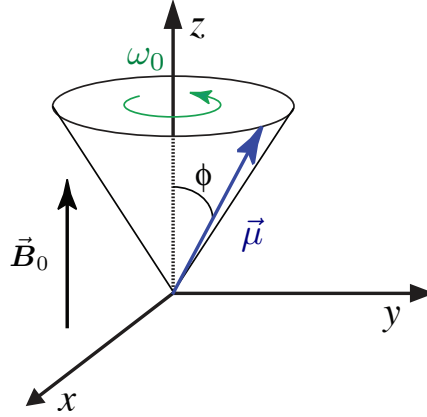


Figure 1.1: The precession of the moment $\vec{\mu}$ at fixed angle ϕ from the external field \vec{B}_0 about a cone. The moment $\vec{\mu}$ precesses at the Larmor frequency $\omega_0 = \gamma B_0$.

the x - y plane where they can be measured. Once in this orientation, the alternating magnetic field due to the precessing component of \vec{M} perpendicular to the external field will generate a voltage in the solenoid by induction.

1.1.2 The Rotating Frame

The response of the system to the application of radio frequency pulses is often conveniently analyzed in a frame rotating at the Larmor frequency [12, 10, 13, 14]. From the perspective of an observer watching spins from the fixed lab frame, the spins precess about \hat{z} at the frequency ω_0 . If the observer is instead in a frame rotating at the Larmor frequency the spins will appear motionless, as if there is no applied field. The externally applied field, \vec{B}_0 , is much larger in scale than both the control pulses and the residual internal fields of interest, making it convenient to work in a rotating frame where the trivial motion caused by the large external field is removed.

In the rotating frame, the effect of a linearly polarized rf field on the spins is also simplified. In the lab frame, the linearly polarized rf field produced by the coil can be regarded as two counter rotating fields with the same frequency. When viewed in a frame rotating at the same radio frequency, the component that rotates in the

same sense as the rotating frame will look like a constant field in the transverse plane, while the component that rotates in the opposite sense will appear to precess at $2\omega_0$. For large \vec{B}_0 the counter-rotating field oscillates far enough from resonance that it has little effect on the magnetic moments and is therefore ignored [15].

1.1.3 Bloch Equations and Spin Relaxation

In this simplified analysis, the precession of spins would go on indefinitely if there were no methods of relaxation. However, given enough time in any real system, the magnetization will align along the direction of the external magnetic field. The source of this relaxation, which is the bulk of the discussion in most NMR textbooks [9, 10, 13, 14, 11], is a complicated subject where a full description requires the machinery of quantum mechanics. However, the phenomenological Bloch equations provide an elegant, qualitative description of the relaxation of the nuclear polarization \vec{M} [7, 10].

Bloch's approach adds an extra term to each component of the equation of motion from equation (1.2) to account for spin relaxation. The Bloch equations are given by

$$\frac{d}{dt}M_x = \gamma(\vec{M} \times \vec{B})_x - \frac{M_x}{T_2} \quad (1.3)$$

$$\frac{d}{dt}M_y = \gamma(\vec{M} \times \vec{B})_y - \frac{M_y}{T_2} \quad (1.4)$$

$$\frac{d}{dt}M_z = \gamma(\vec{M} \times \vec{B})_z + \frac{M_0 - M_z}{T_1} \quad (1.5)$$

where $\vec{M} = (M_x, M_y, M_z)$ and the spin relaxation is characterized by two times, T_1 and T_2 . The structure of the added terms ensures that M_0 is the equilibrium value of M_z , while M_x and M_y tend to zero at equilibrium.

The characteristic time constant, T_1 , is the spin-lattice or longitudinal relaxation time. In order for spins to polarize along the direction of the large external field, high

energy spins anti-parallel to the field require a mechanism for an energy-lowering spin flip. Fluctuating fields produced by other spin species provide a major relaxation mechanism, but others include atomic vibrations, translations and rotations depending on the spin bath environment.

The time constant, T_2 , which is a main focus in this dissertation, characterizes the relaxation of transverse magnetization. It is referred to as the spin-spin or transverse relaxation time. The contributing mechanisms here, unlike T_1 relaxation, involve interactions in which there is no net energy transfer from the spin system to the environment. The primary interactions causing T_2 relaxation are from local fluctuations in the magnetic field at the site of the nucleus. These small field fluctuations can come from the dipolar fields produced by other spins. Due to the variation in local fields, the nuclei precess at slightly different rates. As the spins get more and more out of step with one another, they point in all directions in the x - y plane, causing the vector sum of the the transverse magnetization to approach zero.

1.2 Quantum Mechanical Spins

Purcell's team at Harvard, being spectroscopists, took a quantum mechanical approach. They considered how the external magnetic field splits the energy levels of the nuclear magnetic moments and how an applied rf field caused transitions between these levels [6].

1.2.1 Larmor Frequency

In the quantum mechanical description, the Hamiltonian for a magnetic moment $\vec{\mu}$ in a static magnetic field \vec{B}_0 has the form

$$\mathcal{H} = -\vec{\mu} \cdot \vec{B}_0. \quad (1.6)$$

Here, the magnetic moment $\vec{\mu}$ is related to the nuclear spin operator, \vec{I} , by Planck's constant

$$\vec{\mu} = \gamma \hbar \vec{I}. \quad (1.7)$$

For a spin $\frac{1}{2}$ -system the allowed eigenvalues of I_z are $m_I = \pm\frac{1}{2}$, so the two energy levels are separated by an amount

$$\Delta E = \hbar \gamma B_0. \quad (1.8)$$

Transitions between the energy levels require that the angular frequency of applied radiation satisfy the resonance condition

$$\omega = \gamma B_0. \quad (1.9)$$

In the quantum mechanical description, the Larmor frequency is a measure of the energy quanta required to cause transitions between energy levels, rather than the precession frequency of classical spins about a cone. For typical nuclei in strong fields ($B_0 \sim 10$ Tesla), the frequency falls in the radio frequency range.

1.2.2 Quantum Mechanical Equation of Motion

To compare to the classical description, and since these are the quantities measured in experiment we need to know the expectation value of the magnetic moment operator $\langle \vec{\mu}(t) \rangle = \gamma \hbar \langle \vec{I}(t) \rangle$. The equation of motion of the operator $\vec{\mu}(t)$ is given by the Heisenberg equation,

$$\frac{d}{dt} \vec{\mu} = -\frac{i}{\hbar} [\vec{\mu}, \mathcal{H}] \quad (1.10)$$

$$= -\frac{i}{\hbar} [\vec{\mu}, -\gamma \hbar \vec{I} \cdot \vec{B}_0] \quad (1.11)$$

$$= i\gamma^2 \hbar [\vec{I}, I_x B_x + I_y B_y + I_z B_z]. \quad (1.12)$$

Taking the commutator and the expectation value of this expression gives an analogous expression to the classical equation (1.2).

$$\frac{d\langle \vec{\mu} \rangle}{dt} = \langle \vec{\mu} \rangle \times \vec{B}. \quad (1.13)$$

However, this reduction to the classical equation is only possible because the Hamiltonian under consideration is linear in the spin operator \vec{I} . For this dissertation, we are primarily concerned with dipolar systems which cannot be described so easily.

1.2.3 Density Matrix Representation

For coupled spins in quantum many-body systems, a classical approach is not capable of a full description. Many interactions, such as multiple quantum coherence effects, have no classical analog. To describe the quantum mechanical evolution of systems like these, we use the density operator $\rho(t)$.

For an idealized pure state, where all spin systems in the ensemble are in the same

state described by the state function

$$|\psi(t)\rangle = \sum_i c_i(t)|i\rangle, \quad (1.14)$$

the density operator is

$$\rho(t) = \sum_i \sum_j c_i(t)c_j^*(t)|i\rangle\langle j|. \quad (1.15)$$

For an ensemble in thermal equilibrium, spin systems in the ensemble have a probability p^k of being in the state $|\psi^k(t)\rangle$. For the ensemble in this mixed state, the density operator is given by

$$\rho(t) = \sum_i \sum_j \overline{c_i(t)c_j^*(t)}|i\rangle\langle j|. \quad (1.16)$$

where the bar denotes the ensemble average. The equation of motion for the density matrix is

$$\frac{d}{dt}\rho = -\frac{i}{\hbar}[\mathcal{H}, \rho]. \quad (1.17)$$

If \mathcal{H} is time independent, which is often possible with an appropriate choice of coordinate system, the time dependent density matrix becomes

$$\rho(t) = e^{-\frac{i}{\hbar}\mathcal{H}t}\rho(0)e^{+\frac{i}{\hbar}\mathcal{H}t}. \quad (1.18)$$

From this equation, the time evolution operator can be identified as $\mathcal{U} \equiv e^{-\frac{i}{\hbar}\mathcal{H}t}$. Once the time dependent density matrix is given, the the expectation value of the

spin operators can be calculated by

$$\langle I_x \rangle = \text{Tr} [\rho(t) I_x] \quad (1.19)$$

$$\langle I_y \rangle = \text{Tr} [\rho(t) I_y] \quad (1.20)$$

$$\langle I_z \rangle = \text{Tr} [\rho(t) I_z] \quad (1.21)$$

where Tr indicates the trace of the matrix. These expressions allow us to calculate the observable $\vec{M}(t) = N \langle \vec{\mu}(t) \rangle$ which is related to the spin operators by $\langle \vec{\mu}(t) \rangle = \gamma \hbar \langle \vec{I}(t) \rangle$.

Chapter 2

NMR Experimental Details

2.1 Pulsed NMR Spectrometer

The first NMR experiments used a steady state or continuous wave spectroscopy approach [8, 6]. Information about a system was gathered by monitoring the response to constant irradiation. The response would change as the frequency of radiating field, or the strength of the longitudinal field B_0 , was swept past the resonance condition. Twenty years later, pulsed NMR was introduced and showed that the same information and more could be gathered using short intense pulses of resonant rf radiation [16]. These short rf pulses allow an experimenter to investigate the response of the system to many frequencies sent to the sample all at once. Then the resulting time domain signal can be decomposed into its spectral components by Fourier transformation.

For the experiments in this dissertation, we used a Tecmag Apollo spectrometer. The spectrometer functions as both a transmitter, controlling the quick intense bursts of rf radiation sent to the sample, and as a receiver, amplifying and collecting the time domain signal that can be Fourier transformed into a spectrum.

2.1.1 Transmitter

To achieve a particular macroscopic magnetic moment configuration, the experimenter needs precise control of the length of time the rf pulse is applied, as well as its amplitude and phase. The amplitude of the tipping field dictates how quickly spins are reoriented. The stronger the pulse, the faster the spin rotations and the closer the pulse action is to an ideal rotation. For short, intense pulses other spin interactions can often be ignored¹. For the experiments in this dissertation, we use high amplitude, square rf pulses aligned either along the x or y -axis to manipulate spins.

Our transmitter consists of a digital frequency synthesizer, transmitter modulator and amplifier. The synthesizer produces a continuous rf wave that is modified into the desired pulse shape and adjusted to the specified phase by the modulator. The signal is then sent to the amplifier which intensifies the signal to the desired amplitude.

2.1.2 Receiver

Tipping the magnetization vector towards the x - y plane causes spins to precess about \vec{B}_0 . As the magnetization precesses, it induces a voltage in the coil wrapped around the sample. The weak nuclear induction signal is first magnified by a pre-amp and then sent to the spectrometer for quadrature heterodyne detection [14]. This mixing technique allows the experimenter to record both the x - and y -component of the precessing nuclear magnetization, termed the “real” and “imaginary” channel respectively, in the rotating frame. In the first detection stage, the Apollo spectrometer demodulates to an intermediate frequency of 11.25 MHz, rather than removing the Larmor carrier frequency altogether (homodyne detection). In the second stage, the signal is digitized, digitally filtered and the intermediate frequency is removed. Com-

¹Exceptions will be covered in later chapters.

pared to homodyne detection, this avoids problems associated with detection near DC levels. As a final step, the signal is intensified again and digitally stored for analysis.

2.2 Tank Circuits

To deliver the rf pulses to the actual sample and collect the resulting signal, a resonant tank circuit is used. We typically use one of two tank circuit designs [14], depending on the desired frequency (Figure 2.1). Both include a coil with inductance L , which surrounds the sample, and two variable capacitors, C_t and C_m . There is also a small resistance, r , due to the resistance of the wire making up the coil. Without C_m , the two circuits reduce to either a simple series or parallel LRC circuit. In both the simple parallel and series LRC circuits the undamped resonance frequency is $\omega = \frac{1}{\sqrt{LC_t}}$. The resonance, which should be tuned to the Larmor frequency, is controlled by changing C_t . Although adjusting L is also an option, it is less practical than a variable capacitor and usually requires winding of a new coil. Another inconvenience is the physical restriction on the coil size due to the confined space within the magnet bore and the coil's function as a sample holder.

However, finding the right tuning frequency is not the only requirement on the NMR tank circuit. In order to get the most power delivered to the sample and the most signal returned from the sample without reflection, the impedance of the tank circuit must match the 50Ω cable attached to the spectrometer. To meet this requirement, C_m is included in the two configurations shown in Figure 2.1. By requiring impedance matching at the desired resonant frequency, the exact values of C_t and C_m

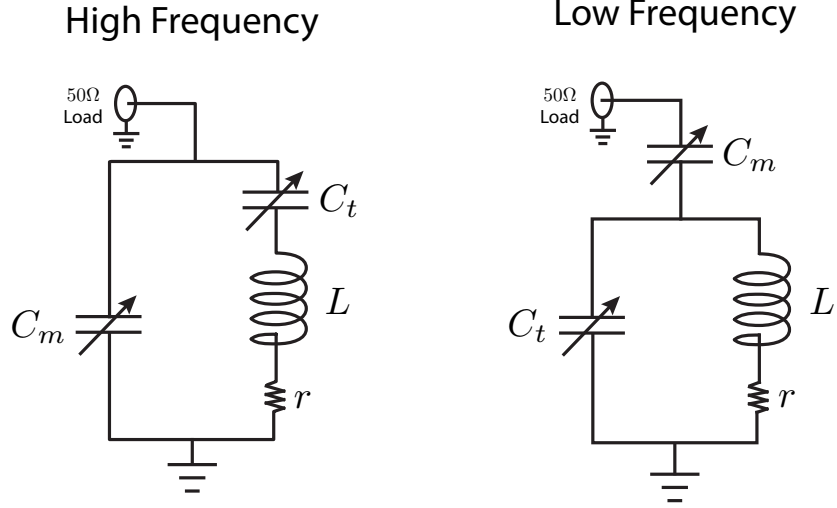


Figure 2.1: High frequency tank circuit for resonant frequencies > 100 MHz and low frequency tank circuit for resonant frequencies < 100 MHz. The sample is placed in the inductor, L . Typical values of L fall in the range $\sim 10 - 100 \mu\text{-Henries}$ depending on coil size and number of turns. Typical values of C_t and C_m range from $\sim 1\text{-}200\text{pF}$ and resistance, r , is $\lesssim 5\Omega$.

for the two circuits can be calculated directly.

$$\text{High Frequency: } C_t = \frac{L\omega + \sqrt{(50\Omega - r)r}}{\omega(L^2\omega^2 - (50\Omega)r + r^2)} \quad (2.1)$$

$$C_m = \frac{1 - \frac{r}{50\Omega}}{\omega\sqrt{(50\Omega - r)r}} \quad (2.2)$$

$$\text{Low Frequency: } C_t = \frac{L\omega - \sqrt{\frac{r}{50\Omega}(L^2\omega^2 - (50\Omega)r + r^2)}}{\omega(L^2\omega^2 + r^2)} \quad (2.3)$$

$$C_m = \frac{\sqrt{\frac{r}{50\Omega}}}{\omega\sqrt{L^2\omega^2 - (50\Omega)r + r^2}} \quad (2.4)$$

Perhaps more useful are the following approximations for $r \ll \omega L$, which is generally

true for our coils.

$$\text{High Frequency: } C_t \approx \frac{1}{\omega \sqrt{r(50\Omega)}} \quad (2.5)$$

$$C_m \approx \frac{1}{\omega^2 L - \omega \sqrt{r(50\Omega)}} \quad (2.6)$$

$$\text{Low Frequency: } C_t \approx \frac{1}{\omega^2 L \left(1 + \sqrt{\frac{r}{50\Omega}}\right)} \quad (2.7)$$

$$C_m \approx \frac{\sqrt{\frac{r}{50\Omega}}}{\omega^2 L} \quad (2.8)$$

For our tank circuits, the typical range of values is $\lesssim 5\Omega$ for r , $10 \sim 200$ MHz for the resonance frequency $\frac{\omega}{2\pi}$, and $10 \sim 100$ μ -Henries for L . By adjusting the tuning capacitor, C_t , the frequency of the circuit can be tuned, while the matching capacitor, C_m , is adjusted to keep the impedance of the circuit at 50Ω . The variable capacitors we use range from 2-25 pF. If the circuit requires a capacitance outside this range, fixed capacitors are used in series or parallel to reach it. The high frequency circuit, with C_t and L in series, is typically used for resonance frequencies > 100 MHz. Below 100 MHz, the low frequency circuit, with C_t and L in parallel, is often used. In practice, this division is only a guideline and choosing the best circuit is done through trial and error.

2.3 Superconducting Magnet

A large, homogeneous and stable external magnetic field is required for high resolution solid state NMR experiments. High fields offer larger nuclear spin polarization and therefore better signal to noise. The field must also be homogeneous. Observing the signal from a sample often requires a field that varies less than one part per million (ppm) over the sample volume. If the large external field is too inhomogeneous, it will

obscure the smaller field variations arising from the sample. The natural line width, which is a measure of these local fields, can be drowned out if there are significant spatial and temporal field fluctuations over the duration of the experiment, which in some cases may take several hours.

To meet these restrictions, a superconducting magnet run in persistent current mode was used. The experiments in this dissertation were conducted on an Oxford Instruments Teslatron type II superconducting magnet with an 88 mm wide bore. Most experiments were run at the maximum field of 12 Tesla at room temperature, with a field drift < 0.01 ppm/hour.

To achieve a such a stable field, first the magnet is slowly energized to the desired strength, plus an overshoot of 0.017 Tesla as suggested by the manufacturer. After a 20 minute wait period the superconducting magnet is brought down to the intended field and left in persistent current mode. This guarantees a drift rate < 0.1 ppm/hour. After changing the field strength, the drift is monitored by recording the signal from a deuterium sample over the next 10+ hours. Over this time period the field should settle to a stable value. For most of our experiments, the drift rate is much lower than 0.1 ppm/hour since the field typically stabilizes to ~ 5 ppb/hour after several days of keeping the superconducting magnet in persistent current mode.

Once the field is stable to < 0.1 ppm per hour, then the spatial field homogeneity can be improved. Through a process called “shimming,” an extremely homogenous field across a volume of ~ 1 cm³ can be achieved. During the shimming process, the field strength as a function of position is measured using an ~ 1 mm³ deuterium droplet. By measuring the NMR signal from the droplet in different positions within the magnet, a spatial profile of the field can be mapped.

The gradients found in the initial field mapping are minimized by turning on currents that flow through a set of smaller superconducting coils. These pre-installed

shim coils control the $\frac{\partial}{\partial z}$, $\frac{\partial^2}{\partial z^2}$, $\frac{\partial}{\partial x}$, $\frac{\partial}{\partial y}$, $\frac{\partial^2}{\partial x^2}$, $\frac{\partial^2}{\partial y^2}$ and $\frac{\partial^2}{\partial x \partial y}$ gradient fields. To properly calibrate the gradient coils, the current through a single coil is set to a specified value and the field profile remeasured. This process is repeated for all the shim coils to determine each coil's contribution to the overall field at a given current strength. From these measurements, the appropriate current settings to counteract the inhomogeneity of the field created by the large superconducting solenoid are calculated and applied. By carefully and painstakingly shimming the magnet, we can typically achieve < 0.2 ppm magnetic field homogeneity over a $\sim 1\text{cm}^3$ volume at the field center.

Chapter 3

NMR Measurements and Unexpected Spin Echoes

Having reviewed the basic physics and tools used in NMR, we can address some of the initial questions that led us to discover the new spin echo phenomena that are the focus of this dissertation. The current chapter reviews the most salient experimental inconsistencies with theory that began this project and the subsequent work probing the source of the disagreement. This large body of work, detailed in the dissertations of Dr. Anatoly Dementyev [2], Dr. Dale Li [4], and Dr. Yanqun Dong [5] will be briefly summarized here, highlighting the important advances in our understanding in the phenomenon and my personal efforts to support this investigation.

3.1 Unexpected Echoes

Over the past 60 years, NMR has matured into a sophisticated tool for the control and characterization of spin decoherence. For this reason, nuclear spins have become an attractive system for implementing quantum computation [1, 17, 18, 19]. In particular, given the existing infrastructure of the semiconductor industry, spins in

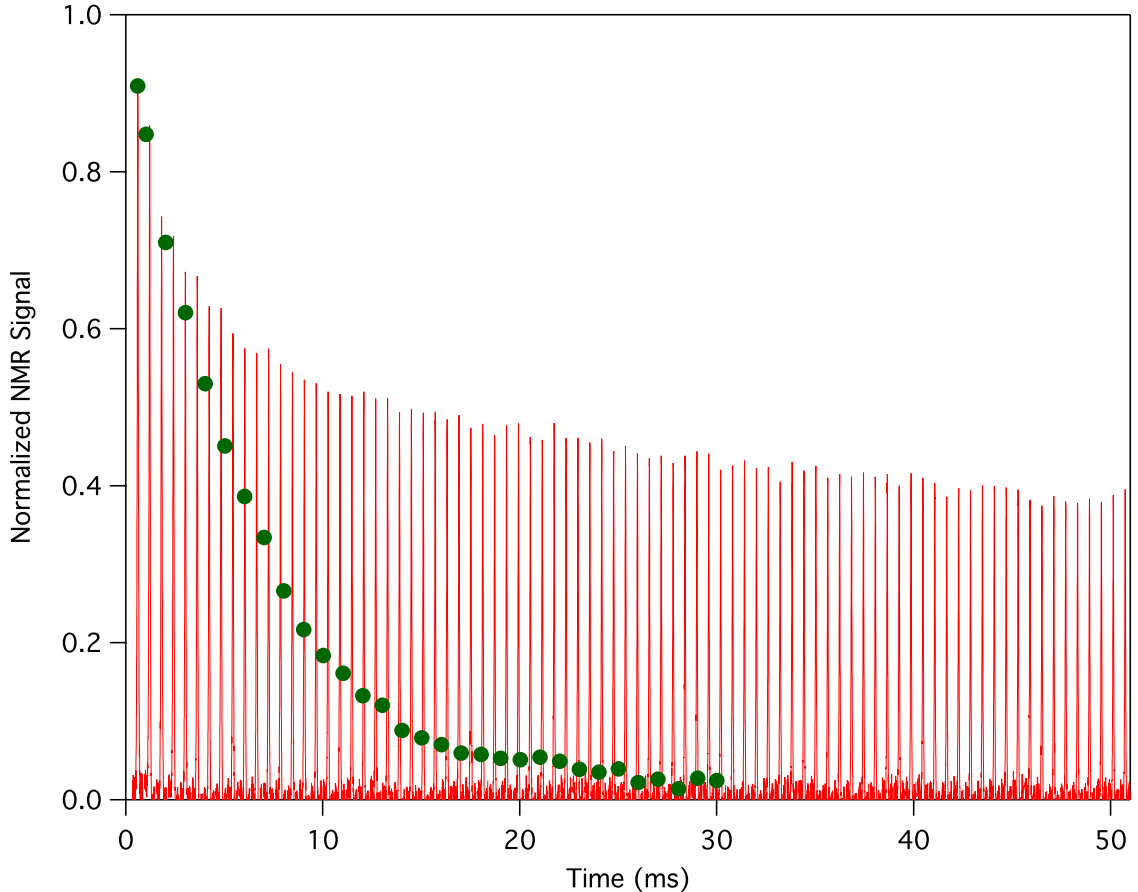


Figure 3.1: Two NMR experiments to measure T_2 in ^{29}Si in a crushed powder of Silicon doped with Phosphorus ($3.94 \times 10^{19} \text{ P/cm}^3$). Hahn echo peaks (dots) are generated with a single π -pulse. The CPMG echo train (lines) are generated with multiple π -pulses spaced with delay $2\tau = 592\mu\text{s}$. Normalization is set by the initial magnetization after the first 90_X pulse. Data taken at room temperature in a 12 Tesla field. From reference [24].

semiconductors seemed particularly promising as a scalable system [1, 20, 21, 22]. For many of these proposals the spin dynamics of ^{29}Si are important, whether the silicon nuclei play the central role as qubits [22] or rather, contribute to the decohering background environment of other qubits [1, 20, 21]. To support these efforts, our group intended to measure the spin-spin relaxation time, T_2 , in silicon doped with phosphorus. In doing so, we were met with many startling results [2, 4, 23, 24].

Using two standard methods of measuring T_2 [10, 14], we were surprised not only

that they did not agree, but also that one method showed measurable ^{29}Si NMR signals out to much longer times than theoretically expected. The results of both methods, shown in Figure 3.1, are clearly very different.

In order to discuss the two methods of measurement, why they should agree, as well as some of the other unexpected behavior, a review the relevant Hamiltonian describing the system is needed.

3.2 Internal Hamiltonian

For a system of N spin- $\frac{1}{2}$ nuclei in an external magnetic field, like the ^{29}Si nuclear system shown in Figure 3.1, we found that the relevant spin Hamiltonian in the lab frame, \mathcal{H}^{lab} , has the form [2, 9, 10, 25]

$$\mathcal{H}^{\text{lab}} = \mathcal{H}_Z^{\text{lab}} + \mathcal{H}_d^{\text{lab}} \quad (3.1)$$

where $\mathcal{H}_Z^{\text{lab}}$ is the Zeeman Hamiltonian and $\mathcal{H}_d^{\text{lab}}$ is the dipolar Hamiltonian.

3.2.1 Zeeman Hamiltonian

In the lab frame, the Zeeman Hamiltonian has the form

$$\mathcal{H}_Z^{\text{lab}} = \sum_{i=1}^N -\gamma\hbar(B_0 + \delta B_i)I_{z_i} \quad (3.2)$$

where B_0 is the large external field and δB_i is the small Zeeman shift at nuclear site i due to spatial magnetic inhomogeneities. In the rotating frame defined by the Larmor precession frequency, $\omega_0 = \gamma B_0$, the Zeeman Hamiltonian reduces to a term that contains only the small Zeeman shift, $\Omega_{z_i} = -\gamma\hbar\delta B_i$. For the systems appropriate to the model presented in later chapters, Ω_{z_i} is the same for a large

number of neighboring spins. This allows us to drop the index i from the Zeeman shift term. The simplified Zeeman Hamiltonian in the rotating frame is given by

$$\mathcal{H}_Z = \sum_{i=1}^N \Omega_z I_{z_i} = \Omega_z I_{z_T} \quad (3.3)$$

where $I_{z_T} = \sum_{i=1}^N I_{z_i}$ is the total I_z spin operator.

3.2.2 Dipolar Hamiltonian

In the lab frame, the magnetic interaction between neighboring spins μ_i and μ_j is described by the full dipolar Hamiltonian,

$$\mathcal{H}_d^{\text{lab}} = \sum_{i=1}^N \sum_{j>i}^N \left[\frac{\vec{\mu}_i \cdot \vec{\mu}_j}{|\vec{r}_{ij}|^3} - \frac{3(\vec{\mu}_i \cdot \vec{r}_{ij})(\vec{\mu}_j \cdot \vec{r}_{ij})}{|\vec{r}_{ij}|^5} \right]. \quad (3.4)$$

Writing the Hamiltonian in spherical coordinates and using the raising and lowering operators I^\pm for two like spins (i.e. $\gamma_1 = \gamma_2$ and $N = 2$) gives

$$\mathcal{H}_d = \frac{\gamma^2 \hbar^2}{r^3} (A + B + C + D + E + F) \quad (3.5)$$

where the terms in the so-called dipolar alphabet [9, 10, 25] are defined as

$$\begin{aligned} A &= I_{1_z} I_{2_z} (1 - 3 \cos^2 \theta) \\ B &= -\frac{1}{4} (I_1^+ I_2^- + I_1^- I_2^+) (1 - 3 \cos^2 \theta) \\ C &= -\frac{3}{2} (I_1^+ I_{2_z} + I_{1_z} I_2^+) \sin \theta \cos \theta e^{-i\phi} \\ D &= -\frac{3}{2} (I_1^- I_{2_z} + I_{1_z} I_2^-) \sin \theta \cos \theta e^{i\phi} \\ E &= -\frac{3}{4} I_1^+ I_2^+ \sin^2 \theta e^{-i2\phi} \\ F &= -\frac{3}{4} I_1^- I_2^- \sin^2 \theta e^{i2\phi}. \end{aligned} \quad (3.6)$$

In the rotating frame, the terms proportional to $e^{i\phi}$ and $e^{i2\phi}$ will oscillate rapidly at ω_0 and $2\omega_0$ and effectively average to zero. From a quantum mechanical standpoint, terms A and B connect degenerate energy states, while terms C , D , E and F contain off diagonal matrix elements that connect states differing in energy by $\hbar\omega_0$ and $2\hbar\omega_0$. The transition probabilities between the off diagonal matrix elements are so low it is an excellent approximation to ignore these terms [9, 10]. Dropping these latter terms gives the secular dipolar Hamiltonian

$$\mathcal{H}_{zz} = \sum_{i=1}^N \sum_{j>i}^N B_{ij} \left(3I_{z_i} I_{z_j} - \vec{I}_i \cdot \vec{I}_j \right) \quad (3.7)$$

where the dipolar coupling constant, B_{ij} , is defined as

$$B_{ij} = \frac{1}{2} \frac{\gamma^2 \hbar^2}{r_{ij}^3} (1 - 3 \cos^2 \theta_{ij}). \quad (3.8)$$

The position vector between spins i and j is given by \vec{r}_{ij} and θ_{ij} is the angle between \vec{r}_{ij} and \vec{B}_0 . This secular form of the dipolar coupling, which commutes with \mathcal{H}_Z , is the form used throughout the remainder of this dissertation.

The form of the internal spin Hamiltonian in the rotating frame is given by

$$\mathcal{H}_{int} = \mathcal{H}_Z + \mathcal{H}_{zz}. \quad (3.9)$$

Using the rotating frame expression of H_{int} in equation (1.18) gives the density matrix

$$\rho(t) = e^{-\frac{i}{\hbar}(\Omega_z I_{z_T} + \mathcal{H}_{zz})t} \rho(0) e^{+\frac{i}{\hbar}(\Omega_z I_{z_T} + \mathcal{H}_{zz})t} \quad (3.10)$$

where we identify the time evolution operators

$$\mathcal{U} = e^{-\frac{i}{\hbar}(\Omega_z I_{zT} + \mathcal{H}_{zz})t} \quad (3.11)$$

$$\mathcal{U}_Z \mathcal{U}_{zz} = e^{-\frac{i}{\hbar}\Omega_z I_{zT}t} e^{-\frac{i}{\hbar}\mathcal{H}_{zz}t}. \quad (3.12)$$

These expressions will be useful later in analyzing the effect of pulses on the evolution a dipolar spin system.

3.3 Delta Function Pulse Approximation

When rf pulses are applied, the Hamiltonian has the more complicated form

$$\mathcal{H}_{tot} = \mathcal{H}_{int} + \mathcal{H}_{P_\phi} \quad (3.13)$$

$$= \Omega_z I_{zT} + \mathcal{H}_{zz} + \mathcal{H}_{P_\phi} \quad (3.14)$$

where

$$\mathcal{H}_{P_\phi} = -\hbar\omega_1 I_{\phi T} \quad (3.15)$$

for an rf pulse with strength $\omega_1 = \gamma B_1$ and pulse phase ϕ . In general, $[\mathcal{H}_{int}, \mathcal{H}_{P_\phi}] \neq 0$, so it convenient to work in the regime $\mathcal{H}_{P_\phi} \gg \mathcal{H}_{int}$, where the pulse strength is much larger than the spectral line width. Then the Hamiltonian can be simply approximated as \mathcal{H}_{P_ϕ} when pulses are applied, as described below.

The rotation rate depends on the pulse strength ω_1 , the rotation angle is controlled by setting the pulse duration and the pulse phase ϕ defines the axis of rotation. For a 180° pulse, the pulse time, t_p , must satisfy $\pi = \omega_1 t_p$. For strong pulses where $\mathcal{H}_{P_\phi} \gg \mathcal{H}_{int}$ is satisfied, the delta function pulse approximation, which takes the limit $t_p \rightarrow 0$ while $\omega_1 \rightarrow \infty$, is conventionally made [9, 10, 13, 25, 26]. The effect on

the system is a rotation of the form

$$\mathcal{R}_\phi = e^{i\pi I_\phi} \quad (3.16)$$

which is an instantaneous, pure rotation. For delta function π -pulse rotations, the Zeeman Hamiltonian is perfectly inverted ($\Omega_z I_{zT} \rightarrow -\Omega_z I_{zT}$) while the bilinear dipolar coupling Hamiltonian, which has terms like $I_{z_i} I_{z_j} \rightarrow (-1)^2 I_{z_i} I_{z_j}$, is left unaltered for ϕ lying in the x - y plane.

The effect of a delta function π -pulse on the time evolution operator in equation (3.11) can be shown more rigorously by the transformation

$$\mathcal{R}_\phi \mathcal{U} \mathcal{R}_\phi^{-1} = e^{i\pi I_\phi} e^{-\frac{i}{\hbar}(\Omega_z I_{zT} + \mathcal{H}_{zz})t} e^{-i\pi I_\phi} \quad (3.17)$$

$$\mathcal{R}_\phi \mathcal{U}_Z (\mathcal{R}_\phi^{-1} \mathcal{R}_\phi) \mathcal{U}_{zz} \mathcal{R}_\phi^{-1} = e^{i\pi I_\phi} e^{-\frac{i}{\hbar} \Omega_z I_{zT} t} (e^{-i\pi I_\phi} e^{+i\pi I_\phi}) e^{-\frac{i}{\hbar} \mathcal{H}_{zz} t} e^{-i\pi I_\phi} \quad (3.18)$$

$$\mathcal{U}_Z^{-1} \mathcal{U}_{zz} = e^{+\frac{i}{\hbar} \Omega_z I_{zT} t} e^{-\frac{i}{\hbar} \mathcal{H}_{zz} t}. \quad (3.19)$$

3.4 Measuring T_2

With these concepts in mind, we can return to the discrepancy shown in Figure 3.1 and why we would expect the two methods to agree.

3.4.1 Hahn Echo Two Pulse Sequence

The first method for measuring T_2 is the Hahn spin echo [27]. The schematic in Figure 3.2 shows the general pulse sequence,

$$90_{\phi_1} - \tau - 180_{\phi_2} - \tau - \text{echo}.$$

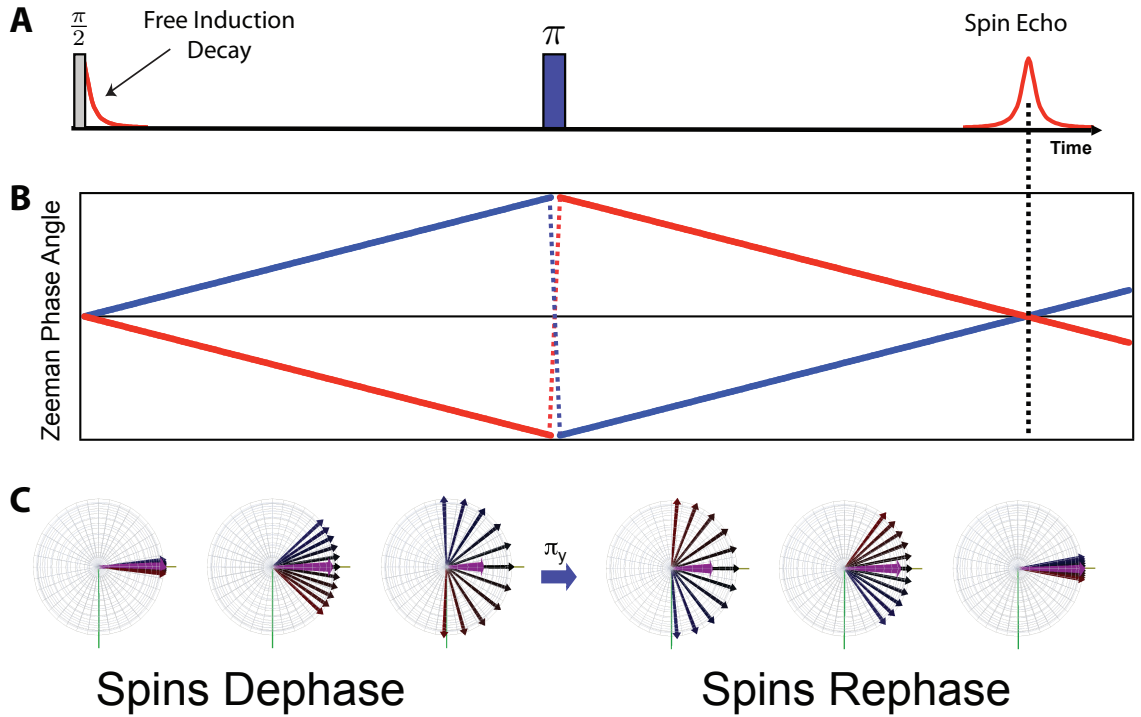


Figure 3.2: **A.** Hahn echo pulse sequence: $90_{\phi_1} - \tau - 180_{\phi_2} - \tau - \text{echo}$. The initializing $\frac{\pi}{2}$ -pulse brings the spins into the transverse plane where they begin to dephase, resulting in a free induction decay (FID). Applying a π -pulse causes the spins to rephase, resulting in a spin echo. **B.** Two representative spin clusters with $\vec{B} = \vec{B}_0 \pm \delta\vec{B}$ due to local field inhomogeneities will accumulate a Zeeman phase angle given by $\theta = \pm \frac{\Omega_z}{\hbar} t$. The sign of Ω_z is reversed by the π -pulse, causing spins to rephase and a spin echo to appear at the point where the Zeeman phase lines cross. **C.** A pictorial representation of the Zeeman dephasing that occurs after the $\frac{\pi}{2}$ -pulse, and the rephasing that occurs after the π -pulse. Each arrow represents a spin cluster with the same value of Ω_z .

The pulse is represented by the angle of rotation with the pulse phase as a subscript. The first pulse, a 90° pulse along the ϕ_1 direction, brings the spins from their equilibrium position along the z -axis into the x - y plane where they begin to precess. As groups of spins precess at slightly different rates according to the local fields they experience, they will tend to drift away from each other. Each arrow in Figure 3.2C represents a large cluster of spins with a slightly different precession frequency, $\frac{\Omega_z}{\hbar}$. As the spins get out of step with one another, the total magnetization will decay away with a characteristic time T_2^* . This so-called free induction decay (FID) is observed immediately after the 90° pulse. Figure 3.2B follows the Zeeman phase of just two spin clusters with $\pm\Omega_z$. As free evolution progresses, the spin clusters accumulate a net Zeeman phase angle, $\theta = \pm\frac{\Omega_z}{\hbar}t$, which is shown pictorially in Figure 3.2C.

After a free evolution period of duration τ , a single π -pulse is applied. For a delta function rotation, the sign of the Zeeman term is reversed, while the bilinear dipolar term is left unchanged. In the second time interval, the system develops under the negative of the original Zeeman Hamiltonian, effectively undoing the Zeeman dephasing that occurred in the first time interval. In the absence of any dipolar interaction, the emerging spin echo will have the same magnitude as the initial FID. In practice, some coherence is lost due to the dipolar coupling that cannot be refocused by the π -pulse, making the Hahn echo experiment a good tool for measuring the decohering effect caused by spin-spin interactions. By varying the length of time τ between the two pulses and measuring the height of the resulting spin echo, a dipolar decay curve can be measured. The green points in Figure 3.1 were acquired one data point at a time using the Hahn echo experiment.

3.4.2 Carr-Purcell-Meiboom-Gill Multiple π -Pulse Sequence

An alternative method for measuring T_2 decay is the Carr-Purcell-Meiboom-Gill (CPMG) experiment [28, 29] shown in Figure 3.3. This experiment, written as

$$90_X - \tau - \{180_Y - \tau - \text{echo} - \tau\}^n,$$

applies a train of equally spaced π -pulses to the system. The block in brackets is repeated n times producing n spin echoes in a single experiment. For $n = 1$, the sequence is identical to the Hahn echo experiment. Each π -pulse reverses the sign of the Zeeman Hamiltonian from one 2τ free evolution period to the next. Under the delta function pulse approximation, a π -pulse has no effect on the dipolar coupling term regardless of the number of pulses used. This effectively cancels out the action of \mathcal{H}_Z on the spin system, leaving a T_2 decay curve due only to \mathcal{H}_{zz} . As long as there are no diffusive dynamics at play [10, 28, 30], as in liquids, the multiple pulse CPMG experiment should give an identical decay curve as the Hahn echo experiment.

This argument can also be demonstrated using the density matrix. For the CPMG experiment, the density matrix has the form

$$\rho(t) = \{\mathcal{U}\mathcal{R}_y\mathcal{U}\}^n \rho(0) \{\mathcal{U}^{-1}\mathcal{R}_y^{-1}\mathcal{U}^{-1}\}^n \quad (3.20)$$

where $\mathcal{U} = \mathcal{U}_Z\mathcal{U}_{zz}$ is the unitary operator in equation (3.11) for free evolution and $\rho(0)$ is the state of the density matrix after the initializing $\frac{\pi}{2}$ -pulse.

From the set of equations (3.17)-(3.19), the effect of π -rotations on the free evo-

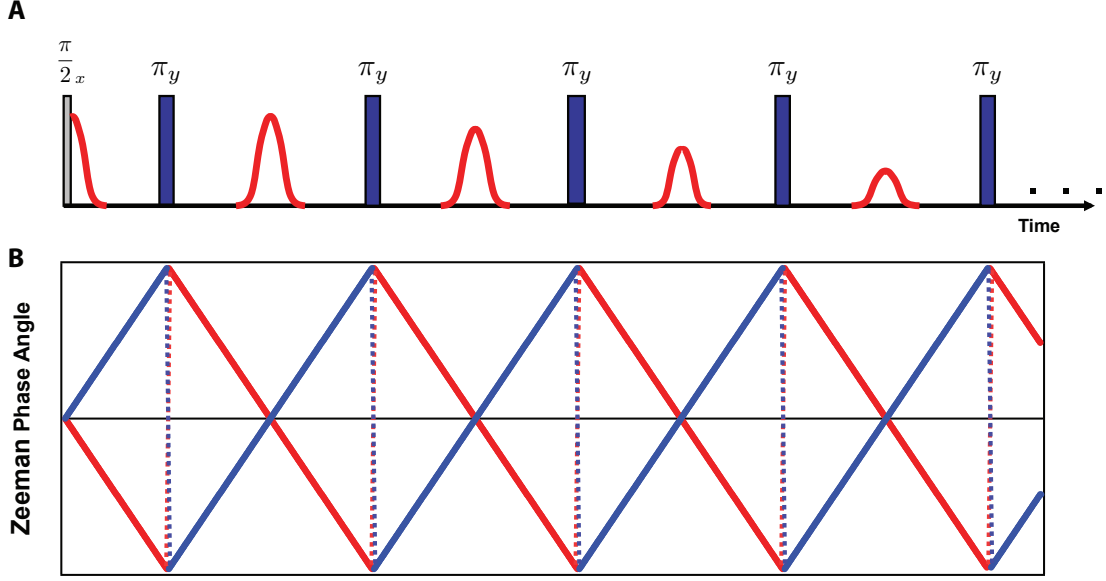


Figure 3.3: **A.** The CPMG experiment: $90_X - \tau - \{180_Y - \tau - \text{echo} - \tau\}^n$. The decay in the spin echo height is a measure of T_2 . **B.** The Zeeman phase angle of two representative spin clusters with precession frequency $\pm \frac{\Omega_z}{\hbar}$. The sign of Ω_z is reversed at each π -pulse causing spins to rephase. A spin echo appears at the point where the Zeeman phase lines cross.

lution unitary operators can be written as

$$\mathcal{R}_y \mathcal{U}_Z \mathcal{R}_y^{-1} = \mathcal{U}_Z^{-1} \quad (3.21)$$

$$\mathcal{R}_y \mathcal{U}_{zz} \mathcal{R}_y^{-1} = \mathcal{U}_{zz} \quad (3.22)$$

Using these expressions in equation (3.20), the density matrix can be simplified to

$$\rho(t) = \{\mathcal{U}_Z \mathcal{U}_{zz} \mathcal{R}_y \mathcal{U}_Z \mathcal{U}_{zz}\}^n \rho(0) \{inv\}^n \quad (3.23)$$

$$= \{\mathcal{U}_Z \mathcal{U}_{zz} \mathcal{R}_y (\mathcal{R}_y^{-1} \mathcal{R}_y) \mathcal{U}_Z \mathcal{U}_{zz} (\mathcal{R}_y^{-1} \mathcal{R}_y)\}^n \rho(0) \{inv\}^n \quad (3.24)$$

$$= \{\mathcal{U}_Z \mathcal{U}_{zz} \mathcal{U}_Z^{-1} \mathcal{U}_{zz} \mathcal{R}_y\}^n \rho(0) \{inv\}^n \quad (3.25)$$

$$= (\mathcal{U}_{zz})^{2n} (\mathcal{R}_y)^n \rho(0) (\mathcal{R}_y^{-1})^n (\mathcal{U}_{zz}^{-1})^{2n} \quad (3.26)$$

where $\{inv\}$ is the inverse of the operators to the left of $\rho(0)$. If the initializing $\frac{\pi}{2}$ -pulse is along $\hat{\mathbf{x}}$, then $\rho(0) = I_y$ and $(\mathcal{R}_y)^n \rho(0) (\mathcal{R}_y^{-1})^n = \rho(0)$ since rotations about $\hat{\mathbf{y}}$ have no effect on I_y . In the delta function pulse approximation, each of the n repeating blocks lasts a time 2τ giving a total elapsed time $t = 2n\tau$. Using these facts, the density matrix further simplifies to

$$\rho(t) = \mathcal{U}_{zz}(t)\rho(0)\mathcal{U}_{zz}^{-1}(t) \quad (3.27)$$

where the time evolution operator for the CPMG experiment is simply $\mathcal{U}_{zz}(t) = e^{\frac{i}{\hbar}\mathcal{H}_{zz}t}$.

Under the delta function pulse approximation, the density matrix evolves only under the dipolar Hamiltonian, independent of the Zeeman shift spread or the number of applied pulses. For $n = 1$, the density matrix is equally valid for the Hahn echo experiment. From equation (3.27) we would expect that a spin system subject to the Hahn Echo and CPMG experiments would evolve under the same dipolar Hamiltonian. However, an extended coherence time was found not only in the ^{29}Si sample shown in Figure 3.1 and other silicon samples [2], but in very different dipolar solids like ^{13}C in C_{60} , ^{89}Y in Y_2O_3 , and electrons in Si:P[3, 22, 31, 32].

3.5 More Unexpected Echoes with Multiple Pulse Experiments

The analysis of the previous section showed that within the delta function pulse approximation, the Hahn echo experiment and the CPMG experiment from Figure 3.1 should agree, although they clearly do not. Even more disconcerting was the fact that this was only one of several surprising experimental results using multiple

pulse sequences on a variety of dipolar solids.

3.5.1 Even-odd Effect

In multiple pulse experiments on dipolar solids where long-lived echoes are observed beyond T_2 , spin locking is often first to be blamed. Continuous wave (cw) spin locking occurs when an initializing 90° pulse is followed by a transverse rf field aligned in the same direction as the freshly rotated spins. The field locks the spins along this axis in the rotating frame, although they still decay with a time constant $T_{1\rho}$ [10, 25]. Spin locking can be done intentionally using a continuous rf field, but can also occur in multiple pulse experiments where $\tau < T_2$ [33, 34, 35, 36]. In pulsed spin locking, the closely spaced pulses generate a time averaged field that can lock the spins in place, preventing free evolution in the transverse plane¹.

In our earliest experiments, there was concern that the π -pulses were somehow holding the magnetization along the measurement axis and producing the long tail shown in the CPMG experiment in Figure 3.1. To reduce the possibility of spin locking, the time delay 2τ between pulses was increased. However, increasing the pulse spacing between the pulses revealed another strange effect. As the spacing was increased, an unevenness in the decay of the echo envelope was observed. For the longest delays between pulses, a pattern developed showing even numbered echoes that were larger in magnitude than the previous odd echo [2, 3, 4].

From the discussion in Section 3.4.2, one would expect the echo peak heights to decay under only the dipolar hamiltonian since Zeeman dephasing is undone by the π -pulses. Therefore, it is particularly startling to observe echoes that are larger in

¹While the long lived CPMG spin echoes from Figure 3.1 resemble the pulsed spin locking experiments, the theoretical explanation of CPMG long-tail effect is quite different. In the following chapter, it will be shown that the key to explaining the long-lived magnetization is not found in the time-averaged effective Hamiltonian ($\mathcal{H}^{(0)}$), but rather the first order term in the Magnus expansion ($\mathcal{H}^{(1)}$).

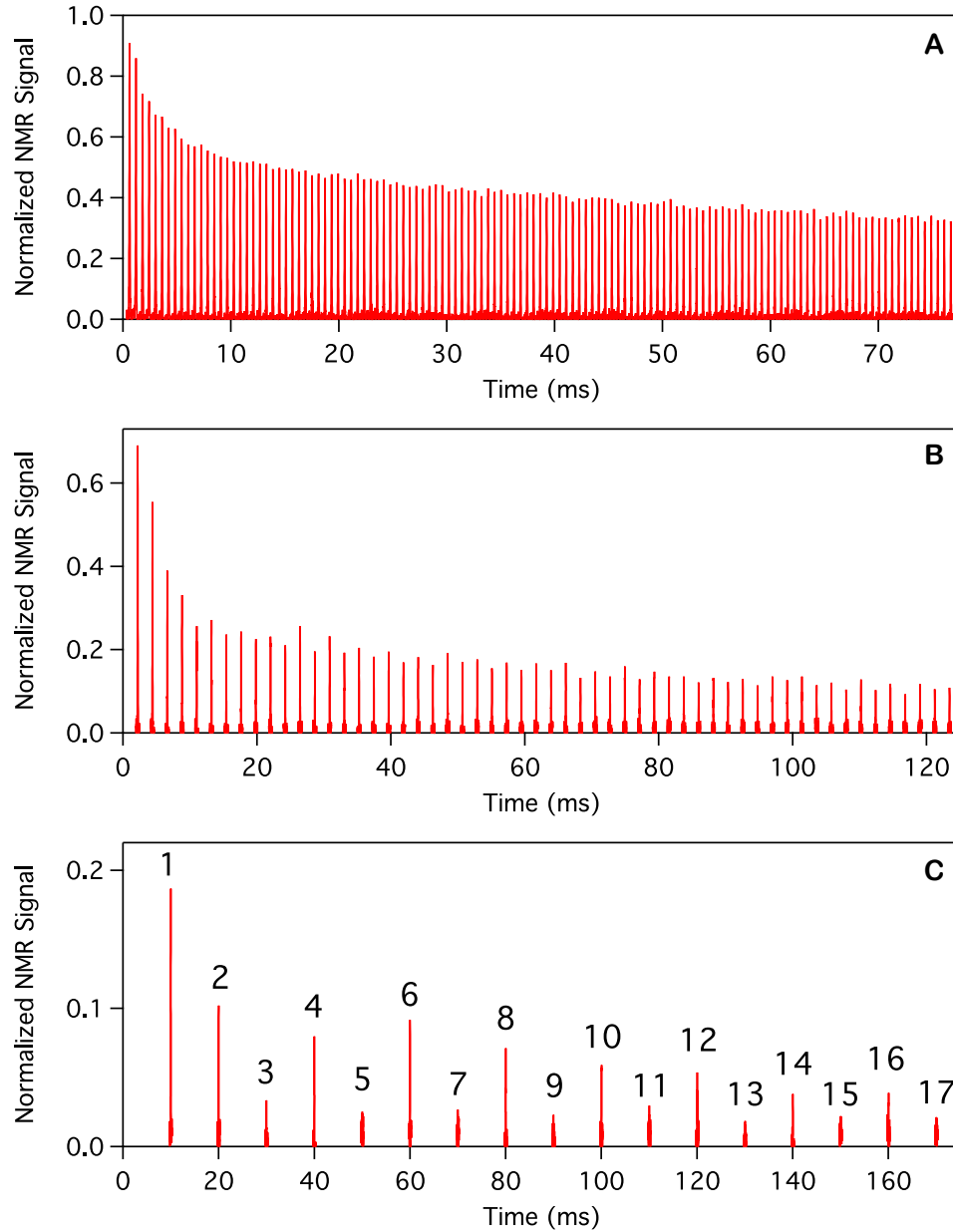


Figure 3.4: CPMG echo trains of ^{29}Si in Si:P (3.94×10^{19} P/cm 3) with three time delays between π pulses. **A.** $2\tau = 592 \mu\text{s}$, **B.** $2\tau = 2.192$ ms and **C.** $2\tau = 9.92$ ms. For comparison, $T_2 = 5.6$ ms in silicon as measured by the Hahn echoes and as predicted by the delta-function pulse approximation. Data taken at room temperature in a 12 Tesla field. From reference [4, 24].

magnitude than echoes that occurred previously.

3.5.2 Pulse Sequence Sensitivity

Implicit in the Hahn Echo analysis in Section 3.4.1 is the freedom to chose the pulse phase of the π -pulses. This is also true for multiple π -pulse experiments, so we define the set of multiple π -pulse experiments

$$\begin{aligned} \text{CP: } & 90_X - \{X, X\}^n \\ \text{APCP: } & 90_X - \{\bar{X}, X\}^n \\ \text{CPMG: } & 90_X - \{Y, Y\}^n \\ \text{APCPMG: } & 90_X - \{\bar{Y}, Y\}^n \end{aligned}$$

where $\{\phi_1, \phi_2\}$ is short hand for

$$\{\tau - 180_{\phi_1} - 2\tau - 180_{\phi_2} - \tau\} \quad (3.28)$$

and \bar{X} and \bar{Y} indicates rotations along $-\hat{x}$ and $-\hat{y}$, respectively. The spin echo is acquired during each 2τ free evolution period. The Carr-Purcell (CP) sequence [28] utilizes a repeating π -pulse along the \hat{x} direction, while the previously introduced Carr-Purcell-Meiboom-Gill (CPMG) experiment [29] features π -pulses along the \hat{y} direction. The alternating phase (AP) versions of these two multiple pulse sequences flip the sign of the π -pulse from one pulse to the next. For the CP and APCP pulse sequences using x -phase π -pulses, spin echoes form along the \hat{y} and $-\hat{y}$ directions [14]. For CPMG and APCPMG, spin echoes form only along \hat{y} .

Within the delta function pulse approximation, all four of these pulse sequences should result in the same decay envelope. However, as Figure 3.5 shows, in physical

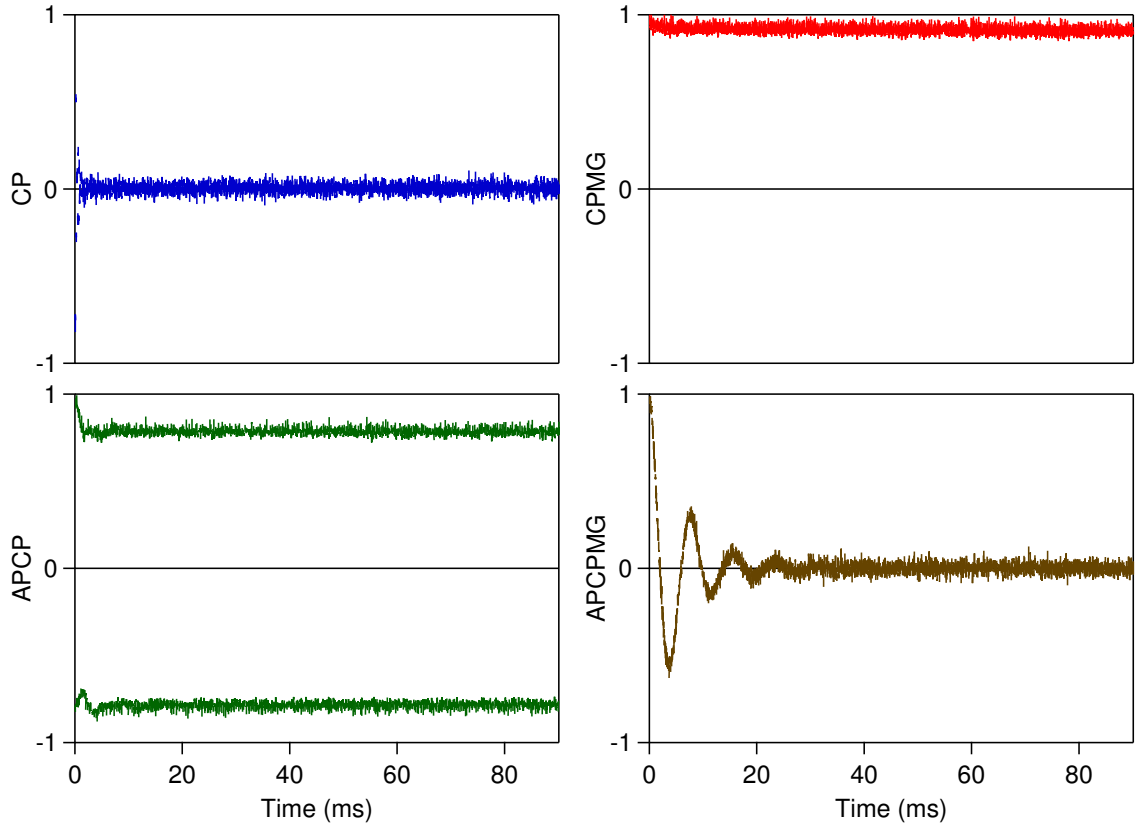


Figure 3.5: NMR pulse sequence sensitivity in Silicon doped with Antimony (Si:Sb, 2.75×10^{17} Sb/cm³) at room temperature. The four pulse sequences with different π -pulse phases, (Top Left) CP, (Top Right) CPMG, (Bottom Left) APCP, (Bottom Right) APCPMG are shown. $2\tau = 72 \mu\text{s}$ and $B^{\text{ext}} = 11.74$ Tesla. From reference [4, 24].

experiments the pulse sequence sensitivity (PSS) is quite dramatic. Signal in the CP and APCPMG experiments quickly decay to zero, while APCP and CPMG show long-lived coherence. Although the condition for strong pulses is satisfied ($\mathcal{H}_{P_\phi} \gg \mathcal{H}_{int}$), we cannot explain the difference between these four experiments within the delta function pulse approximation. The PSS in Figure 3.5 was a strong indicator that the π -pulses were at the root of the unexpected spin echoes and that a breakdown of the delta function approximation was occurring for these multiple π -pulse experiments.

3.6 Beyond the Delta Function Approximation

Under the delta function pulse approximation, instantaneous π -pulses should have no effect on the transverse relaxation time of dipolar solids. For strong pulses where $\mathcal{H}_{P_\phi} \gg \mathcal{H}_{int}$ is satisfied, multiple π -pulse experiments should only refocus the spread in Zeeman shifts, while the measurable signal decays under the dipolar Hamiltonian.

However, we found in the previous set of experiments that this was not the case. In this section, we present our attempts to find the reason for this deviation and how these investigations lead to the theoretical model we use in later chapters.

3.6.1 Experimental Sources

As a first step in understanding the behavior, our group focused its efforts on the possible experimental and sample dependent sources of the unexpected behavior. A large body of work went into exploring extrinsic effects and minimizing experimental imperfection in our experiments. The breadth of these explorations, detailed in reference [3] and Dr. Dale Li's thesis [4], involved extensive studies of pulse timings, rf field homogeneity, rf field strength, phase transients, and composite pulse sequences to reduce pulse error. Despite all the improvements made over the course

of these experiments, the long CPMG tail and PSS remained and could not be linked to experimental imperfections.

In addition to these studies, our group also investigated extrinsic effects that could arise from the material properties of the sample itself. These included studies exploring possible dependence on temperature, spin natural abundance, and a variety of dipolar spin environments [3, 4]. These experiments gave strict constraints on the finite pulse simulations described later in this chapter and the theoretical model used throughout this dissertation. The following experiments are two of the contributions I made in this effort.

Single Crystal Measurements

Most samples tested in these initial experiments were ground into fine powders to minimize the effects of skin depth. Due to the small magnetic susceptibility of silicon [37], each powdered particle would have a slightly different internal field dependent on its individual shape and size. The crushed sample also allowed a random orientation of the lattice within each powdered particle with respect to \vec{B}_0 , giving a distribution of dipolar coupling constants. This leads to magnetic susceptibility broadening and a widened spectral line.

By using a single crystal of Si:Sb (2.75×10^{17} Sb/cm³) as the sample, these line broadening effects would be removed. The single crystal also gives a discrete subset of dipolar coupling constants, depending on the crystal orientation to the large external field. Figure 3.6A shows the spectrum of a single crystal of Si:Sb with the (110) axis oriented along \vec{B}_0 (red spectrum). The small peaks at the foot of the central peak are due to the dipolar coupling of nearest neighbors. The simulation in blue, done by Kenny McKlean, convolves the magnetic susceptibility broadening for the single crystal in the orientation shown in the inset with the dipolar lineshape. The

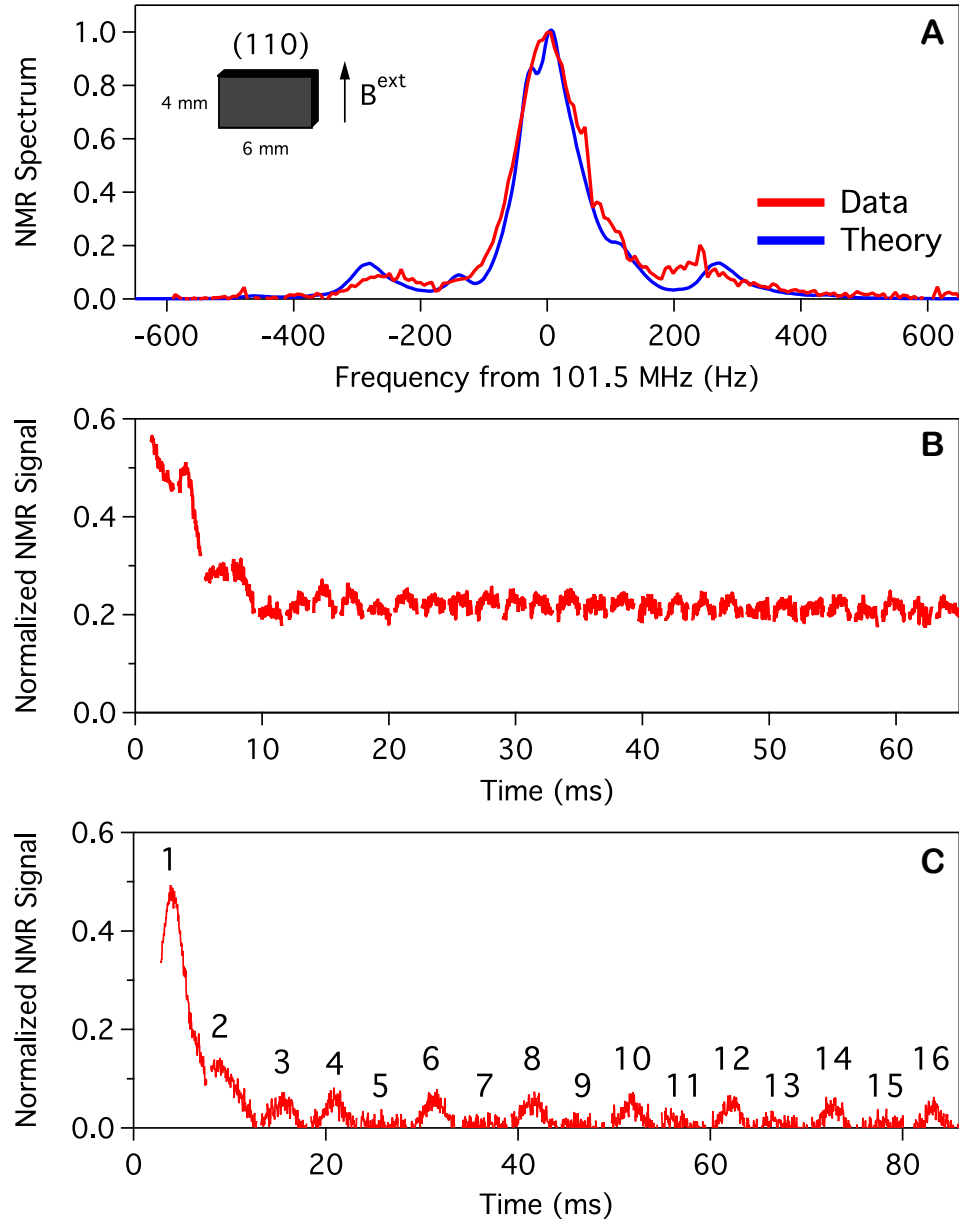


Figure 3.6: NMR data in a single crystal of Si:Sb (2.75×10^{17} Sb/cm³) oriented with the (110) axis along \vec{B}_0 . **A**. NMR spectrum (red) compared to a 6-spin dipolar coupling calculation by Kenneth McKlean that includes magnetic susceptibility broadening and skin depth due to the crystal shape. FWHM = 110Hz. **B** and **C**. CPMG echo trains for (**B**) $2\tau = 2.1$ ms and (**C**) $2\tau = 5.2$ ms. The longer τ spacing shows the even-odd effect. [24]

calculated spectrum, with a FWHM = 110 Hz, is a good fit to the measured spectrum. Also shown are CPMG experiments (Figure 3.6B-C) performed on the single crystal for different τ values, which exhibit the long tail effect and PSS.

These experiments demonstrate that, although the spectral line shape is well understood, the unexpected behaviors still persist. This sample also allowed us to confirm some constraints on the relevant Hamiltonian. The small spread in Ω_z over a macroscopic sample supports the assumption stated in Section 3.2 that a microscopic cluster of $N \leq 10$ spins could be assumed to have essentially the same local field.

Adamantane Experiments

For the small adamantane molecule ($C_{10}H_{16}$), the dipolar coupling between protons dominates the Zeeman broadening over a macroscopic powder sample. Knowing that the dipolar coupling was a key element in the long tail phenomenon under investigation, we wondered what behavior would result in a sample where $\Omega_z \sim 0$ compared to the dipolar coupling.

To quell the fears that pulse errors were contributing to the anomalous behavior, some unusual steps were taken to approach ideal experimental conditions in this sample. While many NMR experiments typically use a 100% filling factor to obtain the most signal, this sample was restricted to a tiny fraction of the coil ($\sim 0.35\%$), making the pulse angle very uniform over the entire sample. The rf field strength was set to approximately ten times the adamantane line width¹ and resistors were added to the NMR tank circuit to lower the quality factor, Q , in order to suppress phase transients. Although lowering Q reduced signal-to-noise even more, it allowed the resonant circuit to follow the step-up and step-down of the rf power at the beginning and end of the pulses much more closely, greatly reducing the influence of transients.

¹Since adamantane has a large FWHM compared to previous samples, we were not able to reach our normal operating range of $B_1/\text{FWHM} \gg 10$ within the limitations of our spectrometer.

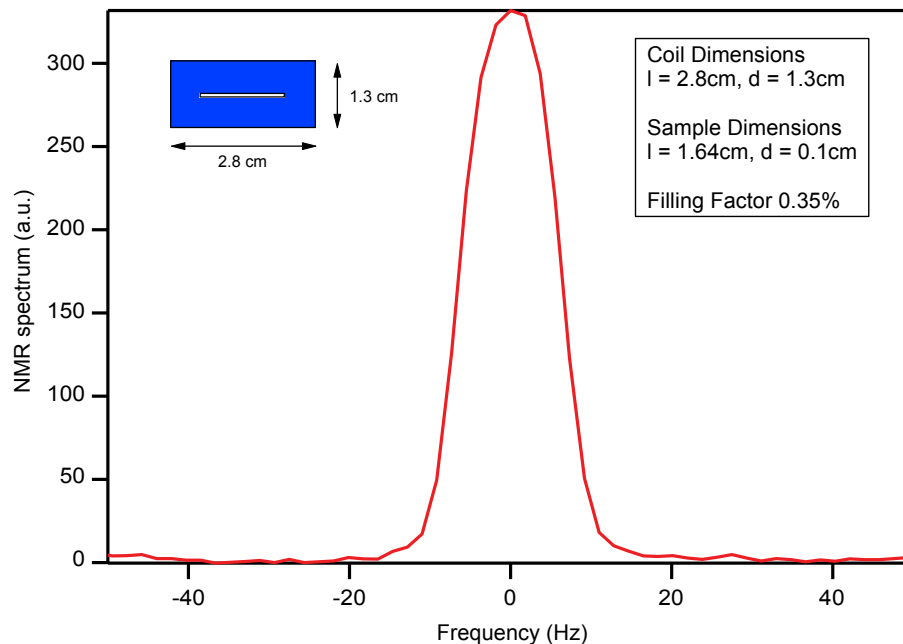


Figure 3.7: Proton (H^1) NMR spectrum at room temperature for the adamantane powder sample ($C_{10}H_{16}$) studied in Figure 3.8. The inset shows the relative size of the NMR sample and the available coil volume. The sample is restricted to a 0.35% filling factor. FWHM ~ 13 kHz, $\frac{\omega_1}{2\pi} \sim 143$ kHz.

Figure 3.7 shows the adamantane spectrum for this particular sample and a scaled diagram comparing the sample size to the available coil size.

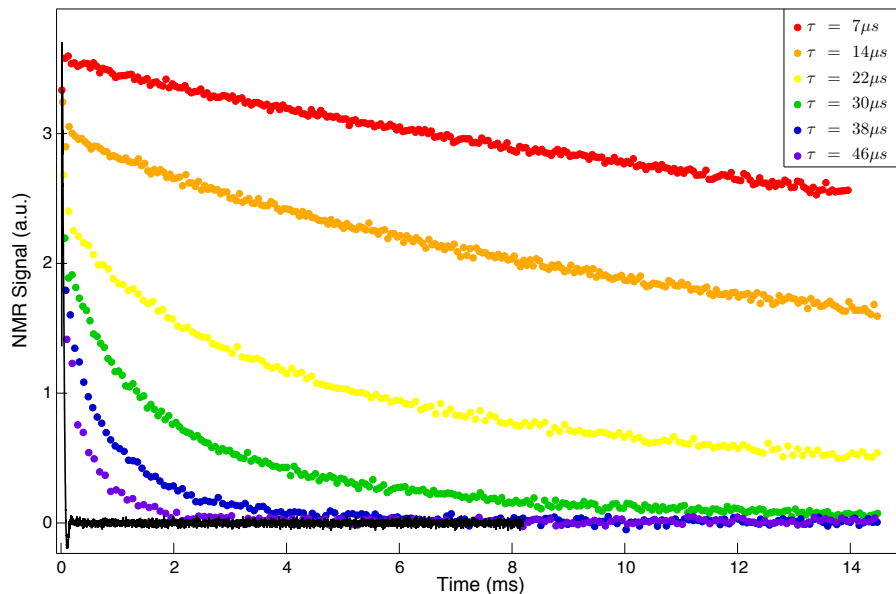


Figure 3.8: Proton (H^1) NMR data of a small adamantane (C_6H_{10}) powder sample, using near ideal conditions from Figure 3.7. The peak of each CPMG echo in the echo train are shown for a series of τ values, with an FID in black for comparison. H^1 linewidth ~ 13 kHz, $\frac{\omega_1}{2\pi} \sim 143$ kHz, $T = 300K$, $B_0 = 12$ Tesla.

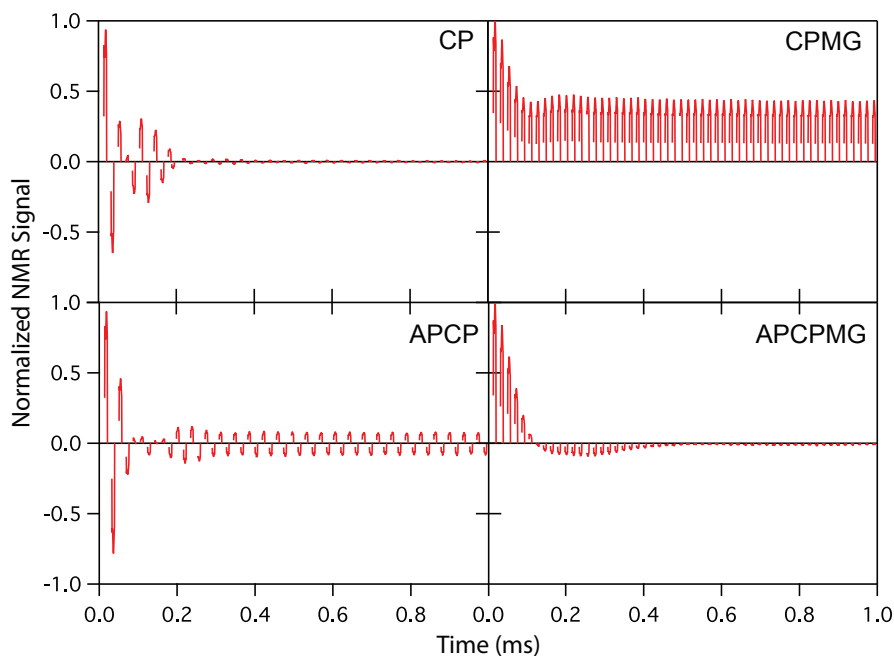


Figure 3.9: Pulse sequence sensitivity in H^1 NMR in adamantane ($C_{10}H_{16}$). CP, CPMG, APCP, APCPMG data of H^1 NMR in adamantane using the same sample and tank circuit as Figure 3.7, but not identical conditions (smaller ω_1 and larger cycle time t_c). H^1 linewidth ~ 13 , $\frac{\omega_1}{2\pi} \sim 114$ kHz, $\tau = 7\mu s$, $T = 300K$, $B_0 = 12$ Tesla.

Figure 3.8 shows CPMG experiments on adamantane in this near ideal sample. For large enough τ , the CPMG echo train decays quickly due to dipolar coupling. As τ is decreased and more pulses are applied, the fast decay due to the dipolar coupling is replaced by a long tail in the CPMG echo train. Pulse sequence sensitivity is also observed in the same sample under slightly different conditions as shown in Figure 3.9.

Because of the unusual steps to prevent experimental artifacts, these sets of experiments were strong support that the unexpected behavior was not the result of pulse error or other extrinsic sources. Additionally, the large dipolar coupling in this sample with negligible Zeeman shift supported our belief that the observed anomalous behavior was primarily due to the dipolar coupling acting in conjunction with the pulse rf field term when many pulses are applied.¹

3.6.2 Exact Calculations for Finite Pulses

In parallel with these experiments, the exact evolution of the density matrix was calculated numerically using the appropriate Hamiltonian with realistic experimental parameters. Having observed anomalously long spin coherence times in many different samples and carefully calibrating and measuring our pulses [3], we felt confident in the parameters to use in exact calculations.

Observing nearly identical CPMG long tail behavior in a variety of silicon samples with different dopant concentrations and different dopant types [2], as well as in different dipolar solids like ^{13}C in C_{60} and ^{89}Y in Y_2O_3 [3], was strong empirical evidence that the errant spin evolution was connected to the homonuclear spin-spin coupling. These experiments put strong constraints on the relevant form of the Hamiltonian in these samples. Specifically, the internal Hamiltonian need only include the Zeeman

¹This was later confirmed by many simulations using $\Omega_z = 0$ that showed the long tail and PSS behavior [4, 5].

and dipolar coupling terms,

$$\mathcal{H}_{int} = \Omega_z I_{z_T} + \mathcal{H}_{zz}. \quad (3.29)$$

When pulses are applied, we no longer drop \mathcal{H}_{int} even though it is true that $\mathcal{H}_{P_\phi} \gg \mathcal{H}_{int}$. During a pulse, the full Hamiltonian then has the form

$$\mathcal{H}_{tot} = \Omega_z I_{z_T} + \mathcal{H}_{zz} - \hbar\omega_1 I_{\phi_T} \quad (3.30)$$

where the pulse time t_p and ω_1 are set by the pulses used. If the delta function pulse approximation is no longer made, what effect does \mathcal{H}_{int} have during a strong pulse with finite strength and non-zero duration?

To answer this question, a full density matrix calculation can be done to determine the observable $\langle I_y(t) \rangle$. Figure 3.10 shows exact calculations for the four pulse sequences from Section 3.5.2 on the silicon lattice using the actual experimental parameters. For a single disorder realization (DR), the ^{29}Si lattice is randomly populated with spins according to its 4.67% natural abundance and is randomly oriented to the large external field [24]. For each DR, Ω_z is drawn from a Gaussian distribution with the FWHM of the realistic Zeeman spread. The full simulation show in Figure 3.10 is calculated for $N = 7$ spins, averaging over 1000 DRs.

For comparison, Figure 3.10 also shows the experiments these simulations aim to reproduce and as well as simulations for delta function π pulses (in black) which turns off the Zeeman and dipolar terms when pulses are applied. Unfortunately, when using the realistic experimental parameters in the simulations, the signal decay appears close to the decay curves calculated for delta function π pulses, rather than the experimental results. It was, in fact, not all that surprising to see how close these simulations were to the delta function pulse approximation since the pulse strength

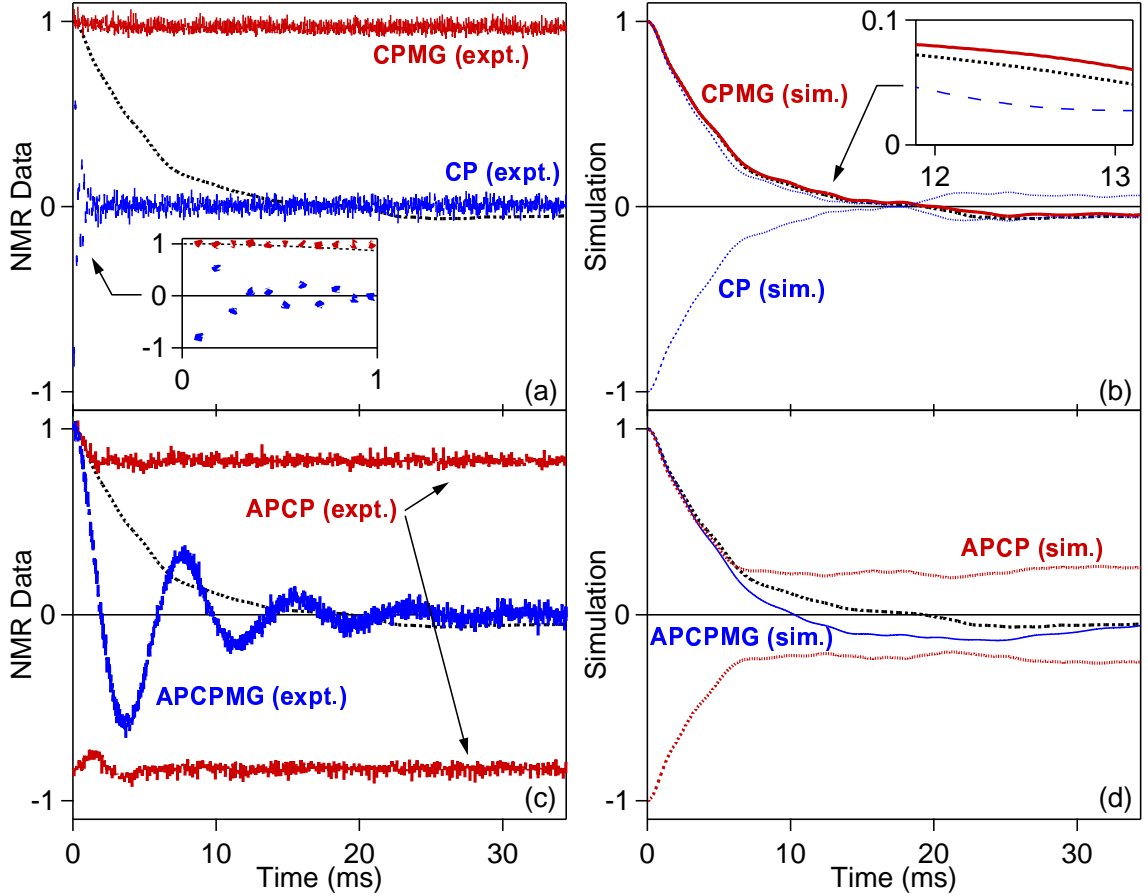


Figure 3.10: **(a,c)** ^{29}Si measurements in Si:Sb with the four phase choices from Section 3.5.2. **(b,d)** $N = 7$ simulations for the same experimental conditions: $t_p = 14\mu\text{s}$, $\tau = 36\mu\text{s}$ and $\frac{\omega_1}{2\pi} = 35.7$ kHz in a 11.75 Telsa field at room temperature. For each of the 1000 disorder realizations, Ω_z/h is drawn from a 290 Hz FWHM gaussian and typical dipolar couplings $\frac{|B_{12}|}{h} \approx 44.5$ Hz, $\frac{|B_{17}|}{h} \approx 3.5$ Hz). Inset **(a)** shows rapid decay of CP data. Inset **(b)** shows distinction between CP and CPMG simulation. The black dashed reference **(a-d)** sets $\Omega_z = 0$ and turns \mathcal{H}_{zz} off during each pulse. From reference [3].

for these simulations and experiments is over 100 times the natural line width in this sample.

However, these exact calculations did show a small effect in the right direction (Figure 3.10 **b** and **d**), although the deviation was frustratingly small and did not compare well to our experiments. Despite the obvious incongruity, there was some consolation in the fact that the deviation showed the right trend and, more importantly, that the deviation came solely from the full Hamiltonian in equation (3.30) acting during finite time duration of pulses. Since no pulse imperfections were assumed in the simulations, these simulations showed that this effect, though small, could come from the internal Hamiltonian itself.

3.6.3 Finding the Long Tail in Simulations

Taking inspiration from the exact calculations, we searched for ways to amplify this effect in simulations. The first success came from inflating the dipolar coupling above the natural ^{29}Si coupling strength. We were first inspired to try this by the results in ^1H NMR experiments on liquid crystal [5] since protons have a much larger dipolar coupling strength. It was under these inflated dipolar coupling conditions that we first saw simulations with behaviors similar to what was seen in experiments.

Figure 3.11 shows pulse sequence sensitivity in simulations where the dipolar coupling strength is scaled up by a factor of 25 for the four pulse sequences CPMG, APCPMG, CP and APCP. The simulations assume strong, but finite π pulses so that both the internal Hamiltonian, \mathcal{H}_{int} , and the rf field term, \mathcal{H}_{P_ϕ} , act when pulses are applied. Compared to Figure 3.10, these simulations show similar behavior to the experiments; CPMG and APCP show a long tail, while CP and APCPMG decay quickly to zero. It is important to emphasize again that no extrinsic imperfections were assumed in the simulations. The pulse sequence sensitivity shown in Figure

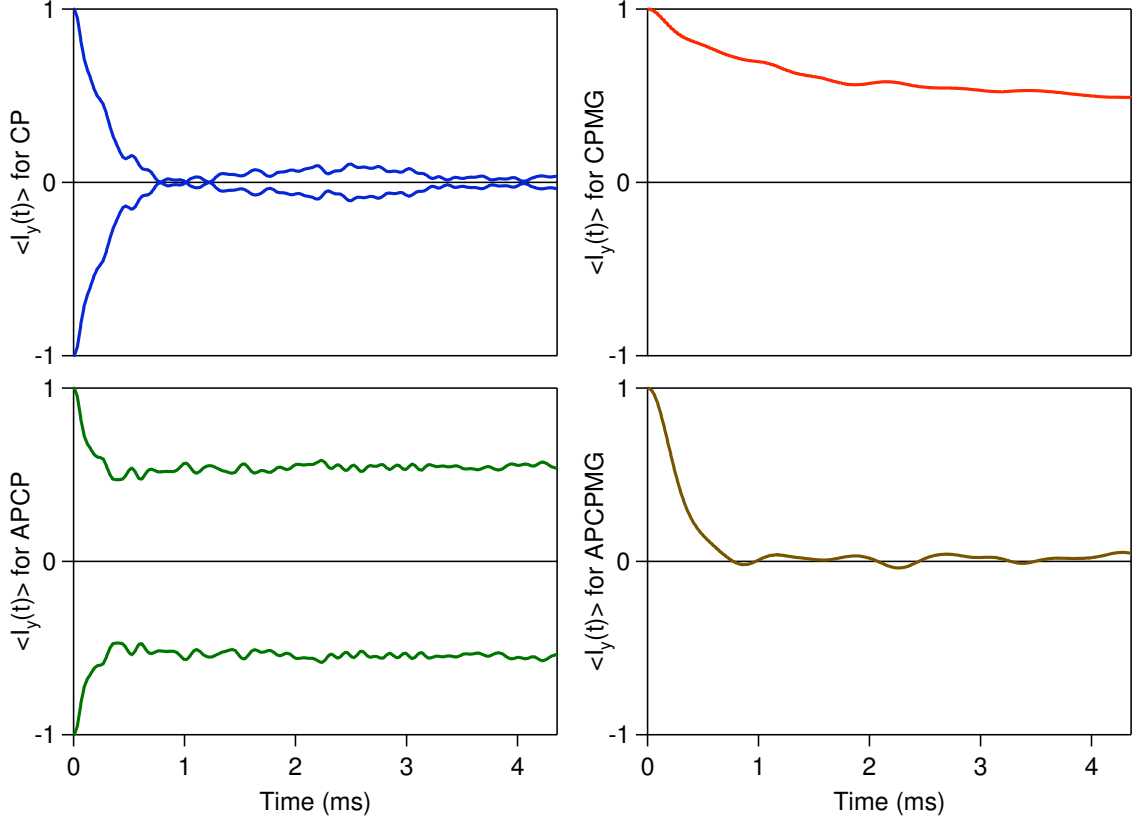


Figure 3.11: Exact calculations using strong but finite π pulses. Calculations use parameters: $N = 6$ spins, simulated pulse strength $H_1 = 40$ kHz ($t_p = 12.5 \mu\text{s}$), delay between π pulses $2\tau = 2 \mu\text{s}$, dipolar coupling scaled by $25 \times B_{jk}$ of ^{29}Si , Zeeman shift Ω_z/h drawn from a 3 kHz wide Gaussian for each DR, and the disorder average is taken over 150 DRs. The full lineshape is 4 kHz, which is a convolution of the pure dipolar line of 2.2 kHz and the Zeeman spread of 3 kHz. CPMG and APCP display long-lived tails while CP and APCPMG decay to zero. From reference [4, 24].

3.11 comes solely from the presence of the full Hamiltonian in equation (3.30) acting during finite time duration of pulses.

Although it was a relief to find that altering these and other parameters in simulations could produce behaviors reminiscent of the experiments [4, 5, 24], it was still disconcerting that these simulations did not use realistic parameters for the silicon lattice initially studied. Many simulations were done exploring the effect of these parameters [4, 5, 24], but did not help build an intuitive understanding of the behavior. To find the underlying mechanisms causing the long tail and pulse sequence sensitiv-

ity, an analytic description was needed. For this, we turned to average Hamiltonian theory, introduced in the next chapter.

Chapter 4

Average Hamiltonian Theory

Coherent averaging theory, now more commonly called average Hamiltonian theory, has proven itself as a powerful tool in the analysis and development of high resolution pulsed NMR [25, 26, 38]. Historically, average Hamiltonian theory was introduced as a way to describe and help develop sequences aimed at selectively averaging out large scale effects in favor of much smaller interactions of interest [26, 39, 40]. It allows the experimenter to manipulate the effective Hamiltonian by her choice of pulse intensity, direction and timing. It also allows the simple description of other NMR effects, such as spin locking and magic echoes [42, 43], involving the application of long steady pulses. Because it can provide a simplified picture of the evolution of a complex spin system under the application of a repeating train of pulses, we hoped it could help us gain some insight into the unexpected spin echo behavior in both experiments and exact calculations described in Chapter 3.

In this chapter, we show how this analytic tool built to describe systems evolving under the influence of a time-dependent periodic perturbation, will help us gain some insight into the unexpected behavior of the last chapter. After a general introduction to average Hamiltonian theory, we will apply this powerful tool to the four multiple pulse experiments in question. Clues from exact simulations [3, 4, 5] showed that

the source of the divergent behavior could be the finite duration of the pulses, where the delta function approximation predicts that the four sequences should agree in the limit of strong pulses. In this analysis, we will calculate the terms that are ordinarily ignored in the strong pulse limit, and see if they can help explain the unexpected behavior.

4.1 Averaging in the Interaction Frame

In those cases where the Hamiltonian separates naturally into two parts, such as a time-dependent and a time-independent part or a larger scale term and a small perturbative term, the interaction frame can be useful. The interaction frame is an intermediate representation between the Schrodinger picture and the Heisenberg picture, where the time evolution of the system is shared between the operators and the quantum states. The Hamiltonian can be written as the sum of its time independent and time dependent parts,

$$\mathcal{H}_{tot} = \mathcal{H}_0 + \mathcal{H}_1(t). \quad (4.1)$$

The general time evolution operator is

$$\mathcal{U}_{tot}(t) = T \exp \left[-\frac{i}{\hbar} \int_0^t dt' \mathcal{H}_{tot}(t') \right] \quad (4.2)$$

where T is the Dyson time ordering operator. In a suitable, carefully chosen interaction frame, the interesting part of a spin interaction (e.g. T_2 relaxation) can be preserved, while a trivial interaction (e.g. the Larmor precession) or unwanted interaction can be suppressed. In order to achieve the simplification, the effects of the two parts of the Hamiltonian need to be separated. This is done by splitting the the time

evolution operator into a product of two terms,

$$\mathcal{U}_{tot}(t) = \mathcal{U}_1(t)\mathcal{U}_0(t). \quad (4.3)$$

The terms are defined as

$$\mathcal{U}_1(t) = T \exp \left[-\frac{i}{\hbar} \int_0^t dt' \mathcal{H}_1(t') \right] \quad (4.4)$$

$$\mathcal{U}_0(t) = T \exp \left[-\frac{i}{\hbar} \int_0^t dt' \tilde{\mathcal{H}}_0(t') \right] \quad (4.5)$$

$$\tilde{\mathcal{H}}_0(t) = \mathcal{U}_1^{-1}(t)\mathcal{H}_0\mathcal{U}_1(t) \quad (4.6)$$

where $\tilde{\mathcal{H}}_0(t)$ is the Hamiltonian in the time dependent toggling frame [13, 25, 38] or interaction frame of \mathcal{H}_1 . If we require that the time dependent Hamiltonian \mathcal{H}_1 is periodic in time with period t_c ,

$$\mathcal{H}_1(t + nt_c) = \mathcal{H}_1(t) \quad \text{for } n = 0, 1, 2, \dots \quad (4.7)$$

and that \mathcal{H}_1 is cyclic, meaning that

$$\mathcal{U}_1(t_c) = 1 \quad (4.8)$$

then the perturbing Hamiltonian term \mathcal{H}_1 has no overall direct effect at the end of one full cycle. In other words, $\tilde{\mathcal{H}}_0$ returns to its original value after each t_c since the toggling frame returns to its original orientation. This greatly simplifies the time-evolution operator to a single exponential, provided that the system is observed stroboscopically, only at intervals of t_c . Using the Magnus expansion [44], the unitary

operator can be written

$$\mathcal{U}_{tot}(nt_c) = \mathcal{U}_0(t_c)^n = \exp \left[-\frac{i}{\hbar} \bar{\mathcal{H}} nt_c \right] \quad (4.9)$$

where $\bar{\mathcal{H}}$ is given by

$$\bar{\mathcal{H}} = \bar{\mathcal{H}}^{(0)} + \bar{\mathcal{H}}^{(1)} + \bar{\mathcal{H}}^{(2)} + \dots \quad (4.10)$$

The first three terms of the average Hamiltonian expansion are

$$\bar{\mathcal{H}}^{(0)} = \frac{1}{t_c} \int_0^{t_c} dt \tilde{\mathcal{H}}_0(t) \quad (4.11)$$

$$\bar{\mathcal{H}}^{(1)} = -\frac{i}{2\hbar t_c} \int_0^{t_c} dt_2 \int_0^{t_2} dt_1 \left[\tilde{\mathcal{H}}_0(t_2), \tilde{\mathcal{H}}_0(t_1) \right] \quad (4.12)$$

$$\begin{aligned} \bar{\mathcal{H}}^{(2)} = & -\frac{1}{6\hbar^2 t_c} \int_0^{t_c} dt_3 \int_0^{t_3} dt_2 \int_0^{t_2} dt_1 \left\{ \left[\tilde{\mathcal{H}}_0(t_3), \left[\tilde{\mathcal{H}}_0(t_2), \tilde{\mathcal{H}}_0(t_1) \right] \right] \right. \\ & \left. + \left[\tilde{\mathcal{H}}_0(t_1), \left[\tilde{\mathcal{H}}_0(t_2), \tilde{\mathcal{H}}_0(t_3) \right] \right] \right\}. \end{aligned} \quad (4.13)$$

Average Hamiltonian theory simplifies the time evolution operator from a product of many Hamiltonian exponentials that may not commute, to a single exponential. Another advantage is that the terms in the average Hamiltonian are time independent, and the sum of all the terms describe exactly the evolution of the density matrix at multiples of the cycle time t_c . Although the evolution is determined by a single exponential operator, the disadvantage is that the exponent has an infinite number of terms. Fortunately, under the right conditions, the exact expression can be approximated by the first few terms [10, 13, 26, 38]. In general, the complicated higher order terms may add interactions that are unwanted, but these will have less and less impact as t_c is made smaller.

4.2 Truncation of Internal Hamiltonians

Average Hamiltonian theory can also be useful in systems in which one part of the Hamiltonian is much larger in scale and the other can be viewed as a perturbation. In fact, the secular dipolar Hamiltonian in equation (3.7) is itself an average Hamiltonian in the interaction frame of large Zeeman Hamiltonian, \mathcal{H}_Z [45]. As a simple example, we can apply average Hamiltonian theory to a dipolar coupled system in a large Zeeman field.

In the laboratory frame, the Hamiltonian of two dipolar coupled like-spins has the form

$$\mathcal{H} = \mathcal{H}_Z + \mathcal{H}_d \quad (4.14)$$

where

$$\mathcal{H}_Z = -\hbar\omega_0(I_{z_1} + I_{z_2}) \quad (4.15)$$

$$\mathcal{H}_d = \frac{\gamma^2\hbar^2}{r^3} \left\{ \left(\vec{I}_1 \cdot \vec{I}_2 \right) - \frac{3 \left(\vec{I}_1 \cdot \vec{r} \right) \left(\vec{I}_2 \cdot \vec{r} \right)}{r^2} \right\}. \quad (4.16)$$

It was previously argued in Section 3.2.2 that in a frame rotating at ω_0 the non-secular dipolar terms C, D, E and F in equation (3.6) oscillate at the large frequencies ω_0 and $2\omega_0$ and can therefore be ignored. This argument can be made more rigorous using average Hamiltonian theory. In an average Hamiltonian analysis, coherent averaging takes place in the toggling frame of the dominant \mathcal{H}_Z term. In this frame, $\tilde{\mathcal{H}}_d$ becomes time dependent.

Following the formalism of Section 4.1, the time evolution operator is separated into two parts.

$$\mathcal{U}_{tot} = \mathcal{U}_Z \mathcal{U}_d. \quad (4.17)$$

In this case, since we are going into the toggling frame of the dominant Zeeman Hamiltonian, \mathcal{H}_Z takes the place of the time-dependent external part of the Hamiltonian (\mathcal{H}_1 in equation (4.1)) while \mathcal{H}_d takes the place of the small time-independent, internal part of the Hamiltonian (\mathcal{H}_0 in equation (4.1)). The propagators are

$$\mathcal{U}_Z(t) = \exp \{i(I_{z_1} + I_{z_2})\omega_0 t\} \quad (4.18)$$

$$\mathcal{U}_d(t) = T \exp \left\{ -\frac{i}{\hbar} \int_0^t dt' \tilde{\mathcal{H}}_d(t') \right\} \quad (4.19)$$

with

$$\tilde{\mathcal{H}}_d(t) = \mathcal{U}_Z^{-1}(t) \mathcal{H}_d \mathcal{U}_Z(t). \quad (4.20)$$

To express the full dipolar Hamiltonian in the toggling frame, we need the following well-known relations

$$e^{-iI_z \varphi} I_z e^{iI_z \varphi} = I_z \quad (4.21)$$

$$e^{-iI_z \varphi} I^+ e^{iI_z \varphi} = I^+ e^{-i\varphi} \quad (4.22)$$

$$e^{-iI_z \varphi} I^- e^{iI_z \varphi} = I^- e^{i\varphi}. \quad (4.23)$$

Rewriting the dipolar alphabet in equation (3.6) in the toggling frame and using

$\varphi = \omega_0 t$ in the above equations gives

$$\begin{aligned}
\tilde{A} &= I_{1_z} I_{2_z} (1 - 3 \cos^2 \theta) \\
\tilde{B} &= -\frac{1}{4} (I_1^+ I_2^- + I_1^- I_2^+) (1 - 3 \cos^2 \theta) \\
\tilde{C} &= -\frac{3}{2} (I_1^+ I_{2_z} + I_{1_z} I_2^+) \sin \theta \cos \theta e^{-i(\phi - \omega_0 t)} \\
\tilde{D} &= -\frac{3}{2} (I_1^- I_{2_z} + I_{1_z} I_2^-) \sin \theta \cos \theta e^{i(\phi + \omega_0 t)} \\
\tilde{E} &= -\frac{3}{4} I_1^+ I_2^+ \sin^2 \theta e^{-i2(\phi - \omega_0 t)} \\
\tilde{F} &= -\frac{3}{4} I_1^- I_2^- \sin^2 \theta e^{i2(\phi + \omega_0 t)}.
\end{aligned} \tag{4.24}$$

When \mathcal{H}_d is sandwiched between \mathcal{U}_Z^{-1} and \mathcal{U}_Z , the last four terms pick up a periodic time dependence while the first two terms remain time independent. The zeroth order average Hamiltonian is then

$$\bar{\mathcal{H}}^{(0)} = \frac{1}{t_c} \int_0^{t_c} dt \tilde{\mathcal{H}}_d(t). \tag{4.25}$$

Integrating over one period, $t_c = \frac{2\pi}{\omega_0}$, gives the zeroth order average Hamiltonian. All terms except \tilde{A} and \tilde{B} average to zero, leaving the familiar expression for the truncated dipolar Hamiltonian

$$\bar{\mathcal{H}}_d^{(0)} = \frac{1}{2} \frac{\gamma^2 \hbar^2}{r^3} (1 - 3 \cos^2 \theta) (3 I_{1_z} I_{2_z} - \vec{I}_1 \cdot \vec{I}_2) \tag{4.26}$$

which is easily scaled up for the N-spin system in equation (3.7). The requirement for stroboscopic observation need not be so strict if t_c is very small, corresponding to a high field limit.

4.3 Average Hamiltonian for Finite Pulses

Average Hamiltonian theory is particularly useful in analyzing and designing multiple pulse sequences. Each pulse in the sequence rotates the toggling frame to a different orientation. Between pulses, the system is allowed to freely evolve. During these intervals, $\tilde{\mathcal{H}}_0$ remains constant but depends on the previous applied pulses. In this way, multiple pulse sequences can be used as a tool to manipulate Hamiltonians and the evolution of the systems they govern.

For the multiple pulse sequences of Section 3.5.2, the Hamiltonian has the time dependent form

$$\mathcal{H}_{tot}(t) = \mathcal{H}_Z + \mathcal{H}_{zz} - \hbar\omega(t)I_{\phi_T} \quad (4.27)$$

where $\omega(t) = \omega_1$ during an applied pulse along ϕ and zero during free evolution. The first two terms are taken as the time independent, internal Hamiltonian $\mathcal{H}_0 = \mathcal{H}_{int} = \mathcal{H}_Z + \mathcal{H}_{zz}$, where \mathcal{H}_Z is the Zeeman Hamiltonian in equation (3.3) and \mathcal{H}_{zz} is the secular dipolar Hamiltonian in equation (3.7). The applied pulse term is the time dependent external Hamiltonian, $\mathcal{H}_1 = \mathcal{H}_{rf} = -\hbar\omega(t)I_{\phi_T}$. The spin operator lies in the transverse plane and can be written $I_{\phi_T} = \cos\phi I_{x_T} + \sin\phi I_{y_T}$, although in practice the pulse is typically applied along either the x - or y -axis.

In the case of infinitely strong pulses, H_{int} can be neglected in comparison to H_{rf} when the pulse is on. For an infinitely strong pulse, H_{rf} produces perfect spin rotations, while between pulses the density matrix develops under the time independent H_{int} . This approximation is conventionally made whenever pulses are very strong compared to the Zeeman line-width ($\omega_1 \gg \frac{\Omega_z}{\hbar}$). Although we will not assume perfect rotations in the following analysis, this strong pulse condition along with small enough t_c allows us to keep just the first few terms in the average Hamiltonian expansion in equation (4.10).

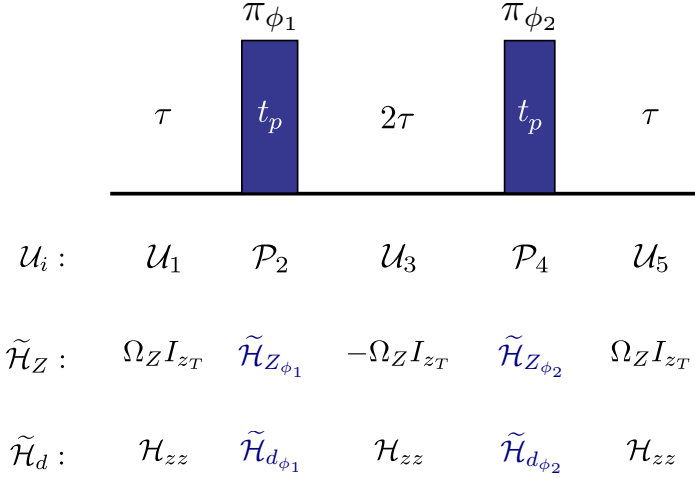


Figure 4.1: The $\{\phi_1, \phi_2\}$ multiple π -pulse sequence. Each cycle has a total length $t_c = 4\tau + 2t_p$, where 2τ is the free evolution time between pulses and t_p is the duration of the pulse. \mathcal{U}_i are the time evolution operators describing the different events in the sequence. The toggling frame Hamiltonians, $\tilde{\mathcal{H}}_Z$ and $\tilde{\mathcal{H}}_d$, for the free evolution periods are identical for all four pulse sequences, $\{Y, Y\}$, $\{\bar{Y}, Y\}$, $\{X, X\}$ and $\{\bar{X}, X\}$, but differ during the pulse events.

4.3.1 Toggling Frame Hamiltonians

Using the formalism outlined in Section 4.1, we can analyze the general repeating π -pulse sequence, $\{\phi_1, \phi_2\}$, defined by equation (3.28) and shown in Figure 4.1. As an example, for the $\{Y, Y\}$ pulse block repeated n times, the total time evolution operator for the system is

$$\mathcal{U}_{tot} = \{\mathcal{U}_5 \mathcal{P}_4 \mathcal{U}_3 \mathcal{P}_2 \mathcal{U}_1\}^n \quad (4.28)$$

where \mathcal{U}_1 , \mathcal{U}_3 and \mathcal{U}_5 are the transformation operators during the free evolution periods and \mathcal{P}_2 and \mathcal{P}_4 are both π -pulses along \hat{y} . It is important to note that all three terms in equation (3.15) are retained during the pulse events since we are not using the delta function pulse approximation.

The Hamiltonian is constant within each of the five events so that the toggling frame Hamiltonians [equation (4.6)] during the different time intervals, t_i , can be

computed in a stepwise manner

$$\tilde{\mathcal{H}}(t_1) = \mathcal{U}_1^{-1} \mathcal{H}_{int} \mathcal{U}_1 \quad (4.29)$$

$$\tilde{\mathcal{H}}(t_2) = \mathcal{U}_1^{-1} \mathcal{P}_2^{-1} \mathcal{H}_{int} \mathcal{P}_2 \mathcal{U}_1 \quad (4.30)$$

$$\tilde{\mathcal{H}}(t_3) = \mathcal{U}_1^{-1} \mathcal{P}_2^{-1} \mathcal{U}_3^{-1} \mathcal{H}_{int} \mathcal{U}_3 \mathcal{P}_2 \mathcal{U}_1 \quad (4.31)$$

....

Because of the time ordering operator in equation (4.4) for $\mathcal{U}_{rf}(t)$ and the structure of the interaction frame, the operators are applied to \mathcal{H}_{int} in reverse time-ordering and an opposite sense of rotation to find the toggling frame Hamiltonian.

During the first event, as well as the free evolution periods in the third and fifth time interval, no pulse is applied so that $\mathcal{H}_{rf} = 0$. From equation (4.4), it is clear that $\mathcal{U}_1 = \mathcal{U}_3 = \mathcal{U}_5 = 1$ and the toggling frame Hamiltonian from equation (4.6) in first time interval is just $\mathcal{H}_{int} = \mathcal{H}_Z + \mathcal{H}_{zz}$.

In the second interval, the unitary operator is

$$\mathcal{U}_1 \mathcal{P}_2(t_2) = \mathcal{P}_2(t_2) = e^{+iI_y \omega_1 t_2}. \quad (4.32)$$

We can apply this evolution operator to the two parts of $\mathcal{H}_{int} = \mathcal{H}_Z + \mathcal{H}_{zz}$ one by one. Using $\theta = \omega_1 t_2$, the action of this evolution operator on $\mathcal{H}_Z = \Omega_z I_{zT}$ is

$$\Omega_z I_{zT} \rightarrow \Omega_z (I_{zT} \cos \theta + I_{xT} \sin \theta). \quad (4.33)$$

The action on the secular dipolar Hamiltonian,

$$\mathcal{H}_d = \sum_{i=1}^N \sum_{j>i}^N B_{ij} \left(3I_{z_i} I_{z_j} - \vec{\mathbf{I}}_i \cdot \vec{\mathbf{I}}_j \right) \quad (4.34)$$

is a bit more complicated. However, only the first term needs transformation since the scalar $\vec{I}_i \cdot \vec{I}_j$ is invariant under rotation. Under the action of $\mathcal{P}_2(t_2)$, the first term transforms as

$$3I_{z_i}I_{z_j} \rightarrow 3(I_{z_i}I_{z_j} \cos^2 \theta + I_{x_i}I_{x_j} \sin^2 \theta + (I_{z_i}I_{x_j} + I_{x_i}I_{z_j}) \cos \theta \sin \theta). \quad (4.35)$$

Subtracting the scalar $\vec{I}_i \cdot \vec{I}_j = I_{x_i}I_{x_j} + I_{y_i}I_{y_j} + I_{z_i}I_{z_j}$ from equation (4.35) and collecting terms gives the dipolar Hamiltonian in the toggling frame

$$\begin{aligned} \tilde{\mathcal{H}}_d = \sum_{i=1}^N \sum_{j>i}^N B_{ij} [I_{z_i}I_{z_j} (\frac{1}{2} + \frac{3}{2} \cos(2\theta)) + I_{x_i}I_{x_j} (\frac{1}{2} - \frac{3}{2} \cos(2\theta)) \\ - I_{y_i}I_{y_j} + \frac{3}{2} (I_{z_i}I_{x_j} + I_{x_i}I_{z_j}) \sin 2\theta] \end{aligned} \quad (4.36)$$

$$= -\frac{1}{2} \mathcal{H}_{yy} + \mathcal{H}_y^S \cos(2\theta) + \mathcal{H}_y^A \sin(2\theta) \quad (4.37)$$

where the following have been defined

$$\mathcal{H}_{yy} \equiv \sum_{i=1}^N \sum_{j>k}^N B_{ij} (3I_{y_i}I_{y_j} - \vec{I}_i \cdot \vec{I}_j) \quad (4.38)$$

$$\mathcal{H}_y^S \equiv \frac{3}{2} \sum_{i=1}^N \sum_{j>k}^N B_{ij} (I_{z_i}I_{z_j} - I_{x_i}I_{x_j}) \quad (4.39)$$

$$\mathcal{H}_y^A \equiv \frac{3}{2} \sum_{i=1}^N \sum_{j>k}^N B_{ij} (I_{x_i}I_{z_j} + I_{z_i}I_{x_j}). \quad (4.40)$$

In the third interval, the system is again allowed to freely evolve, so we need only make the transformation according to

$$\mathcal{U}_1 \mathcal{P}_2(t_p) \mathcal{U}_3 = P_2(t_p) = e^{+i\pi I_y} \quad (4.41)$$

where $\omega_1 t_p = \pi$ was used. Because the dipolar Hamiltonian is bilinear, it is not

effected by this transformation while the Zeeman Hamiltonian picks up a minus sign.

$$\tilde{\mathcal{H}}(t_3) = -\Omega_z I_{z_T} + \mathcal{H}_{zz} \quad (4.42)$$

Continuing in this stepwise manner, the last two toggling frame Hamiltonians for the remaining events in the $\{Y, Y\}$ pulse sequence are

$$\begin{aligned} \tilde{\mathcal{H}}(t_4) = & -\Omega_z (I_{z_T} \cos \theta + I_{x_T} \sin \theta) \\ & - \frac{1}{2} \mathcal{H}_{yy} + \mathcal{H}_y^S \cos(2\theta) + \mathcal{H}_y^A \sin(2\theta) \end{aligned} \quad (4.43)$$

$$\tilde{\mathcal{H}}(t_5) = +\Omega_z I_{z_T} + \mathcal{H}_{zz}. \quad (4.44)$$

Table 4.1 summarizes these results for the $\{Y, Y\}$ sequence.

To calculate the toggling frame Hamiltonians for the similar pulse sequences, $\{\bar{Y}, Y\}$, $\{X, X\}$, and $\{\bar{X}, X\}$ we introduce following terms analogous to those in equations (4.38) - (4.40).

$$\mathcal{H}_{xx} \equiv \sum_{i=1}^N \sum_{j>k}^N B_{ij} \left(3I_{x_i} I_{x_j} - \vec{I}_i \cdot \vec{I}_j \right) \quad (4.45)$$

$$\mathcal{H}_x^A \equiv \frac{3}{2} \sum_{i=1}^N \sum_{j>k}^N B_{ij} (I_{y_i} I_{z_j} + I_{z_i} I_{y_j}) \quad (4.46)$$

$$\mathcal{H}_x^S \equiv \frac{3}{2} \sum_{i=1}^N \sum_{j>k}^N B_{ij} (I_{z_i} I_{z_j} - I_{y_i} I_{y_j}) \quad (4.47)$$

The toggling frame Hamiltonian expressions for all these pulse sequences are shown in Tables 4.1 for comparison. At this point it is important to emphasize again that the toggling frame Hamiltonians between pulses (events \mathcal{U}_1 , \mathcal{U}_3 and \mathcal{U}_5) are identical for all four pulse sequences (Figure 4.1) and that $I_{z_T} \rightarrow -I_{z_T}$ after a π -pulse, regardless

Event	Time	$\tilde{\mathcal{H}}(t_i)$ for $\{Y, Y\}$
\mathcal{U}_1	τ	$+\Omega_z I_{zT} + \mathcal{H}_{zz}$
\mathcal{P}_2	t_p	$+\Omega_z(I_{zT}C_\theta + I_{xT}S_\theta) - \frac{1}{2}\mathcal{H}_{yy} + \mathcal{H}_y^S C_{2\theta} + \mathcal{H}_y^A S_{2\theta}$
\mathcal{U}_3	2τ	$-\Omega_z I_{zT} + \mathcal{H}_{zz}$
\mathcal{P}_4	t_p	$-\Omega_z(I_{zT}C_\theta + I_{xT}S_\theta) - \frac{1}{2}\mathcal{H}_{yy} + \mathcal{H}_y^S C_{2\theta} + \mathcal{H}_y^A S_{2\theta}$
\mathcal{U}_5	τ	$+\Omega_z I_{zT} + \mathcal{H}_{zz}$

Event	Time	$\tilde{\mathcal{H}}(t_i)$ for $\{\bar{Y}, Y\}$
\mathcal{U}_1	τ	$+\Omega_z I_{zT} + \mathcal{H}_{zz}$
\mathcal{P}_2	t_p	$+\Omega_z(I_{zT}C_\theta - I_{xT}S_\theta) - \frac{1}{2}\mathcal{H}_{yy} + \mathcal{H}_y^S C_{2\theta} - \mathcal{H}_y^A S_{2\theta}$
\mathcal{U}_3	2τ	$-\Omega_z I_{zT} + \mathcal{H}_{zz}$
\mathcal{P}_4	t_p	$-\Omega_z(I_{zT}C_\theta + I_{xT}S_\theta) - \frac{1}{2}\mathcal{H}_{yy} + \mathcal{H}_y^S C_{2\theta} + \mathcal{H}_y^A S_{2\theta}$
\mathcal{U}_5	τ	$+\Omega_z I_{zT} + \mathcal{H}_{zz}$

Event	Time	$\tilde{\mathcal{H}}(t_i)$ for $\{X, X\}$
\mathcal{U}_1	τ	$+\Omega_z I_{zT} + \mathcal{H}_{zz}$
\mathcal{P}_2	t_p	$+\Omega_z(I_{zT}C_\theta - I_{yT}S_\theta) - \frac{1}{2}\mathcal{H}_{xx} + \mathcal{H}_x^S C_{2\theta} - \mathcal{H}_x^A S_{2\theta}$
\mathcal{U}_3	2τ	$-\Omega_z I_{zT} + \mathcal{H}_{zz}$
\mathcal{P}_4	t_p	$-\Omega_z(I_{zT}C_\theta - I_{yT}S_\theta) - \frac{1}{2}\mathcal{H}_{xx} + \mathcal{H}_x^S C_{2\theta} - \mathcal{H}_x^A S_{2\theta}$
\mathcal{U}_5	τ	$+\Omega_z I_{zT} + \mathcal{H}_{zz}$

Event	Time	$\tilde{\mathcal{H}}(t_i)$ for $\{\bar{X}, X\}$
\mathcal{U}_1	τ	$+\Omega_z I_{zT} + \mathcal{H}_{zz}$
\mathcal{P}_2	t_p	$+\Omega_z(I_{zT}C_\theta + I_{yT}S_\theta) - \frac{1}{2}\mathcal{H}_{xx} + \mathcal{H}_x^S C_{2\theta} + \mathcal{H}_x^A S_{2\theta}$
\mathcal{U}_3	2τ	$-\Omega_z I_{zT} + \mathcal{H}_{zz}$
\mathcal{P}_4	t_p	$-\Omega_z(I_{zT}C_\theta - I_{yT}S_\theta) - \frac{1}{2}\mathcal{H}_{xx} + \mathcal{H}_x^S C_{2\theta} - \mathcal{H}_x^A S_{2\theta}$
\mathcal{U}_5	τ	$+\Omega_z I_{zT} + \mathcal{H}_{zz}$

Table 4.1: Toggling frame Hamiltonians, $\tilde{\mathcal{H}}(t_i)$, during each event of the four different pulse sequences, $\{\tau-180_{\phi_1}-2\tau-180_{\phi_2}-\tau\}$, where t_p is the pulse time, and τ is the free evolution time and the π -pulse phases are $\{\phi_1, \phi_2\}$. $C_\theta = \cos(\omega_1 t)$, $C_{2\theta} = \cos(2\omega_1 t)$, $S_\theta = \sin(\omega_1 t)$, $S_{2\theta} = \sin(2\omega_1 t)$ where $0 \leq t \leq t_p$.

of phase. The differences between the four pulse sequences appear only in the toggling frame Hamiltonian expressions *during* the pulses. Between the $\{Y, Y\}$ pulse sequence and its alternating phase counterpart, $\{\bar{Y}, Y\}$, there is only a difference in the sign of the sine functions of the event \mathcal{P}_2 . This difference is also found between $\{X, X\}$ and $\{\bar{X}, X\}$. If the delta function pulse approximation is made instead, these differences are excluded from the outset and one expects all sequences to behave identically. However, for strong but finite pulses, these terms effect the final $\bar{\mathcal{H}}$ and will lead to evolution that depends on the phase of the π -pulses that are applied.

4.3.2 Average Hamiltonians for the four pulse sequences

To complete the average Hamiltonian analysis, the expressions from Table 4.1 are fed into Equations (4.11) and (4.12) for the zeroth and first order average Hamiltonian expressions. In the following set of average Hamiltonian expressions, the origin of each term can usually be inferred from the prefactors of τ , t_p , τt_p or t_p^2 . In the zeroth order average Hamiltonian expressions, terms proportional to τ and t_p come from the free evolution event and pulse events, respectively. For the first order Hamiltonian expressions, terms proportional to τt_p and t_p^2 come from the commutator between free evolution and the pulse event, and the commutator of pulse event with itself¹.

¹The direct of calculations of $\bar{\mathcal{H}}_{\{Y,Y\}}^{(1)}$ and $\bar{\mathcal{H}}_{\{X,X\}}^{(1)}$ will not result in the same compact form as those shown in equations (4.49) and (4.53). This requires the replacement $\mathcal{H}_{zz} = -\mathcal{H}_{xx} - \mathcal{H}_{yy}$.

$$\{Y, Y\}: \quad \bar{\mathcal{H}}_{\{Y,Y\}}^{(0)} = \frac{1}{t_c} (4\tau\mathcal{H}_{zz} - t_p\mathcal{H}_{yy}) \quad (4.48)$$

$$\begin{aligned} \bar{\mathcal{H}}_{\{Y,Y\}}^{(1)} &= \frac{-i}{2\pi\hbar} \frac{t_p}{t_c} (t_p [\mathcal{H}_y^A, \mathcal{H}_y^S + \mathcal{H}_{yy}] \\ &\quad + (8\tau + 2t_p) [\Omega_z I_{xT}, \Omega_z I_{zT} + \mathcal{H}_{yy}]) \end{aligned} \quad (4.49)$$

$$\{\bar{Y}, Y\}: \quad \bar{\mathcal{H}}_{\{\bar{Y},Y\}}^{(0)} = \frac{1}{t_c} \left(4\tau\mathcal{H}_{zz} - t_p\mathcal{H}_{yy} - \frac{4\Omega_z}{\pi} t_p I_{xT} \right) \quad (4.50)$$

$$\bar{\mathcal{H}}_{\{\bar{Y},Y\}}^{(1)} = 0 \quad (4.51)$$

$$\{X, X\}: \quad \bar{\mathcal{H}}_{\{X,X\}}^{(0)} = \frac{1}{t_c} (4\tau\mathcal{H}_{zz} - t_p\mathcal{H}_{xx}) \quad (4.52)$$

$$\begin{aligned} \bar{\mathcal{H}}_{\{X,X\}}^{(1)} &= \frac{i}{2\pi\hbar} \frac{t_p}{t_c} (t_p [\mathcal{H}_x^A, \mathcal{H}_x^S + \mathcal{H}_{xx}] \\ &\quad + (8\tau + 2t_p) [\Omega_z I_{yT}, \Omega_z I_{zT} + \mathcal{H}_{xx}]) \end{aligned} \quad (4.53)$$

$$\{\bar{X}, X\}: \quad \bar{\mathcal{H}}_{\{\bar{X},X\}}^{(0)} = \frac{1}{t_c} \left(4\tau\mathcal{H}_{zz} - t_p\mathcal{H}_{xx} + \frac{4\Omega_z}{\pi} t_p I_{yT} \right) \quad (4.54)$$

$$\bar{\mathcal{H}}_{\{\bar{X},X\}}^{(1)} = 0 \quad (4.55)$$

Here we see more explicitly that under the instantaneous pulse approximation (i.e. taking $t_p \rightarrow 0$) there is only evolution under the dipolar Hamiltonian, \mathcal{H}_{zz} ($\frac{4\tau}{t_c} \rightarrow 1$ as $t_p \rightarrow 0$), over the course of the cycle. It is also apparent that the evolution is identical for the different sequences. Taking this limit also shows that first and higher order corrections to $\bar{\mathcal{H}}^{(0)}$ are only present when the instantaneous pulse approximation is not assumed. This suggests that the behavioral differences between the four pulse sequences (Figure 3.5) may arise solely from the presence of both the dipolar and Zeeman Hamiltonian under the action of strong but finite pulses. Admittedly, these terms are quite small for strong pulses, and have little effect over a single cycle.

However, these small terms can have large impact as the cycle is repeated many times, resulting in different dynamics of the system that are unique to the pulse sequences used. Under close inspection of Figure 3.5 and Figure 3.9 after only a few cycles, at early times, the pulse sequences have very similar evolution. It is only after a more repetitions of the cycle that the divergent evolution is more apparent.

4.3.3 Simulations Using Average Hamiltonian Expressions

Although the average Hamiltonian terms in equations (4.48)-(4.55) have their differences, the complicated expressions can be hard to interpret. Since the interpretation was not immediately obvious, simulations were used to help study their effects.

For simplicity, we look only at the $\{Y, Y\}$ pulse sequence and see how the terms in $\bar{\mathcal{H}}^{(0)}$ and $\bar{\mathcal{H}}^{(1)}$ can contribute to the long tail behavior we first observed in experiments. Figure 4.2 shows average Hamiltonian simulations and exact calculations for the $\{Y, Y\}$ pulse sequence with parameters $\frac{\omega_1}{2\pi} = 40$ kHz, and $\tau = 1$ μ s. In order to compare average Hamiltonian simulations to exact calculations like those done in Section 3.6.2, the dipolar coupling strength is increased by a factor of 25. As another simplification, we use $\Omega_z = 0$ based on the adamantane experiments in Section 3.6.1 which indicated that a spread in Ω_z was not a requirement to see these effects.

As a first comparison, Figure 4.2 (a) shows the the fastest dipolar decay when \mathcal{H}_{int} is forced to zero during the pulses. If $\mathcal{H}_{int} \neq 0$ during the pulses, and the average Hamiltonian description is taken to first order, $\bar{\mathcal{H}}_{\{Y, Y\}}^{(0)}$, the decay slows and the long tail begins to emerge (Figure 4.2 (b)). Including both $\bar{\mathcal{H}}_{\{Y, Y\}}^{(0)}$ and $\bar{\mathcal{H}}_{\{Y, Y\}}^{(1)}$ in the simulations shows a further increase in the tail height (Figure 4.2 (b)). This simulation compares very well with the exact calculations (Figure 4.2 (c)), strongly suggesting that higher order average Hamiltonian terms like $\bar{\mathcal{H}}_{\{Y, Y\}}^{(2)}$ or greater are not

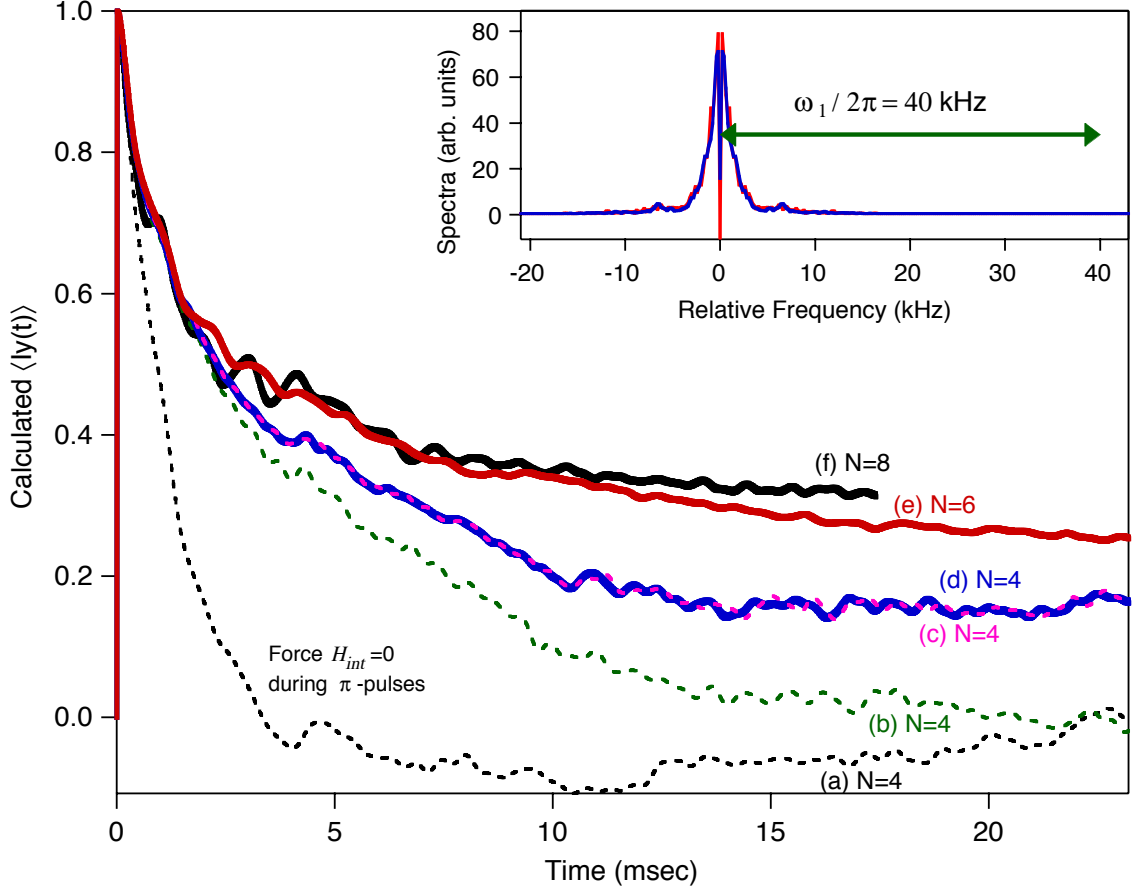


Figure 4.2: CPMG calculations for pure dipolar decay ($\Omega_z = 0$, $\frac{\omega_1}{2\pi} = 40$ kHz, and $\tau = 1 \mu\text{s}$). Each curve averages 400 DRs [exception (f): 80 DRs] of N spins on a silicon lattice, with $\gamma' = 5\gamma$ of ^{29}Si . Several approximations are used for $N = 4$: (a) setting $\mathcal{H}_{int} = 0$ during pulses, (b) using $\bar{\mathcal{H}}_{\{Y,Y\}}^{(0)}$ only, and (c) using $\bar{\mathcal{H}}_{\{Y,Y\}}^{(0)} + \bar{\mathcal{H}}_{\{Y,Y\}}^{(1)}$ only. Exact calculations for (d) $N = 4$, (e) $N = 6$, and (f) $N = 8$ show that the tail height depends on N . Inset shows the pulses strength used compared to the calculated spectra for $N = 4$ (red) and $N = 6$ (blue). From reference [3].

required to describe the behavior, at least for these particular parameters.

It is interesting to note that average Hamiltonian theory was first introduced as a tool for designing line narrowing sequences with $\bar{\mathcal{H}}^{(0)} = 0$, which should result in a lack of signal decay. Higher order corrections that were non-zero were then to blame for any observable decay [13, 25, 26]. In contrast, for the $\{Y, Y\}$ sequence, higher order corrections to $\bar{\mathcal{H}}_{\{Y, Y\}}^{(0)}$ somehow preserve coherence, and instead slow the decay expected for $\bar{\mathcal{H}}_{\{Y, Y\}}^{(0)}$.

Although the average Hamiltonian descriptions in equations (4.48)-(4.55) offer a model to work with that agrees with exact calculations, it is still difficult to interpret the long list of terms in the $\bar{\mathcal{H}}_{\{Y, Y\}}^{(1)}$ and $\bar{\mathcal{H}}_{\{X, X\}}^{(1)}$ expressions. From the simulations in Figure 4.2, it is clear that the complicated terms in $\bar{\mathcal{H}}^{(1)}$ are important in these multiple π -pulse experiments, but it is not clear how these expressions lead to divergent evolution in the different pulse sequences [4].

Unable to make significant progress interpreting the complicated terms for these simple pulse sequences, we wondered if we could combine the $\{\phi_1, \phi_2\}$ blocks in ways that that would result in simpler average Hamiltonian expressions. These explorations, guided and inspired by classic NMR experiments, resulted in a new way of controlling spin coherence and are outlined in the next chapters.

Chapter 5

Exploring the AHT Model:

Coherence Control using $\bar{\mathcal{H}}^{(0)}$

In this chapter, we begin to explore the average Hamiltonian model outlined in Chapter 4. Although the repeating π -pulses in the CP, APCP, CPMG and APCPMG experiments follow a very simple repeating pattern, the zeroth and first order average Hamiltonian expressions in equations (4.48)-(4.55) are quite complicated. These expressions are hard to interpret and can make the quantitative predictions of their effects difficult [3, 4, 5]. In order to explore and test the average Hamiltonian model outlined in the previous chapter, more complicated pulse sequences based on this description were designed with the intent of manipulating the system into following much simpler approximate Hamiltonian expressions. Although firmly rooted in the regime where $\mathcal{H}_{P_\phi} \gg \mathcal{H}_{int}$, these experiments are designed to utilize terms that are not present in the delta function pulse approximation. Therefore, the experiments that follow would not work in the delta function pulse limit.

These NMR experiments were conducted on a powder sample of C₆₀ in a 12 Tesla field at room temperature. The ¹³C spin- $\frac{1}{2}$ nucleus has a 1.11% natural abundance

(n.a.) and has a Larmor Frequency of 128.56 MHz in this field. At room temperature, buckyballs form an fcc lattice where each molecule undergoes rapid isotropic rotation about its lattice point [46, 47, 48]. Due to this rapid molecular motion, the intra-C₆₀ dipolar couplings are averaged to zero while the inter-ball dipolar coupling between different C₆₀ molecules is left intact. For this reason the spin system is well approximated by a single species of spin- $\frac{1}{2}$ nuclei located on average at the center of each molecule, coupled together by the like-spin dipolar interaction [3, 24]. The macroscopic powder sample can be viewed as an ensemble of N-spin clusters, with different magnetic shift Ω_z values in different clusters due to bulk diamagnetism.

For this system, the Hamiltonian in the rotating frame is $\mathcal{H}_{int} = \mathcal{H}_Z + \mathcal{H}_{zz}$, where the Zeeman term which allows for a net resonance offset (Ω_P) is $\mathcal{H}_Z = (\Omega_z^{loc} + \Omega_P)I_{zT}$, and the secular part of the homonuclear dipolar coupling is $\mathcal{H}_{zz} = \sum_{j>i}^N B_{ij} \left(3I_{z_i}I_{z_j} - \vec{I} \cdot \vec{I} \right)$. In this material the resulting Zeeman line broadening dominates the spectrum's full width half maximum (FWHM). The spectrum's measured FWHM = 260Hz, while the calculated dipolar FWHM = 38Hz. For these experiments the rf pulses were unusually hard, with a pulse strength $\frac{\omega_1}{2\pi} = 25\text{kHz}$ which is 100 times the ¹³C line width. To make the rf field intensity uniform across the sample, the sample was restricted to < 8% of the coil volume.

5.1 FID of the Echo Train

As discussed in the previous chapter, average Hamiltonian theory allows us some insight into the pulse phase dependence of these multiple pulse sequences. The CPMG experiment, $90_X - \{Y, Y\}^N$, produced a long lived train of spin echoes, while the APCPMG experiment, $90_X - \{\bar{Y}, Y\}^N$, exhibited a rapidly decaying tail. The top panel of Figure 5.1 shows NMR data for these sequences applied to ¹³C nuclei in C₆₀.

As we saw in Chapter 4, the zeroth order average Hamiltonian expressions for the repeating part of these multiple pulse sequences are

$$\bar{\mathcal{H}}_{\{Y,Y\}}^{(0)} = \alpha\mathcal{H}_{zz} - \beta\mathcal{H}_{yy} \quad (5.1)$$

$$\bar{\mathcal{H}}_{\{\bar{Y},Y\}}^{(0)} = \alpha\mathcal{H}_{zz} - \beta\mathcal{H}_{yy} - \lambda\Omega_z I_{x_T}. \quad (5.2)$$

where the following dimensionless quantities have been introduced

$$\alpha = \frac{4\tau}{t_c} \quad (5.3)$$

$$\beta = \frac{t_p}{t_c} \quad (5.4)$$

$$\lambda = \frac{4t_p}{\pi t_c}. \quad (5.5)$$

The $\{\bar{Y}, Y\}$ sequence has an extra term in equation (5.2) compared to $\{Y, Y\}$ in equation (5.1). This term, proportional to I_{x_T} , can be interpreted as an average constant magnetic field along \hat{x} . If this were the only term in the Hamiltonian, it would cause spins to nutate in the y - z plane. In this picture, the variation in Zeeman energies Ω_z across the sample causes a spread of the spins as they nutate, leading to the eventual decay of the coherent signal.

During a free induction decay in the same system, spins initially along \hat{y} freely evolve under the Hamiltonian

$$\mathcal{H} = \Omega_z I_{z_T} + \mathcal{H}_{zz}. \quad (5.6)$$

The free induction decay, characterized by T_2^* , is a result of the spread in Zeeman energies Ω_z . In comparison, the decay produced in the APCPMG sequence $90_X - \{\bar{Y}, Y\}^N$ in Figure 5.1 can be thought of as an FID of the echo train. For the

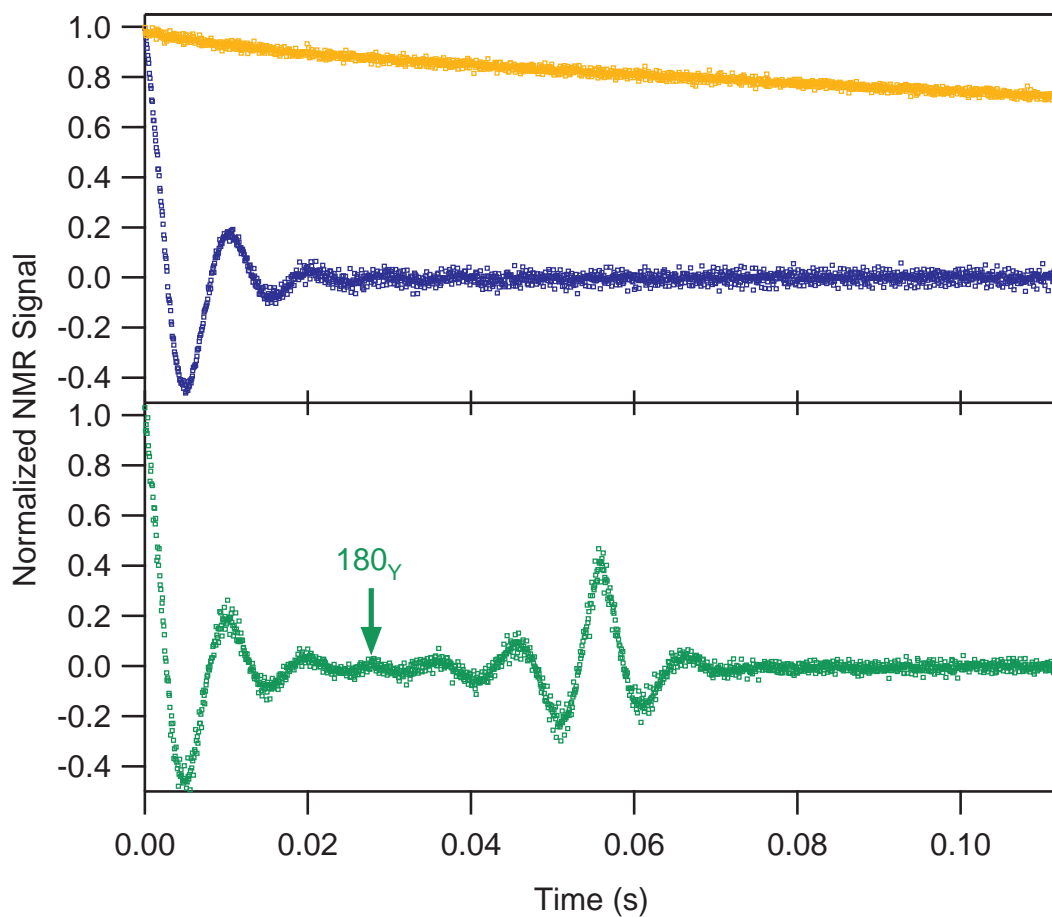


Figure 5.1: NMR data for ^{13}C nuclei in C_{60} at room temperature. Comparison of the CPMG pulse sequence $90_X - \{Y, Y\}^N$ (yellow) to the APCPMG sequence, $90_X - \{\bar{Y}, Y\}^N$ (blue). Inserting a single flip- 180_Y pulse into $\{\bar{Y}, Y\}^N$ induces an echo of the echo train (green). $\tau = 25\mu\text{s}$, $\alpha \approx 0.71$. Only the peak of each echo is shown. Signal is normalized to the amplitude of the C_{60} FID.

APCPMG experiment, the effective field $\lambda\Omega_z I_{x_T}$ along $\hat{\mathbf{x}}$ plays the role of the large external field $\vec{\mathbf{B}}_0$ parallel to $\hat{\mathbf{z}}$ in the classic FID experiment. The motion of the spins in the the y - z plane in the APCPMG experiment is analogous to the motion in the x - y plane in a normal FID experiment.

5.2 Hahn Echo Analog

Continuing this analogy, it can be asked whether the dephasing caused by the Zeeman-like term $\lambda\Omega_z I_{x_T}$ can be reversed as the effect of $\Omega_z I_{z_T}$ is reversed in a Hahn echo experiment. As described in Section 3.4.1, the decay in an FID can be partially refocused by the application of a single π -pulse. The π -pulse reverses the dephasing caused by the spread in Zeeman energies, resulting in a Hahn spin echo.

In the same vein, we can attempt to refocus the signal lost due to the I_x term in equation (5.2) by applying π -pulses. Inserting a single 180_Y pulse into the APCPMG sequence $90_X - \{\bar{Y}, Y\}^{N_1} - 180_Y - \{\bar{Y}, Y\}^{N_2}$ does, in fact, produce an echo in the envelope of the individual spin echo peaks (Figure 5.1). Although in appearance the shape of the echo is reminiscent of a conventional spin echo, the signal actually extends over more than 800 individual spin echo peaks. The spin echo in the bottom panel of Figure 5.1 is an echo of the echo train itself.

To understand the echo of the echo train in Figure 5.1, we can write $\bar{\mathcal{H}}_{\{\bar{Y}, Y\}}^{(0)}$ in equation (4.50) in terms of the similar expression for $\bar{\mathcal{H}}_{\{Y, Y\}}^{(0)}$ in (4.48),

$$\bar{\mathcal{H}}_{\{\bar{Y}, Y\}}^{(0)} = \bar{\mathcal{H}}_{\{Y, Y\}}^{(0)} - \lambda\Omega_z I_{x_T}. \quad (5.7)$$

If the single inserted 180_Y pulse is treated as a perfect rotation, \mathcal{R}_{π_Y} , we can write

the density matrix as

$$\rho(t) = \mathcal{U}_{\{\bar{Y}, Y\}} \mathcal{R}_{\pi_Y} \mathcal{U}_{\{\bar{Y}, Y\}} \rho(0) \{inv\} \quad (5.8)$$

$$= \mathcal{U}_{\{\bar{Y}, Y\}} \mathcal{R}_{\pi_Y} \mathcal{U}_{\{\bar{Y}, Y\}} (\mathcal{R}_{\pi_Y}^{-1} \mathcal{R}_{\pi_Y}) \rho(0) \{inv\} \quad (5.9)$$

$$= \mathcal{U}_{\{\bar{Y}, Y\}} \left(\mathcal{R}_{\pi_Y} \mathcal{U}_{\{\bar{Y}, Y\}} \mathcal{R}_{\pi_Y}^{-1} \right) \mathcal{R}_{\pi_Y} \rho(0) \{inv\} \quad (5.10)$$

where the operators $\mathcal{U}_{\{\bar{Y}, Y\}}$ and \mathcal{R}_{π_Y} can be explicitly written as

$$\mathcal{U}_{\{\bar{Y}, Y\}} = e^{-\frac{i}{\hbar} (\bar{\mathcal{H}}_{\{Y, Y\}}^{(0)} - \lambda \Omega_z I_{x_T}) N_2 t_c} \quad (5.11)$$

$$\mathcal{R}_{\pi_Y} = e^{i\pi I_{y_T}}. \quad (5.12)$$

The term $(\mathcal{R}_{\pi_Y} \mathcal{U}_{\{\bar{Y}, Y\}} \mathcal{R}_{\pi_Y}^{-1})$ is a transformation of $\mathcal{U}_{\{\bar{Y}, Y\}}$ by a π_y rotation. Because the terms in $\bar{\mathcal{H}}_{\{Y, Y\}}^{(0)}$ are bilinear, they are not effected by a π -rotation while the Zeeman term changes sign; $-\lambda \Omega_z I_{x_T} \rightarrow +\lambda \Omega_z I_{x_T}$. Then the density matrix becomes

$$\rho(t) = e^{-\frac{i}{\hbar} (\bar{\mathcal{H}}_{\{Y, Y\}}^{(0)} - \lambda \Omega_z I_{x_T}) N_2 t_c} e^{-\frac{i}{\hbar} (\bar{\mathcal{H}}_{\{Y, Y\}}^{(0)} + \lambda \Omega_z I_{x_T}) N_1 t_c} \mathcal{R}_{\pi_Y} \rho(0) \{inv\} \quad (5.13)$$

$$= e^{-\frac{i}{\hbar} (\bar{\mathcal{H}}_{\{Y, Y\}}^{(0)} - \lambda \Omega_z I_{x_T}) N_2 t_c} e^{-\frac{i}{\hbar} (\bar{\mathcal{H}}_{\{Y, Y\}}^{(0)} + \lambda \Omega_z I_{x_T}) N_1 t_c} \rho(0) \{inv\} \quad (5.14)$$

where in the last step we have used the fact that $\rho(0) = I_{y_T}$. Like the Hahn echo experiment in Section 3.4.1, π -pulses can be applied to refocus the signal loss due to the term $\lambda \Omega_z I_{x_T}$. Rephasing after the 180_Y pulse leads to the echo of the echo train when $N_1 = N_2$.

If this average Hamiltonian model is a faithful description of the behavior and the pulse quality is very good, then a 180_X pulse along \hat{x} should have no effect on the term $-\lambda \Omega_z I_{x_T}$, and therefore have no effect on the on the APCPMG sequence. As the theory predicts, there is no echo of the echo train when a single flip- 180_X is applied during $\{\bar{Y}, Y\}$ repeating blocks (Figure 5.2, red). The the origi-

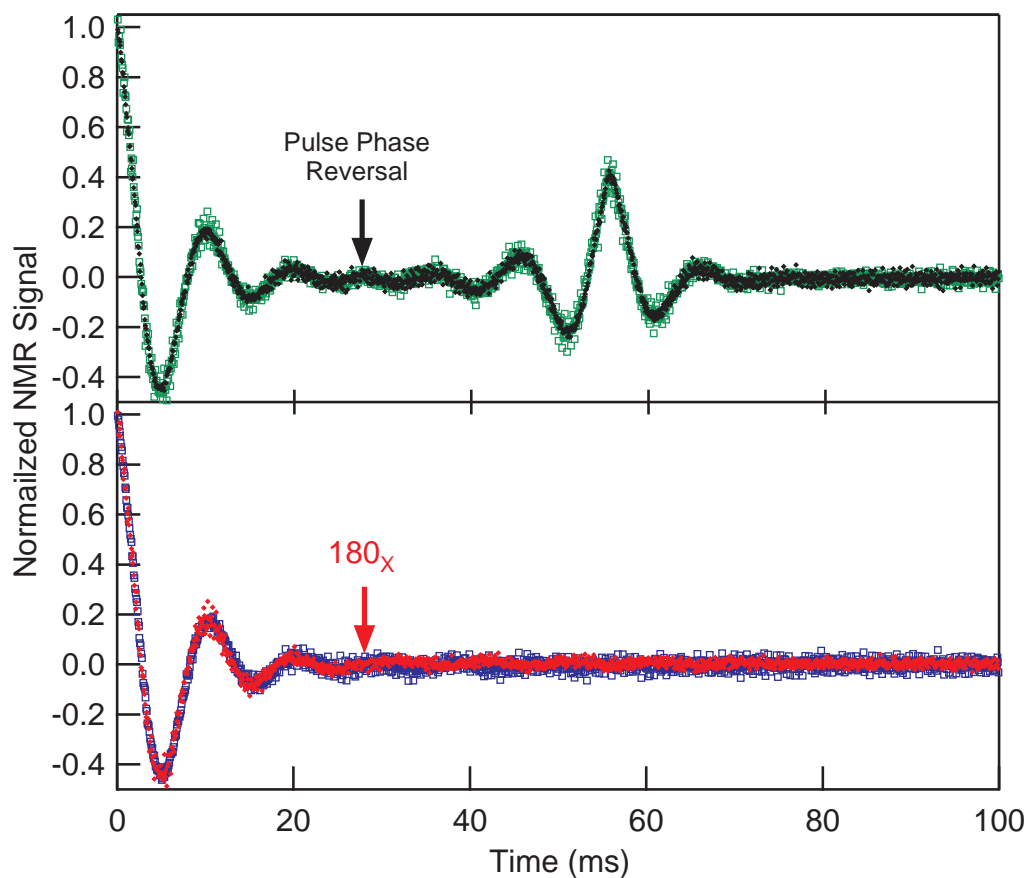


Figure 5.2: NMR data for ^{13}C nuclei in C_{60} at room temperature. Reversing the APCPMG phase pattern, $90_X - \{\bar{Y}, Y\}^{200} - \{Y, \bar{Y}\}^{600}$, at the point indicated (black) has the same effect as inserting a single y -phase π -pulse, $90_X - \{\bar{Y}, Y\}^{200} - 180_Y - \{\bar{Y}, Y\}^{600}$ (green). Inserting a single x -phase π -pulse, $90_X - \{\bar{Y}, Y\}^{200} - 180_X - \{\bar{Y}, Y\}^{600}$, has no effect (red) and looks like the original APCPMG experiment, $90_X - \{\bar{Y}, Y\}^{800}$ (blue). $\tau = 25\mu\text{s}$ and $\alpha \approx 0.71$. Only the peak of each echo is shown. The signals are normalized to the amplitude of the C_{60} .

nal APCPMG experiment (Figure 5.2, blue) is indistinguishable from the experiment $90_X - \{\bar{Y}, Y\}^{N_1} - 180_X - \{\bar{Y}, Y\}^{N_2}$ since there is no change in the sign of $-\lambda\Omega_z I_{x_T}$.

As another test of the model, we can use the pulse sequence $\{Y, \bar{Y}\}$ which inverts the pulse phases of the original $\{\bar{Y}, Y\}$ APCPMG experiment. The two sequences, $\{\bar{Y}, Y\}$ and $\{Y, \bar{Y}\}$, have only a sign difference in the effective field of their zeroth order average Hamiltonian expression,

$$\bar{\mathcal{H}}_{\{\bar{Y}, Y\}}^{(0)} = \bar{\mathcal{H}}_{\{Y, \bar{Y}\}}^{(0)} - \lambda\Omega_z I_{x_T} \quad (5.15)$$

$$\bar{\mathcal{H}}_{\{Y, \bar{Y}\}}^{(0)} = \bar{\mathcal{H}}_{\{\bar{Y}, Y\}}^{(0)} + \lambda\Omega_z I_{x_T}. \quad (5.16)$$

Instead of applying a single 180_Y pulse during the APCPMG experiment, the same effect can be achieved by switching the phase of the pulses in the second time interval.

If N $\{\bar{Y}, Y\}$ blocks are followed by an equal number N of $\{Y, \bar{Y}\}$ blocks, an echo of the echo train will emerge. For the experiment $90_X - \{\bar{Y}, Y\}^{N_1} - \{Y, \bar{Y}\}^{N_2}$, the density matrix has nearly the same form as equation (5.14).

$$\rho(t) = \mathcal{U}_{\{Y, \bar{Y}\}} \mathcal{U}_{\{\bar{Y}, Y\}} \rho(0) \{inv\} \quad (5.17)$$

$$= e^{-\frac{i}{\hbar} (\bar{\mathcal{H}}_{\{Y, \bar{Y}\}}^{(0)} + \lambda\Omega_z I_{x_T}) N_2 t_c} e^{-\frac{i}{\hbar} (\bar{\mathcal{H}}_{\{\bar{Y}, Y\}}^{(0)} - \lambda\Omega_z I_{x_T}) N_1 t_c} \rho(0) \{inv\}. \quad (5.18)$$

In both cases, changing the sign of the dephasing term produces a time reversal of the Zeeman evolution from one period to the next, resulting in an echo of the echo train (Figure 5.2 black and green). Between the two experiments, the result is nearly identical whether one pulse is added or if the phase of 1200 pulses is changed.

This phase reversal experiment, $90_X - \{\bar{Y}, Y\}^{N_1} - \{Y, \bar{Y}\}^{N_2}$, which switches the sign of the dephasing term $\Omega_z I_{x_T}$ can be thought of in analogy to Solomon's original rotary echo experiment [49]. In Solomon's experiment, a constant transverse rf field is applied to the spins which cause them to nutate in a plane perpendicular to the

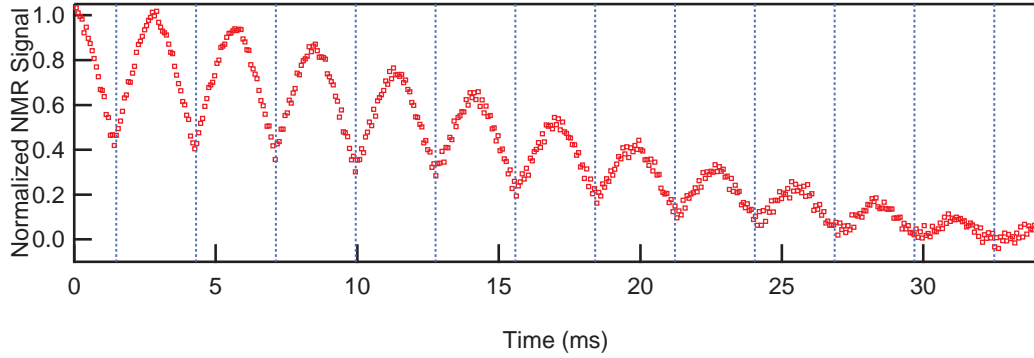


Figure 5.3: A CPMG of the echo train is induced by using the sequence $90_X - \{\bar{Y}, Y\}^{10} - \left\{ \{Y, \bar{Y}\}^{20} - \{\bar{Y}, Y\}^{20} \right\}^{12}$. Only the peak of each echo in the echo train is shown. Sample C₆₀. $\tau = 25\mu s$ and $\alpha \approx 0.71$.

transverse field. If the transverse field is inhomogeneous, the nuclear spins will experience different local rf fields. In an inhomogeneous field spins will nutate at different rates, causing the spins to dephase and the signal to decay. If the transverse field is then reversed and applied for an equal amount of time, the spins will rephase and a rotary echo will appear. In the classic NMR experiment, the dephasing caused by nutation under a spread in ω_1 values is undone by subsequent nutation under $-\omega_1$. In contrast to the rotary echo experiment, a spread in Ω_z rather than a spread in ω_1 is responsible for the signal loss shown in Figure 5.1, and subsequent motion under $-\Omega_z$ causes a spin echo in the echo train.

Continuing in this manner, more π -pulses can be applied during the $\{\bar{Y}, Y\}$ sequence to reverse the effects of the Zeeman-like dephasing. To produce the same effect one can alternate between blocks of $\{\bar{Y}, Y\}$ and $\{Y, \bar{Y}\}$, creating multiple echoes in the envelope of the individual spin echo peaks, a CPMG of the echo train. Figure 5.3 shows the phase-change version of the experiment, which is easier to implement and less likely to suffer from finite pulse effects.¹ However, the dipolar part of $\bar{\mathcal{H}}_{\{\bar{Y}, Y\}}^{(0)}$ in

¹The finite pulse effects described in Chapter 4 become important if many π -pulses are inserted into the original $90_X - \{\bar{Y}, Y\}^N$ experiment. This seemingly inconsistent treatment of strong pulses is discussed in the final paragraph of this section.

equation (5.2) is just $\bar{\mathcal{H}}_{\{Y,Y\}}^{(0)}$ in equation (5.1). In all of the previous experiments, the sign of $\bar{\mathcal{H}}_{\{Y,Y\}}^{(0)}$ is never reversed. This contributes to the observed decay of the echoes of the echo train in all the cases discussed so far.

Before moving on to the next set of experiments, the validity of representing the inserted 180_ϕ and, implicitly, the initializing 90_X pulses as pure rotations must be addressed. The treatment of these pulses as delta function pulses may seem inconsistent with the analysis in Section 4.3, which is the foundation of these and following experiments. This analysis used the terms that emerge from the finite pulse duration to explain behavior that did not adhere to the conventional theory for strong pulses. It is true that these new experiments exploit the effects of the repeating block that come from the non-zero duration of the π -pulses. While the surprisingly non-negligible effects of the dipolar coupling during the strong but finite π -pulses adds non-zero quantum coherence operators to $\bar{\mathcal{H}}^{(0)} + \bar{\mathcal{H}}^{(1)}$, these contributions are small and only manifest large effects after the coherent repetition of many $\{\phi_1, \phi_2\}$ blocks. For this reason, treating the few 90_ϕ and 180_ϕ pulses outside of the repeating block as delta function rotations is not an unreasonable approximation.

5.3 Quadrature Detection in the Echo of Echoes

The firsts two experiments in Section 5.2, $90_X - \{\bar{Y}, Y\}^{N_1} - 180_X - \{\bar{Y}, Y\}^{N_2}$ and $90_X - \{\bar{Y}, Y\}^{N_1} - \{Y, \bar{Y}\}^{N_2}$, seemed to produce identical results, as shown in Figure 5.2. However, the physical interpretation is slightly different, as are the time evolution operators, equations (5.14) and (5.18), respectively.

In Section 5.2 these experiments were compared to the classic NMR Hahn echo and Solomon's rotary echo, whose physically different spin evolutions can be described by what Abragam termed as pancake and racetrack echoes, in his canonical text *The*

Principles of Nuclear Magnetism [9].

The two types of echoes are shown in Figure 5.4, looking from above at the x - y plane. After an initializing 90_X pulse, the spins lie in the transverse plane along the y -axis. As they spread due to small variations in the local magnetic field, some going clockwise (red) and others going counterclockwise (blue) in the rotating frame, a spin “pancake” is formed in the transverse plane. If the pancake is flipped by a 180_Y pulse, the phase angle of each spin isochromat changes sign as measured from the y -axis. In this case there is no change in the local fields and the spins continue in the same rotational direction from their new phase position in the x - y plane. If the π -pulse is applied at time τ , the spins will rephase and form an spin echo at time 2τ .

In the racetrack echo, the isochromats are compared to runners on a track [9]. As time passes, the runners spread out uniformly around the track. If at time τ , the runners change direction and run at the same speed, they will form an “echo” at time 2τ . In the rotating frame of the spin isochromats, the spins dephase according to the spread in $+\Omega_z$ just as they do for the pancake echo (Figure 5.4B). However, in the racetrack echo no π -pulse is applied. Instead, the sign of the dephasing field ($+\Omega_z$) is reversed ($-\Omega_z$) for the second time interval. This causes the spins to change direction and precess with the opposite sense of rotation. Specifically, the clockwise going spins change direction at time τ moving counterclockwise while counterclockwise going spins move clockwise.

In the Hahn echo analog experiments in Section 5.2, quadrature detection along the x -axis shows that there is no signal along \hat{x} , although there is an oscillating signal along \hat{y} (Figure 5.5). In the two types of Hahn echo analog experiments, the spins are nutating in the y - z plane due to a small average field along \hat{x} ¹ caused by phase transients. In the π -pulse version of the Hahn echo analog experiment, the

¹This small field is generated by the pattern of phase transients that appear at the beginning and end of the 180_Y and $180_{\bar{Y}}$ pulses. See Appendix A.

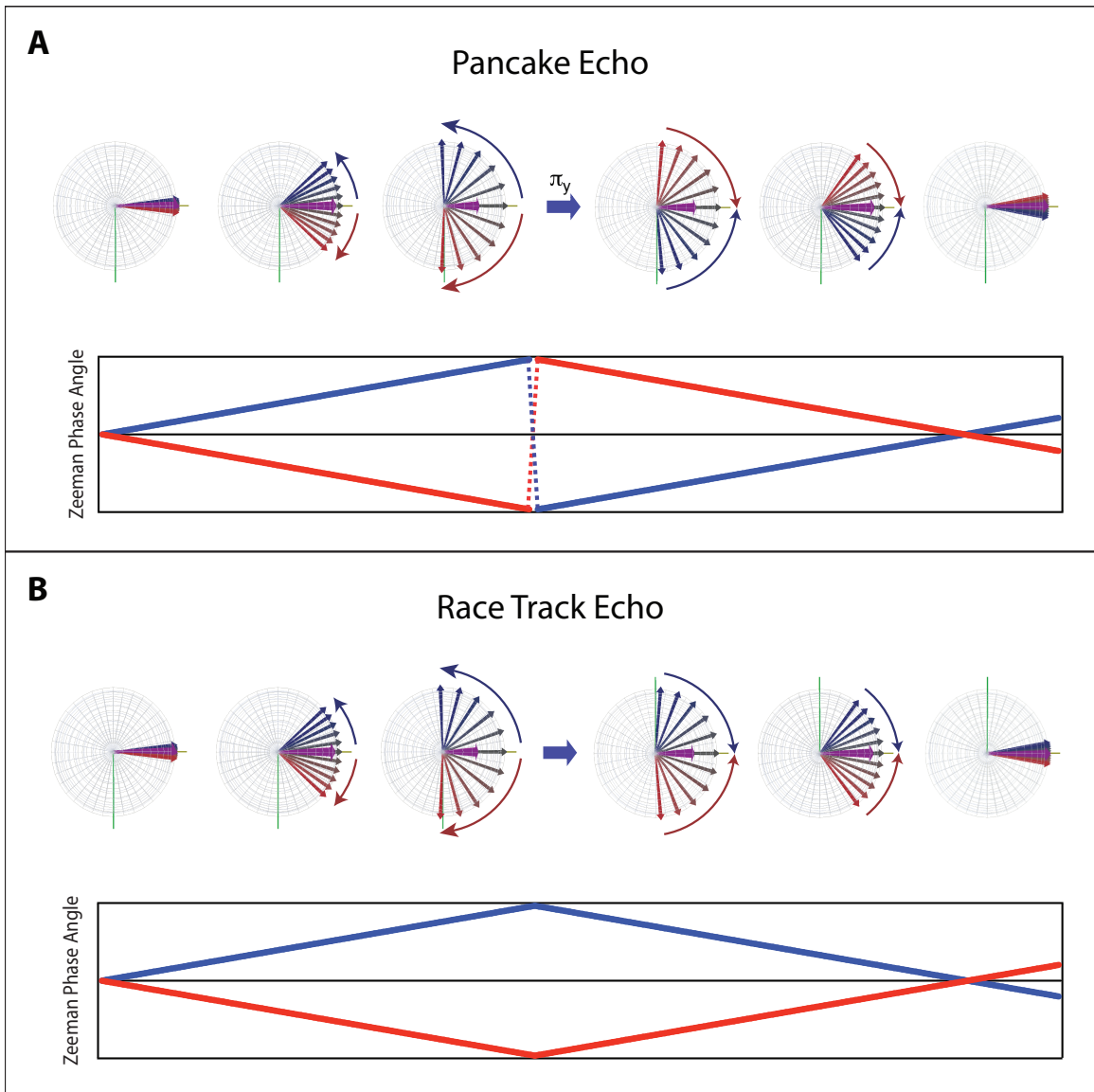


Figure 5.4: Comparison of the pancake and racetrack echoes in the Bloch sphere and below in Zeeman phase angle. **A.** In a pancake echo, the phase of individual spin isochromats is changed by a factor of (-1) by the application of a π -pulse causing a discontinuous jump in the Zeeman phase angle. After the π pulse, spins continue to rotate in the same direction under the influence of the local magnetic field: spins moving clockwise (counterclockwise) in red (blue) continue in the same sense of rotation before and after the π -pulse. **B.** In a racetrack echo, the sign of the local magnetic field is changed from the first time interval to the second. In the second time interval, the spins rotate in the opposite sense from the initial rotation and the Zeeman phase acquired in the first time interval is undone without a discontinuous jump.

repeating pulse block $\{\bar{Y}, Y\}$ never changes, therefore the pattern of phase transients never changes. In the phase reversal version of the Hahn echo analog experiment, the repeating pulse block $\{\bar{Y}, Y\}$ changes to $\{Y, \bar{Y}\}$, which causes the phase transients to also change sign. The π -pulse version of the experiment should exhibit the characteristics of Abragam's pancake echo, while the later should show the characteristics of the racetrack echo. Between the two types of experiments, the field along \hat{x} generated by the phase transients in the second time interval ($t \geq N_1 t_c$) is opposite in sign. Therefore, they should nutate in opposite directions in the y - z plane.

However, as Figure 5.5 shows, the measured $\langle I_y(t) \rangle$ looks identical for both the pancake and racetrack echo. To distinguish between the two types of Hahn echo analog experiments, $90_X - \{\bar{Y}, Y\}^{N_1} - 180_X - \{\bar{Y}, Y\}^{N_2}$ and $90_X - \{\bar{Y}, Y\}^{N_1} - \{Y, \bar{Y}\}^{N_2}$, quadrature detection is necessary along the z -axis to measure $\langle I_z(t) \rangle$. To accomplish this, snapshots along the z -axis are taken by applying a 90_X pulse at varying points of the Hahn echo analog experiment and measuring the initial height of the FID that results. The 90_X pulse projects the value of the magnetization along \hat{z} into the y -axis for measurement. By taking $N_1 = 60$ and $N_2 = 5, 10, 15, \dots, 100$ before the last 90_X , magnetization along \hat{z} can be tracked.

Figure 5.5 clearly demonstrates that the π pulse version of the experiment (black) causes an opposite sense of rotation compared to the phase reversal version of the experiment (blue).

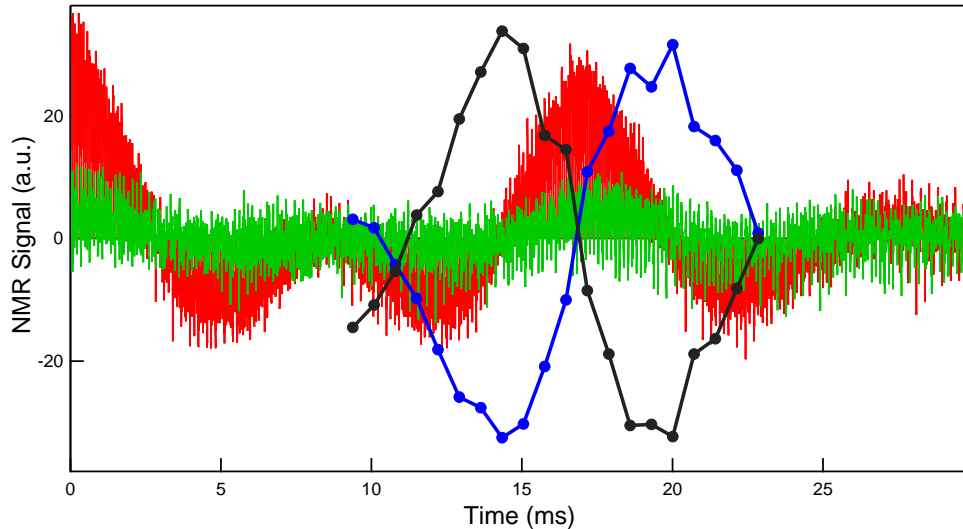


Figure 5.5: Quadrature detection in the Hahn echo analog. The original Hahn echo analog experiment is shown in red (observation along the y -axis) and green (observation along the x -axis). $90_X - \{\bar{Y}, Y\}^{N_1} - 180_X - \{\bar{Y}, Y\}^{N_2} - 90_X$ in black and $90_X - \{\bar{Y}, Y\}^{N_1} - \{Y, \bar{Y}\}^{N_2} - 90_X$ in blue. Data points generated by taking $N_2 = 5, 10, 15, \dots, 100$ and measuring the initial height of the FID generated by the last 90_X pulse. $N_1 = 60$, $t_p = 20.9 \mu\text{s}$, $\tau = 25 \mu\text{s}$.

5.4 Magic Echo Analog

5.4.1 Manipulating the Dipolar Term

As we saw in Sections 3.4.1 and 5.2, it is convenient to view spin echo phenomenon by picturing the spins as first developing under the influence of some Hamiltonian, then in the second time interval as developing under the negative of that Hamiltonian. In this way, the spin system can return to its original state, resulting in a spin echo.

In the same manner, if the sign of the dipolar coupling term in the Hamiltonian can be reversed after the initial dephasing has occurred, then the magnetization lost to dipolar coupling can be recovered. The Lee-Goldburg experiment [50, 51] was able to manipulate the dipolar coupling term by applying a long continuous pulse field in the transverse direction. In this case the truncated Hamiltonian in the rotating frame

is

$$\mathcal{H} = \gamma \hbar B_{\text{eff}} I_{\xi} + \frac{1}{2} (3 \cos^2 \theta - 1) \sum_{i>j}^N B_{ij} (3 I_{\xi_i} I_{\xi_j} - \vec{I}_i \cdot \vec{I}_j) \quad (5.19)$$

where the system is now quantized along the effective field $\vec{B}_{\text{eff}} = (B_1, 0, \delta B_z)$ and θ is the angle between the static field \vec{B}_0 and $\vec{B}_{\text{eff}} = B_{\text{eff}} I_{\xi} \hat{\xi}$. By a suitable choice of \vec{B}_{eff} , and therefore θ , Lee and Goldberg found that they could effectively eliminate the dipolar term by setting

$$\frac{3 \cos^2 \theta - 1}{2} \rightarrow 0 \quad (5.20)$$

In the case of the magic echo experiment [42, 43, 52], $\theta = \frac{\pi}{2}$ and B_1 is exactly on resonance¹. The angular factor now has a negative sign

$$\frac{3 \cos^2 \theta - 1}{2} = -\frac{1}{2} \quad (5.21)$$

which can be used to reverse dipolar dephasing. Under a strong, constant pulse field along \hat{x} , the dipolar term has the averaged form

$$\bar{\mathcal{H}}_d = -\frac{1}{2} \sum_{i>j}^N B_{ij} (3 I_{x_i} I_{x_j} - \vec{I}_i \cdot \vec{I}_j) = -\frac{1}{2} \mathcal{H}_{xx} \quad (5.22)$$

where the non-secular terms have been dropped since they average away in the interaction frame defined by the effective magnetic field term (see Section 4.2). In order for this dephasing term to be reversed by evolution under \mathcal{H}_{zz} after the pulse has ended, \mathcal{H}_{xx} must be transformed to \mathcal{H}_{zz} . This is accomplished by applying a $90_{\bar{Y}}$ pulse before the long continuous pulse Θ_X along \hat{x} , and a 90_Y pulse afterward. The magic echo sequence is written as $90_{\bar{Y}} - \Theta_X - 90_Y$. After this set of pulses has been

¹For systems where Ω_z has a large spread in frequency, it is not possible to set B_1 exactly on resonance for all spins.

applied, or at the end of the “burst”, the density matrix has the form

$$\rho(t) = \mathcal{R}_{90_Y} \mathcal{P}_{\Theta_X} \mathcal{R}_{90_{\bar{Y}}} \rho(0) \{inv\} \quad (5.23)$$

$$= e^{+i\frac{\pi}{2}I_y} e^{-\frac{i}{\hbar}(-\frac{1}{2}\mathcal{H}_{xx})t} e^{-i\frac{\pi}{2}I_y} \rho(0) \{inv\} \quad (5.24)$$

$$= e^{-\frac{i}{\hbar}(-\frac{1}{2}\mathcal{H}_{zz})t} \rho(0) \{inv\} \quad (5.25)$$

where it is assumed that the 90° pulses are delta function pulses and the average Hamiltonian from equation (5.22) is used to describe the action of the long Θ_X pulse. If the system is allowed to evolve freely under the dipolar Hamiltonian for a time t' after the burst, the density matrix becomes

$$\rho(t' + t) = e^{-\frac{i}{\hbar}(+\mathcal{H}_{zz})t'} e^{-\frac{i}{\hbar}(-\frac{1}{2}\mathcal{H}_{zz})t} \rho(0) \{inv\}. \quad (5.26)$$

This expression shows that the dipolar phase wrapping during the burst occurs at half the rate of rephasing outside of the burst. Clearly, the density matrix will return to its initial state $\rho(0)$ when $t' = \frac{1}{2}t$.

The magic echo sequence works well to refocus dipolar dephasing, but requires all spins to be on-resonance ($\delta B_z \approx 0$), as well as a long continuous pulse to force the average Hamiltonian to reduce to \mathcal{H}_{xx} . From our understanding of the average Hamiltonian description for multiple finite π -pulse sequences, we developed an analogous experiment to the Magic Echo. In contrast to the original magic echo, the following experiments allow refocusing of the dipolar dephasing using short strong pulses separated by time delays, simplifying implementation. Moreover, this sequence is more successful in the opposite limit, where $\delta B_z \neq 0$.

5.4.2 Magic Echo Analog

To build the magic echo analog sequence, the weak field term proportional to I_y in the zeroth order average Hamiltonian expression for the $\{\bar{X}, X\}$ block,

$$\bar{\mathcal{H}}_{\{\bar{X}, X\}}^{(0)} = \alpha \mathcal{H}_{zz} - \beta \mathcal{H}_{xx} + \lambda \Omega_z I_{yT}, \quad (5.27)$$

can be used to mimic the long continuous pulse in the original magic echo experiment as first proposed by Pines and Waugh [53].

This average field can be used to transform into a second toggling frame [45, 25, 53]. This second averaging procedure is no different than the truncation of the time-independent internal Hamiltonian from Section 4.2, except that here the proper quantization axis is determined by the average field along \hat{y} .

For the repeating block $\{\bar{X}, X\}$, it makes sense to work in the interaction frame of the Hamiltonian term proportional to I_{yT} in equation (4.54). In this reference frame, any terms proportional to \mathcal{H}_{yy} will pick up no time dependence and nonsecular terms from \mathcal{H}_{xx} will average to zero. If higher average Hamiltonian terms past first order are ignored, only the zeroth order term in equation (4.54) is non-zero. Using the replacement,

$$\mathcal{H}_{zz} = -\mathcal{H}_{xx} - \mathcal{H}_{yy} \quad (5.28)$$

the average Hamiltonian can be rewritten as

$$\bar{\mathcal{H}}_{\{\bar{X}, X\}}^{(0)} = \alpha \mathcal{H}_{zz} - \beta \mathcal{H}_{xx} + \lambda \Omega_z I_{yT} \quad (5.29)$$

$$= \alpha (-\mathcal{H}_{xx} - \mathcal{H}_{yy}) - \beta \mathcal{H}_{xx} + \lambda \Omega_z I_{yT} \quad (5.30)$$

$$= -(\alpha + \beta) \mathcal{H}_{xx} - \alpha \mathcal{H}_{yy} + \lambda \Omega_z I_{yT}. \quad (5.31)$$

In the second toggling frame, the field represented by I_{yT} should average out the

non-secular terms from \mathcal{H}_{xx} . It is easiest to pick out the non-secular terms by writing \mathcal{H}_{xx} in terms of the raising and lowering operators in this frame. For quantization along \hat{y} , the raising and lowering operators are

$$I_y^+ = I_z + iI_x \quad (5.32)$$

$$I_y^- = I_z - iI_x. \quad (5.33)$$

Making this substitution in the expression for \mathcal{H}_{xx} in equation (4.45) gives the three terms

$$\mathcal{H}_{xx} = \sum_{i=1}^N \sum_{j>i}^N B_{ij} \left[\frac{3}{4} \left(I_{y_i}^+ I_{y_j}^+ + I_{y_i}^- I_{y_j}^- \right) + \frac{1}{4} \left(I_{y_i}^+ I_{y_j}^- + I_{y_i}^- I_{y_j}^+ \right) - I_{y_i} I_{y_j} \right]. \quad (5.34)$$

In the second toggling frame, terms proportional to $I^+ I^+$ or $I^- I^-$ will pick up phase factors that oscillate at $\pm 2\lambda \frac{\Omega_z}{\hbar}$. The rapid oscillation of these terms can effectively average these terms to zero if the quantizing field is strong enough,¹ leaving

$$\mathcal{H}_{xx} \rightarrow \sum_{i=1}^N \sum_{j>i}^N B_{ij} \left[\frac{1}{4} \left(I_{y_i}^+ I_{y_j}^- + I_{y_i}^- I_{y_j}^+ \right) - I_{y_i} I_{y_j} \right] = -\frac{1}{2} \mathcal{H}_{yy}. \quad (5.35)$$

Using this in the expression for $\bar{\mathcal{H}}_{\{\bar{X}, X\}}^{(0)}$ in equation (5.31), the second averaged Hamiltonian is

$$\bar{\mathcal{H}}_{\{\bar{X}, X\}}^{(0)} = -\frac{\alpha - \beta}{2} \mathcal{H}_{yy} + \lambda \Omega_z I_{yT}, \quad (5.36)$$

which is similar to (5.22) for $\alpha > \beta$. As in Section 5.4.1, the dipolar term \mathcal{H}_{yy} in equation (5.36) can be manipulated by changing experimental parameters related to α , β and γ (equations (5.3)-(5.5)). In this case, adjusting the inter-pulse spacing

¹The term $\lambda \Omega_z$ is typically the same scale as \mathcal{H}_{zz} in many of our in our experiments. However, the Ω_z term can be magnified by introducing a resonance offset frequency Ω_P so that $\Omega_z = \Omega_z^{loc} + \Omega_P$, improving the second averaging approximation.

τ and pulse duration t_p controls the sign and magnitude of the dipolar term, and therefore determines the refocusing time of the echo.

Following the structure of the magic echo sequence, X-phase 90° wrapper pulses are used to transform $-\mathcal{H}_{yy}$ from $\bar{\mathcal{H}}_{\{\bar{X}, X\}}^{(0)}$ in equation (5.36) to $-\mathcal{H}_{zz}$. The pulse sequence has the form

$$90_X - \{90_{\bar{X}} - \{\bar{X}, X\}^N - 90_X\} - t_{\text{free}}$$

where the first 90_X pulse initializes system so that $\rho(0) = I_{y_T}$. Because the first two pulses are of opposite phase and are applied with no time delay in between them, the sequence can be simplified by dropping the first two pulses,

$$\{\bar{X}, X\}^N - 90_X - t_{\text{free}}.$$

A schematic of the pulse sequence is shown in Figure 5.6A. During the burst of length Nt_c when pulses are applied, the spin system develops under the average Hamiltonian

$$\bar{\mathcal{H}}_{\text{burst}} = -\frac{\alpha - \beta}{2} \mathcal{H}_{zz} - \lambda \Omega_z I_{z_T} \quad (5.37)$$

where the $90_{\bar{X}}$ and 90_X wrapper pulses have also transformed the average field term, $\lambda \Omega_z I_{y_T} \rightarrow -\lambda \Omega_z I_{z_T}$. After the burst, the system is allowed to freely evolve under the influence of the internal Hamiltonian alone

$$\mathcal{H}_{\text{int}} = \mathcal{H}_{zz} + \Omega_z I_{z_T}. \quad (5.38)$$

The density matrix in this case is given by

$$\rho(t') = e^{-\frac{i}{\hbar}(\mathcal{H}_{zz} + \Omega_z I_{z_T})t} e^{-\frac{i}{\hbar}(-\frac{\alpha - \beta}{2} \mathcal{H}_{zz} - \lambda \Omega_z I_{z_T})Nt_c} \rho(0) \{inv\} \quad (5.39)$$

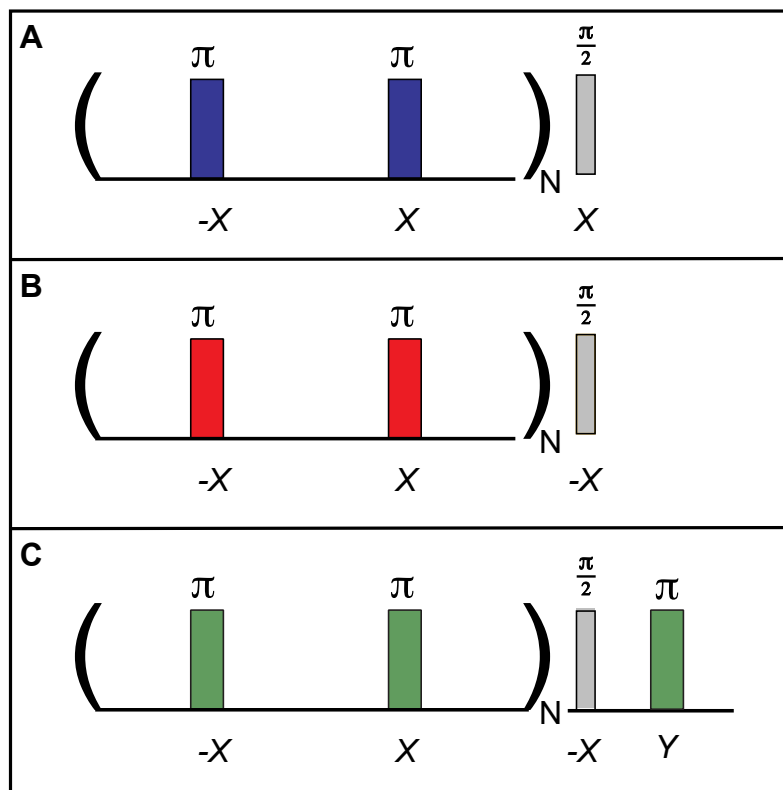


Figure 5.6: Schematic of the three pulse sequences inspired by the original magic echo experiment [42, 43], which all start with the sequence $\{\bar{X}, X\}$ repeated N times. Pulse phases are shown below the pulse diagram and rotation angle above.

where $t' = t + Nt_c$ is the total time elapsed, and t is the free evolution time after the burst has ended. During the burst, the system undergoes both Zeeman and dipolar dephasing at two different rates according to the dimensionless prefactors $\frac{\alpha-\beta}{2}$ and λ . This is followed by a faster rephasing in the free evolution period which can result in a spin echo.

By rearranging the density matrix in equation (5.39),

$$\rho(t') = e^{-\frac{i}{\hbar}(\mathcal{H}_{zz})(t-\frac{\alpha-\beta}{2}Nt_c)} e^{-\frac{i}{\hbar}(\Omega_z I_{zT})(t-\lambda Nt_c)} \rho(0) \{inv\}. \quad (5.40)$$

we can predict the time when the dipolar and Zeeman spin echoes should occur. From this equation we see that the Zeeman refocusing time, t_Z , and dipolar refocusing time, t_d , are

$$t_Z = \lambda Nt_c \quad (5.41)$$

$$t_d = \frac{\alpha - \beta}{2} Nt_c \quad (5.42)$$

after the burst has ended. The timing of the echo depends on the parameters α , β and λ which are related to the pulse sequence timings, τ and t_p [equations (5.3)-(5.5)]. Figure 5.7D in blue shows that the echo appears close to the predicted Zeeman refocusing time, t_Z , but with a slight delay. We believe that the terms ignored in this analysis are responsible for the discrepancy.

The formation of an echo also depends on the phase of the last 90° pulse, further validating the average Hamiltonian description of this behavior. If the $\{\bar{X}, X\}$ repeating blocks are followed by a $90_{\bar{X}}$ pulse as in Figure 5.6B, no echo is formed during free evolution (Figure 5.7D in red). For this phase choice, the the 90_X and $90_{\bar{X}}$ wrapper pulses transform the average field term from $\lambda\Omega_z I_{yT}$ to $+\lambda\Omega_z I_{zT}$. Since the spin operator I_{zT} has the same sign both during and after the burst, the Zeeman

dephasing continues at an even faster rate in the free evolution period. Although the dipolar phase behavior is unaltered by this change in the sequence and does get refocused, for this sample the large Zeeman dephasing ruins the magic echo that would otherwise form during the free evolution period.¹

At this point, it is important to emphasize that these sequences would not produce echoes in the delta function pulse approximation. A train of delta function π -pulses acting on a system of spins initially aligned along \hat{z} at equilibrium should have no effect on the system. The application of either a 90_X or $90_{\bar{X}}$ at the end of this pulse train would only produce an FID immediately after the last pulse in both experiments.

To better understand why the echo does or does not appear, we can follow the development of the respective Zeeman ($\Phi_Z(t')$) and dipolar ($\Phi_d(t')$) phase angles shown in **A**, **B**, and **C** of Figure 5.7. The density matrix can be rewritten as

$$\rho(t') = e^{-i\Phi_d(t')\tilde{\mathcal{H}}_{zz}} e^{-i\Phi_Z(t')\tilde{\mathcal{H}}_Z} \rho(0)\{inv\} \quad (5.43)$$

where the operators $\tilde{\mathcal{H}}_{zz} = \frac{\mathcal{H}_{zz}}{\Omega_d}$ and $\tilde{\mathcal{H}}_Z = \frac{\mathcal{H}_Z}{\Omega_z}$ are dimensionless and Ω_d is an energy scale inferred from the pure dipolar lineshape. During the burst, the Zeeman and dipolar phases evolve under the average Hamiltonian, $\tilde{\mathcal{H}}_{\text{burst}}$, in equation (5.37). Spins with slightly different Ω_z and Ω_d get more and more out of step with one another and begin to dephase. In the subsequent free evolution period, the spins rephase under \mathcal{H}_{int} , but now at a faster rate than the rate of dephasing. From the density matrix equation (5.40) and (5.43), we identify the following equations that describe

¹There is some evidence of the occurrence of a dipolar echo at t_d in the center graph of Figure 5.8. However, because this sample has a 100% filling factor, there is a spread in \vec{B}_1 that limits the application of our model.

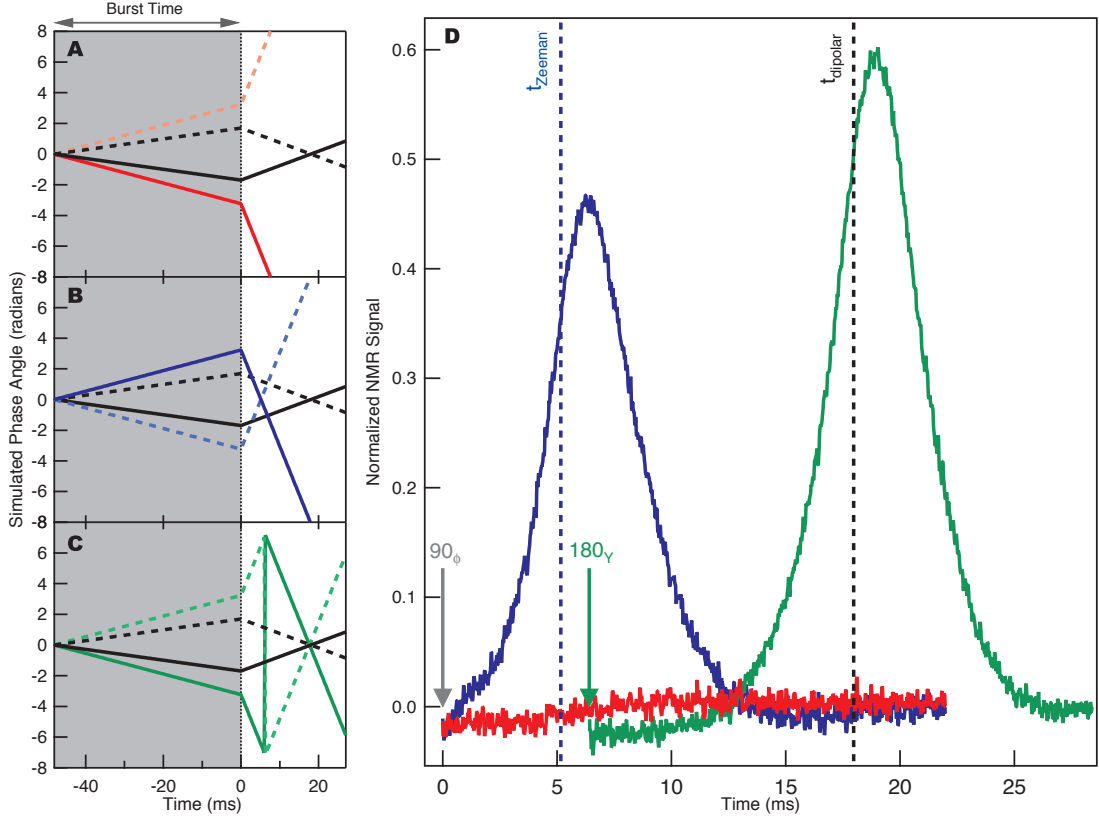


Figure 5.7: NMR data for ^{13}C nuclei in C_{60} at room temperature. Three experiments inspired by the magic echo [42, 43], which all start with the sequence $\{\bar{X}, X\}^N$. **A-C**. Simulated phase evolution of the Zeeman phase angle $\Phi_Z(t)$ and the dipolar phase angle $\Phi_d(t)$ [equations (5.44) and (5.45)] for each experiment in Figure 5.6. Representative values if $\frac{\Omega_z}{h} = \pm 100$ Hz and $\frac{\Omega_d}{h} = \pm 15$ Hz are shown (solid/dashed), with $\Phi_d(t)$ in black and $\Phi_Z(t)$ in the color of the experimental trace. During the grey shaded period, the dipolar and Zeeman phases evolve under $\bar{\mathcal{H}}_{\text{burst}}$. At the end of the burst, free evolution begins ($t = 0$ ms) and the phase develops under \mathcal{H}_{int} . **D**. Data is acquired after the last pulse in the sequence which is indicated in the plot. Following the repeating block with a $90_{\bar{X}}$ pulse does not cause an echo to form (red); with 90_X following the repeating block, a large echo emerges (blue); applying a 180_Y pulse at time t_{π_Y} after the burst of the failed sequence (red), an optimized echo appears (green). Dashed lines show the predicted echo times t_{Zeeman} and t_{dipolar} . $N=200$, $\tau = 50\mu\text{s}$, $\Omega_P = 0$, and $\alpha \approx 0.83$.

the phase wrapping and unwrapping of the spins.

$$\Phi_Z(t) = \begin{cases} \frac{\Omega_Z(\mp\lambda)(t + Nt_c)}{\hbar} & \text{if } -Nt_c \leq t < 0 \\ \frac{\Omega_Z(t \mp \lambda Nt_c)}{\hbar} & \text{if } t \geq 0 \end{cases} \quad (5.44)$$

$$\Phi_d(t) = \begin{cases} \frac{\Omega_d(-\frac{\alpha-\beta}{2})(t + Nt_c)}{\hbar} & \text{if } -Nt_c \leq t < 0 \\ \frac{\Omega_d(t - \frac{\alpha-\beta}{2}Nt_c)}{\hbar} & \text{if } t \geq 0 \end{cases} \quad (5.45)$$

where we have set $t = -Nt_c$ at the start of the burst and $t = 0$ for the start of the free evolution time. The sign of $\mp\lambda$ is determined by the phase choice $\pm X$ of the final 90° pulse. The crossing of $\Phi_Z(t)$ lines after the burst indicates the Zeeman refocusing time, t_Z , in equation (5.41) and the crossing of $\Phi_d(t)$ lines indicate t_d in equation (5.42). If the repeating block is followed by $90_{\overline{X}}$, the $\Phi_Z(t)$ lines in red not only fail to cross, but dephase at an even faster rate during the free evolution time (Figure 5.7A). Following the repeating block with 90_X -pulse forces the spins to rephase, shown by the crossing of the $\Phi_Z(t)$ lines at the time t_Z (Figure 5.7B). In both cases, a dipolar echo is suggested by the crossing of $\Phi_d(t)$ lines at t_d since the phase of the final 90_ϕ pulse does not effect the sign of the bilinear dipolar Hamiltonian. However, because the Zeeman dephasing is large at t_d , a dipolar echo is not observed in this sample for these conditions.

5.4.3 Optimized Magic Echo

The magic echo in the previous section can be enhanced by synchronizing the dipolar and Zeeman refocusing time. By inspecting the simulated phase angle for the experiment $\{\overline{X}, X\} - 90_X$ (Figure 5.7B), it is clear that the Zeeman refocusing time occurs closer to the start of the free evolution time than the dipolar refocusing time. Using the opposite pulse phase ($90_{\overline{X}}$) following the repeating block can stall the Zeeman

refocusing by allowing dephasing to continue at the beginning of the free evolution period. In order to flip the sign of the Zeeman term, a 180_Y pulse is applied at time t_{π_y} after the $90_{\bar{X}}$ (Figure 5.6) in the sequence

$$\{\bar{X}, X\}^N - 90_X - t_{\pi_y} - 180_Y.$$

After the π -pulse, the spins rephase under the influence of the operator $-\Omega_z I_{zT}$ (Figure 5.7C). Since \mathcal{H}_{zz} is not affected by the π -pulse, the corresponding time evolution operator is

$$e^{i\pi I_{yT}} e^{-\frac{i}{\hbar}(\mathcal{H}_{zz} - \Omega_z I_{zT})t} e^{-\frac{i}{\hbar}(\mathcal{H}_{zz} + \Omega_z I_{zT})t_{\pi_y}} e^{-\frac{i}{\hbar}\left(\frac{-(\alpha-\beta)}{2}\mathcal{H}_{zz} + \lambda\Omega_z I_{zT}\right)Nt_c} e^{-i\frac{\pi}{2}I_{xT}}. \quad (5.46)$$

Requiring that the dipolar $\Phi_d(t)$ and Zeeman $\Phi_Z(t)$ phases return to zero simultaneously provides a formula for the timing of the final 180_Y -pulse.

$$-t + t_{\pi_y} = -\lambda Nt_c \quad (5.47)$$

$$t + t_{\pi_y} = \frac{\alpha - \beta}{2} Nt_c \quad (5.48)$$

$$t_{\pi_y} = \frac{1}{4}(\alpha - \beta - 2\lambda) Nt_c \quad (5.49)$$

In this case, the optimized magic echo should appear after the burst at the dipolar echo time, $t_d = \frac{\alpha-\beta}{2} Nt_c$, as shown in Figure 5.7D in green. In practice, second averaging is not perfect and terms left out in this model have an effect on the refocusing time. In the optimized magic echo experiment in Figure 5.7, the measured echo appears at a slightly delayed time after the predicted time, indicating that there is more phase wrapping during the burst than is accounted for in this approximation.

The echo time can also be manipulated by increasing the length of the burst. Longer burst times allow more phase wrapping to occur before free evolution, pushing

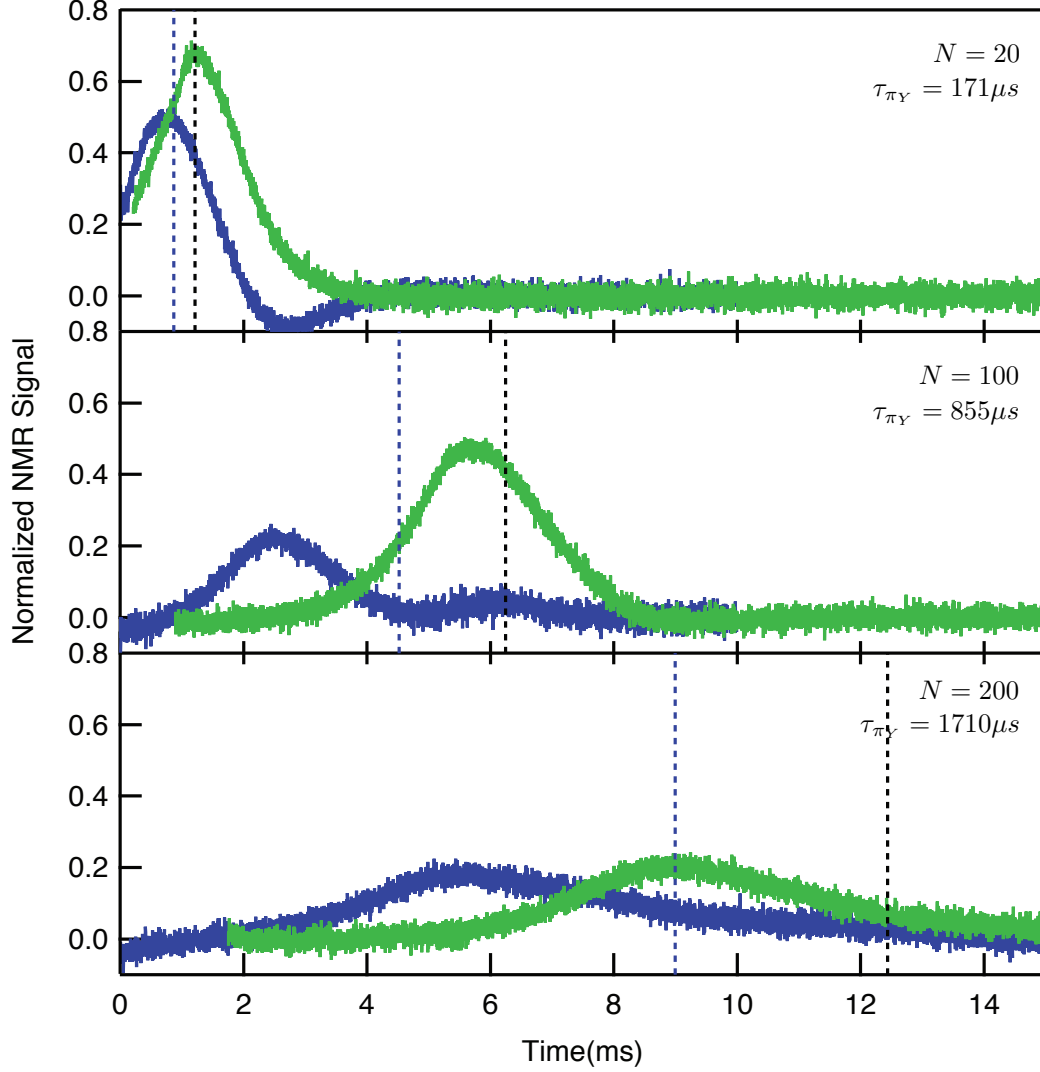


Figure 5.8: NMR data for ^{13}C nuclei in C_{60} at room temperature in a larger sample with a filling factor near 100%. The experiment $\{\overline{X}, X\}^N - 90_X$ is in blue and the optimized experiment $\{\overline{X}, X\}^N - 90_X - t_{\pi_Y} - 180_Y$ is in green. Data is acquired after last pulse in the sequence. The blue dashed line shows the t_Z refocusing time and black dashed line shows the dipolar refocusing time, t_d . Number of repeating blocks, N , and t_{π_Y} values are indicated in plot. $\tau = 40\mu\text{s}$, $\frac{\omega_1}{\pi} = 14$ kHz, and $\alpha \approx 0.69$.

the echo further out in time. The dependence of the echo time on burst length is clearly shown in Figure 5.8. In addition, for longer burst times less signal is recovered and the predicted time of the echo gets progressively worse. It is possible that higher order terms not included in the model so far will become more important at longer burst times. Unfortunately, the spread in ω_1 due to the 100% filling factor of this larger sample complicates the comparison to the simple model of a single ω_1 we used in this analysis.

However, the model used throughout this chapter gave reasonable and quantitative predictions that agreed with experiments, where the delta function pulse approximation would predict completely different behavior. In the delta function pulse limit, the π_y -pulses in the burst should preserve the the initial magnetization along I_z . As stated in the previous section, in the delta function pulse limit a 90_ϕ pulse should only produce a free induction decay if it acts on an initial density matrix proportional to I_z . In this scenario, applying a π -pulse sometime after an FID *should* produce a spin echo. Although the final 180_y -pulse has the same function as a π -pulse in the Hahn echo experiment, it is important to note that the time delay between the 90_ϕ and π -pulse is *not* the same length of time from the π -pulse to the echo. This shows definitively that phase wrapping must have taken place inside the burst itself and is a good quantitative test of the model.

Chapter 6

Quadratic Echo: Coherence

Control using $\bar{\mathcal{H}}^{(0)} + \bar{\mathcal{H}}^{(1)}$

In the previous chapter, alternating phase pulse sequences were used to demonstrate the existence of terms usually ignored in the strong pulse limit; $\{\bar{Y}, Y\}$ was used in the Hahn echo analog and $\{\bar{X}, X\}$ in the magic echo analog. Pulse sequences such as these, which have toggling frame Hamiltonians that satisfy $\tilde{\mathcal{H}}(t) = \tilde{\mathcal{H}}(t_c - t)$, are known as symmetric sequences in AHT. For symmetric sequences, the odd order average Hamiltonian corrections vanish [25, 38]. From the initial experiments in ^{29}Si , we knew that $\bar{\mathcal{H}}^{(1)}$ could play an important role in the spin evolution. However, the specific details of that role were difficult to tease out [4]. For this reason, we began our exploration of the AHT model using the repeating blocks $\{\bar{Y}, Y\}$ and $\{\bar{X}, X\}$ with $\bar{\mathcal{H}}^{(1)} = 0$ to design experiments that used only the zeroth term in the average Hamiltonian expansion.

Encouraged by the successful application of this model and the quantitative predictions it was able to make, we wondered if non-zero higher order terms could be utilized in similar ways. Despite being much smaller in scale, we knew from simula-

tions that under certain conditions $\bar{\mathcal{H}}_{\{\phi_1, \phi_2\}}^{(1)}$ could have large effects over the repetition of many π -pulses. Although it was initially unclear if the smaller corrections to the model would be useful in controlling dipolar and Zeeman evolution, the exploration of these smaller terms lead to the main building blocks we use in the line narrowing and MRI of solids sequences in the last chapter.

6.1 Building the Quadratic Echo Sequence

Following the methods of Chapter 5, we hoped to use a transverse field term to control Zeeman dephasing. The first instance of a transverse field term in the repeating $\{X, X\}$ block occurs in the first order average Hamiltonian shown below and in equation (4.53). This term, proportional to $\Omega_z^2 I_{xT}$, comes from the commutator $[\Omega_z I_{yT}, \Omega_z I_{zT}]$ in the expression

$$\begin{aligned} \bar{\mathcal{H}}_{\{X, X\}}^{(1)} = & \frac{i}{2\pi\hbar} \frac{t_p}{t_c} (t_p [\mathcal{H}_x^A, \mathcal{H}_x^S + \mathcal{H}_{xx}] \\ & + (8\tau + 2t_p) [\Omega_z I_{yT}, \Omega_z I_{zT} + \mathcal{H}_{xx}]). \end{aligned} \quad (6.1)$$

Concentrating on this term, equation (6.1) can be rewritten as

$$\bar{\mathcal{H}}_{\{X, X\}}^{(1)} = -(\kappa\Omega_z)^2 I_{xT} + \bar{\mathcal{H}}_{\{X, X\}}^{(1), non-I_{xT}} \quad (6.2)$$

where

$$\kappa^2 = \frac{t_p(8\tau + 2t_p)}{2\pi\hbar t_c} \quad (6.3)$$

and $\bar{\mathcal{H}}_{\{X, X\}}^{(1), non-I_{xT}}$ contains terms in $\bar{\mathcal{H}}_{\{X, X\}}^{(1)}$ not proportional to I_{xT} . By analogy, it was hoped that $(\kappa\Omega_z)^2 I_{xT}$ could be used in the same way that $\lambda\Omega_z I_{yT}$ was used in the magic echo analog experiment of Section 5.4.2, despite its much smaller size. Like the

transverse field term in the magic echo experiment, the term $(\kappa\Omega_z)^2 I_{x_T}$ could help to secularize the average Hamiltonian expression for $\{X, X\}$,

$$\bar{\mathcal{H}}_{\{X,X\}}^{(0)} = \alpha\mathcal{H}_{zz} - \beta\mathcal{H}_{xx}, \quad (6.4)$$

through second averaging. Rewriting $\bar{\mathcal{H}}_{\{X,X\}}^{(0)}$ in terms of \mathcal{H}_{xx} and \mathcal{H}_{yy} only,

$$\bar{\mathcal{H}}_{\{X,X\}}^{(0)} = \alpha(-\mathcal{H}_{xx} - \mathcal{H}_{yy}) - \beta\mathcal{H}_{xx} \quad (6.5)$$

$$= -(\alpha + \beta)\mathcal{H}_{xx} - \alpha\mathcal{H}_{yy}. \quad (6.6)$$

In the toggling frame of the average field represented by $(\kappa\Omega_z)^2 I_{x_T}$, the dipolar term \mathcal{H}_{yy} reduces to the secular $-\frac{1}{2}\mathcal{H}_{xx}$. Using this in the expression for $\bar{\mathcal{H}}_{\{X,X\}}^{(0)}$, gives

$$\bar{\mathcal{H}}_{\{X,X\}}^{(0)} = -(\alpha + \beta)\mathcal{H}_{xx} + \frac{\alpha}{2}\mathcal{H}_{xx} \quad (6.7)$$

$$= -\frac{\alpha + 2\beta}{2}\mathcal{H}_{xx} \quad (6.8)$$

$$= -\frac{1}{2}\mathcal{H}_{xx} \quad (6.9)$$

where $\alpha = \frac{4\tau}{t_c}$ and $\beta = \frac{t_p}{t_c}$ were used in the last step.

Although the scale of the quadratic term $(\kappa\Omega_z)^2 I_{x_T}$ is small for $\Omega_z \sim 0$, making second averaging hard to justify¹, the effective transverse field it represents grows quickly with an increasing resonance offset [45, 53]. In practice, increasing the resonance offset also changes some of the other terms in $\bar{\mathcal{H}}_{\{X,X\}}^{(1),non-I_{x_T}}$, which can lead to unwanted effects. It was hoped there might be a range of parameters where $\{X, X\}$ produced the desired second averaged Hamiltonian. Unfortunately, using the transverse field term for the sequence $\{X, X\}$ alone proved difficult. The terms

¹An alternative method, Secular Averaging Theory (SAT) [25] was also used to investigate the apparent paradox of a small $\bar{\mathcal{H}}^{(1)}$ term secularizing a larger $\bar{\mathcal{H}}^{(0)}$ term. Unfortunately, the relevant terms in $\bar{\mathcal{H}}^{(0)}$ and $\bar{\mathcal{H}}^{(1)}$ are identical in both AHT and SAT calculations.

in $\bar{\mathcal{H}}_{\{X,X\}}^{(1),non-I_{xT}}$ appeared to have larger impact as $\{X, X\}$ is repeated and cause fast decay as spins precess in the y - z plane.

Again, inspired by classic NMR experiments like the rotary echo and encouraged by the success of the Hahn echo analog experiment, we looked for repeating blocks with similar average Hamiltonian expressions, but with the opposite sign for the unwanted terms in $\{X, X\}$. The repeating block $\{\bar{X}, \bar{X}\}$, which uses π pulses with opposite phase compared to the block $\{X, X\}$, has an average Hamiltonian expression up to first order that is very similar to the expression for $\{X, X\}$. They share the same zeroth order average Hamiltonian expression,

$$\begin{aligned}\bar{\mathcal{H}}_{\{\bar{X},\bar{X}\}}^{(0)} &= \bar{\mathcal{H}}_{\{X,X\}}^{(0)} \\ &= \alpha\mathcal{H}_{zz} - \beta\mathcal{H}_{xx}\end{aligned}$$

while the first order average Hamiltonian term is opposite in sign,

$$\bar{\mathcal{H}}_{\{\bar{X},\bar{X}\}}^{(1)} = -\bar{\mathcal{H}}_{\{X,X\}}^{(1)} \tag{6.10}$$

$$= +(\kappa\Omega_z)^2 I_{xT} - \bar{\mathcal{H}}_{\{X,X\}}^{(1),non-I_{xT}}. \tag{6.11}$$

We found that the decay in the signal due to $\bar{\mathcal{H}}_{\{X,X\}}^{(1)}$ could be recovered by switching from the repeating block $\{X, X\}^N$ to the composite sequence $\{X, X\}^{\frac{N}{2}}\{\bar{X}, \bar{X}\}^{\frac{N}{2}}$.

However, this would also undo the effects related to transverse field term $(\kappa\Omega_z)^2 I_{xT}$ which would be used for net Zeeman phase wrapping. To show that the Ω_z^2 term was acting during the composite block burst and to help justify the model, we added another complication to the original sequence. We introduced phase coherent frequency

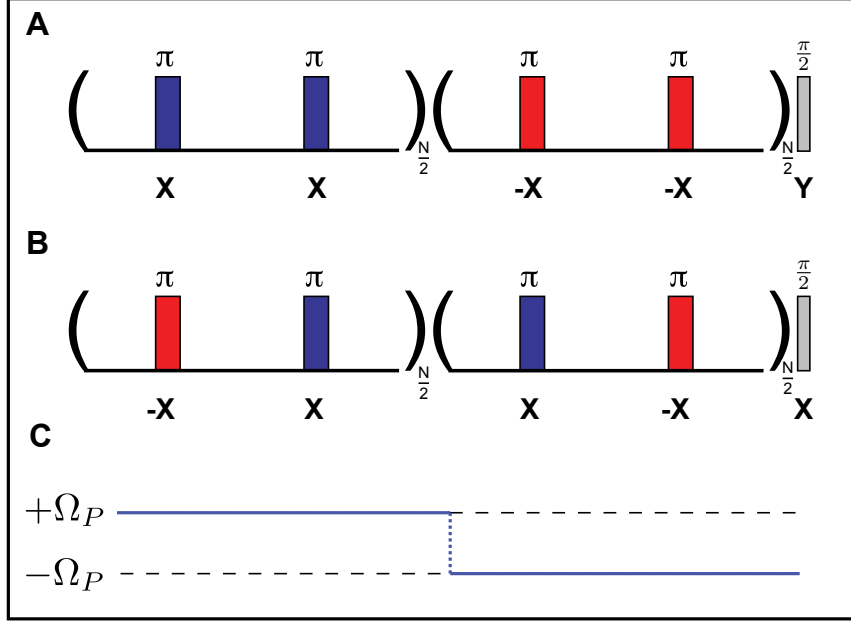


Figure 6.1: **A.** Schematic of the quadratic echo pulse sequence $\{X, X\}^{\frac{N}{2}} \{\bar{X}, \bar{X}\}^{\frac{N}{2}}$. **B.** The linear echo pulse sequence $\{\bar{X}, X\}^{\frac{N}{2}} \{X, \bar{X}\}^{\frac{N}{2}}$. **C.** Resonance offset is jumped to $+\Omega_P$ in the first time interval and $-\Omega_P$ in the second time interval for both pulse sequences.

jumping defined by

$$\Omega_{\text{net}}^+ = \Omega_z + \Omega_P \quad (6.12)$$

$$\Omega_{\text{net}}^- = \Omega_z - \Omega_P \quad (6.13)$$

where $\Omega_P = -h\nu_P$ and ν_P is the pulse transmitter frequency offset implemented on a Tecmag Apollo spectrometer. The frequency is jumped to Ω_{net}^+ in the first $\frac{N}{2}t_c$ time interval and to Ω_{net}^- in the second $\frac{N}{2}t_c$ time interval (Figure 6.1).

With the added frequency jumping, the time evolution operator during the burst has the full complicated form,

$$\mathcal{U}_{\text{burst}} = e^{-\frac{i}{\hbar} \left(\bar{\mathcal{H}}_{\{X,X\}}^{(0)} + (\kappa\Omega_{\text{net}}^-)^2 I_{x_T} - \bar{\mathcal{H}}_{\{X,X\}}^{(1), \text{non-}I_{x_T}} \right) \frac{Nt_c}{2}} e^{-\frac{i}{\hbar} \left(\bar{\mathcal{H}}_{\{X,X\}}^{(0)} - (\kappa\Omega_{\text{net}}^+)^2 I_{x_T} + \bar{\mathcal{H}}_{\{X,X\}}^{(1), \text{non-}I_{x_T}} \right) \frac{Nt_c}{2}}. \quad (6.14)$$

However, in the absence of frequency jumping most of the signal is recovered in the sequence $\{X, X\}^{\frac{N}{2}} \{\bar{X}, \bar{X}\}^{\frac{N}{2}}$. From this behavior, it was inferred that evolution of the system during the burst with frequency jumping follows the simpler time evolution operator,

$$\mathcal{U}_{\text{burst}} \approx e^{-\frac{i}{\hbar} \left(-\frac{1}{2} \mathcal{H}_{xx} + (\kappa \Omega_{\text{net}}^-)^2 I_{x_T} \right) \frac{Nt_c}{2}} e^{-\frac{i}{\hbar} \left(-\frac{1}{2} \mathcal{H}_{xx} - (\kappa \Omega_{\text{net}}^+)^2 I_{x_T} \right) \frac{Nt_c}{2}} \quad (6.15)$$

$$\approx e^{-\frac{i}{\hbar} \left(-\frac{1}{2} \mathcal{H}_{xx} - (2\kappa^2 \Omega_z \Omega_P) I_{x_T} \right) Nt_c}. \quad (6.16)$$

The overall resonance offset in $\Omega_{\text{net}}^\pm = \Omega_z \pm \Omega_P$ helps in second averaging, leading to the approximation $\bar{\mathcal{H}}_{\{X, X\}}^{(0)} \rightarrow -\frac{1}{2} \mathcal{H}_{xx}$. In addition, jumping the resonance offset in this pattern allows the cross term proportional to $\Omega_z \Omega_P$ to cause net dephasing from the beginning to end of the burst. If the approximations made so far are valid for this sample, the rate of phase wrapping that occurs during the burst could be directly controlled by Ω_P .

Following the technique in the magic echo to transform the I_{x_T} operators into I_{z_T} , a $90_{\bar{Y}}$ pulse is applied before the composite block and 90_Y pulse after. With an initializing 90° pulse along \hat{y} , the pulse sequence simplifies to

$$\{X, X\}^{\frac{N}{2}} \{\bar{X}, \bar{X}\}^{\frac{N}{2}} - 90_Y - t_{\text{free}}.$$

To test the model, the burst is followed by free evolution and $\Omega_P = 0$. After dephasing according to equation (6.16) during the burst, the effect is reversed under $\mathcal{H}_{\text{int}} = \mathcal{H}_{zz} + \Omega_z I_{z_T}$ during free evolution and an echo should appear. If there is no resonance offset during the burst, there is very little dephasing due to the small spread in Ω_z as well as a small global phase shift in the first half of the burst, but both of these effects are undone in the second half of the burst. In this model, if there is no resonance offset there is no net dephasing at the end of the burst. For this reason, the largest

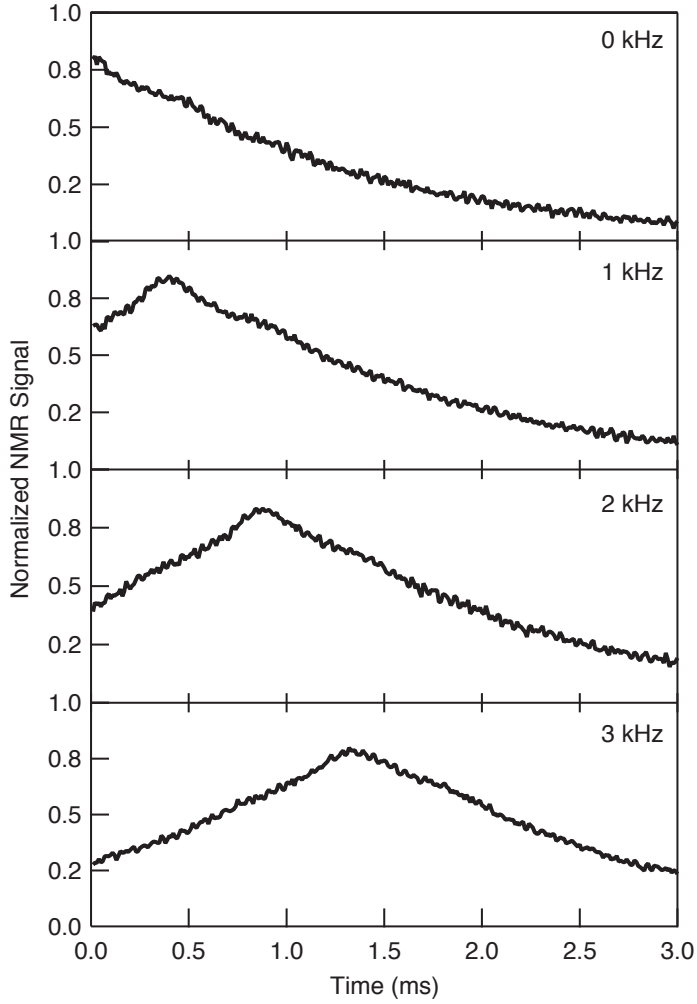


Figure 6.2: Quadratic echo experiments using the sequence $\{X, X\}^{\frac{N}{2}} \{\bar{X}, \bar{X}\}^{\frac{N}{2}} - 90_Y - t_{free}$, where the frequency is jumped according Figure 6.1, and the signal is acquired after the last 90_Y pulse. The off resonance frequency is increased from top to bottom, causing the quadratic echo peak to shift to later times in t_{free} . Sample C_{60} . $N=100$, $\tau = 10\mu s$, and $\alpha \approx 0.5$.

signal should be observed at the start of free evolution. As the off resonance value is increased, the rate of Zeeman dephasing during the burst is increased and the net phase wrapping at the end of the burst increases according to the cross term proportional to $\Omega_z \Omega_P I_{x_T}$. The larger the net phase wrapping built up during the burst, the longer it will take for the echo to appear. This dependence on Ω_P , shown in Figure 6.2, pushes the quadratic echo peak to later times in free evolution.

If the total time evolution operator is assumed to have the form

$$e^{-\frac{i}{\hbar}(\mathcal{H}_{zz} + \Omega_z I_{zT})t_{\text{free}}} e^{-\frac{i}{\hbar}\left(-\frac{1}{2}\mathcal{H}_{zz} - (2\kappa^2\Omega_z\Omega_P)I_{zT}\right)Nt_c} e^{-i\frac{\pi}{2}I_{yT}} \quad (6.17)$$

the Zeeman and dipolar refocusing times are

$$t_Z = 2\kappa^2\Omega_P Nt_c \quad (6.18)$$

$$t_d = \frac{1}{2}Nt_c. \quad (6.19)$$

Figure 6.3 shows good agreement with the Zeeman refocussing time predicted with this model over a large range of resonance offsets, although the echo appears slightly earlier due to terms that have been ignored. However, the linear dependence on Ω_P is clear.

As a tool to visualize the phase behavior during the burst and free evolution, phase diagrams are also shown in Figure 6.3A. For resonance offset settings $\frac{\Omega_P}{h} > 0$ Hz, there is a net phase difference proportional to $-\kappa^2\Omega_z\Omega_P$ between the representative values $\frac{\Omega_z}{h} = \pm 100$ Hz at the end of the burst. This Zeeman dephasing is undone by $+\Omega_z I_{zT}$ during free evolution, causing the echo to form. For the case $\frac{\Omega_P}{h} < 0$ Hz, the phase difference is proportional to $+\kappa^2\Omega_z\Omega_P$, so that dephasing simply continues during free evolution after the burst. As the frequency becomes more negative, the peak of the quadratic echo appears to recede into the burst so that only the trailing edge of the echo is visible during free evolution. Tracing the simulated phase “rays” during free evolution back into the burst in a straight line, analogous to ray tracing in geometric optics, shows where a “virtual” echo takes place (Figure 6.4).

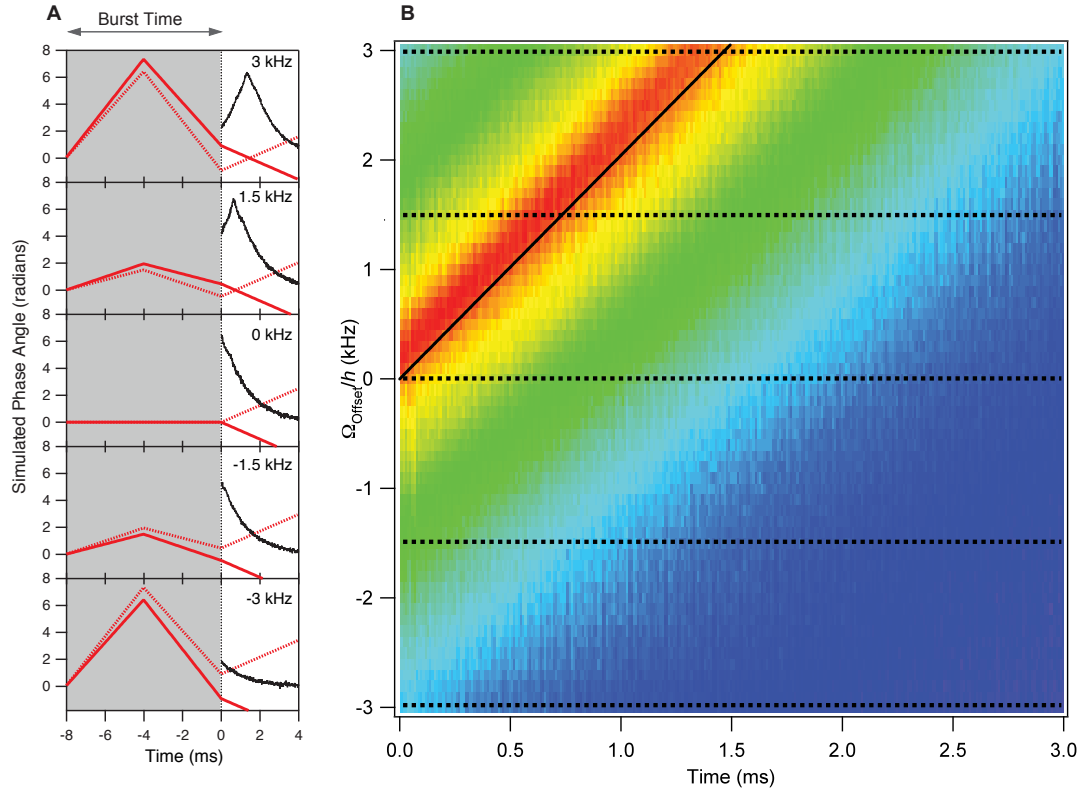


Figure 6.3: **A.** Simulated Zeeman phase angle during the quadratic echo burst in grey and during free evolution in white. Representative values of $\frac{\Omega_z}{h} = \pm 100$ Hz are shown (red solid/dashed). Resonance offset is increased from -3 kHz to $+3$ kHz. Free evolution begins at ($t = 0$ ms) where $\frac{\Omega_P}{h} = 0$ Hz. Corresponding slices from the image plot are shown in black. **B.** Image plot of 31 quadratic echoes for -3 kHz $\leq \frac{\Omega_P}{h} \leq 3$ kHz, in steps of 100 Hz. The black trend line shows the predicted Zeeman refocusing time. Black dashed lines indicate the slices that are displayed in **A.** Sample C_{60} . $N=100$, $\tau = 10\mu s$, and $\alpha \approx 0.5$.

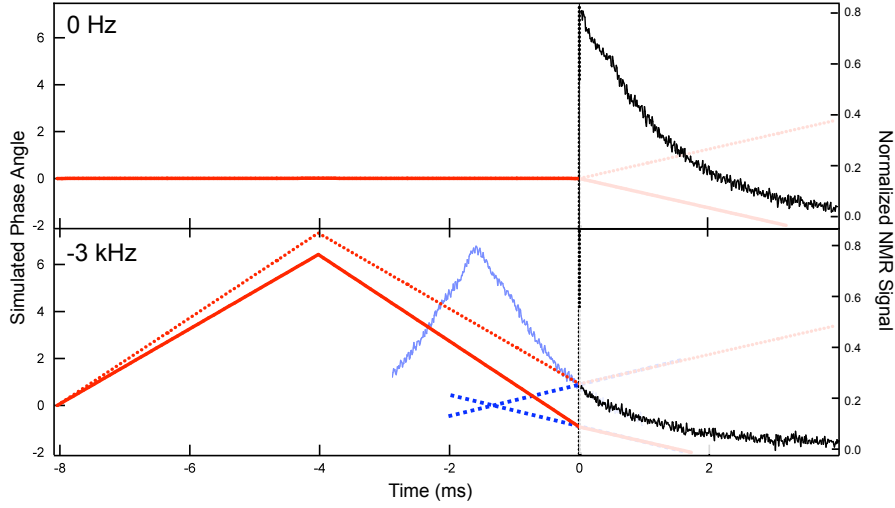


Figure 6.4: Simulated Zeeman phase angle during the quadratic echo burst on the left. Representative values of $\frac{\Omega_z}{h} = \pm 100$ Hz are shown (red solid/dashed). Quadratic echo data is shown on the right. Resonance offsets of 0 kHz and -3 kHz. Free evolution begins at ($t = 0$ ms) where $\frac{\Omega_P}{h}$ is set to 0 Hz. The projected virtual echo is shown in blue. Sample C_{60} . $N=100$, $\tau = 10\mu s$, and $\alpha \approx 0.5$.

6.2 Linear Echo

In contrast, the corresponding linear sequence

$$\{\bar{X}, X\}^{\frac{N}{2}} \{X, \bar{X}\}^{\frac{N}{2}} - 90_X - t_{free}$$

with the same frequency jump pattern (Figure 6.1) exhibits completely different behavior. Because $\{\bar{X}, X\}$ and $\{X, \bar{X}\}$ are symmetric sequences, the first order average Hamiltonian term vanishes. For these two repeating blocks, the average Hamiltonian expressions up to first order, which are linear instead of quadratic in Ω_z , are

$$\bar{\mathcal{H}}_{\{\bar{X}, X\}} = \alpha \mathcal{H}_{zz} - \beta \mathcal{H}_{xx} + \lambda \Omega_z I_{yT} \quad (6.20)$$

$$\bar{\mathcal{H}}_{\{X, \bar{X}\}} = \alpha \mathcal{H}_{zz} - \beta \mathcal{H}_{xx} - \lambda \Omega_z I_{yT}. \quad (6.21)$$

Following the same second averaging argument used the magic echo analog analysis from Section 5.4, the dipolar terms reduce to

$$\alpha\mathcal{H}_{zz} - \beta\mathcal{H}_{xx} \rightarrow -\frac{\alpha - \beta}{2}\mathcal{H}_{yy}. \quad (6.22)$$

For the burst $\{\bar{X}, X\}^{\frac{N}{2}}\{X, \bar{X}\}^{\frac{N}{2}}$ with the same frequency jumping pattern as the quadratic echo experiment (Figure 6.1), the time evolution operator has the approximate form

$$\mathcal{U}_{\text{burst}} \approx e^{-\frac{i}{\hbar}\left(-\frac{\alpha-\beta}{2}\mathcal{H}_{yy}-\lambda\Omega_{\text{net}}^-I_{yT}\right)\frac{Nt_c}{2}} e^{-\frac{i}{\hbar}\left(-\frac{\alpha-\beta}{2}\mathcal{H}_{yy}+\lambda\Omega_{\text{net}}^+I_{yT}\right)\frac{Nt_c}{2}} \quad (6.23)$$

$$\approx e^{-\frac{i}{\hbar}\left(-\frac{\alpha-\beta}{2}\mathcal{H}_{yy}\right)Nt_c} e^{-\frac{i}{\hbar}\left(\lambda\Omega_P I_{yT}\right)Nt_c} \quad (6.24)$$

Following the burst with a 90_X pulse and free evolution with $\Omega_P = 0$, the total unitary operator for this experiment is

$$e^{-\frac{i}{\hbar}\left(\mathcal{H}_{zz}+\Omega_z I_{zT}\right)t_{\text{free}}} e^{-\frac{i}{\hbar}\left(-\left(\frac{\alpha-\beta}{2}\right)\mathcal{H}_{zz}-\lambda\Omega_P I_{zT}\right)Nt_c} e^{-i\frac{\pi}{2}I_{xT}}. \quad (6.25)$$

The effect of changing the sign of Ω_P during the burst simply introduces a trivial global phase factor $e^{-i\phi I_{zT}}$ where $\phi = -\frac{\Omega_P}{\hbar}\lambda Nt_c$. This is followed by the dominant Zeeman dephasing that takes place during t_{free} , causing the largest signal to occur just after the burst for all Ω_P .

For each value of Ω_P , the net phase shift accumulated is the same for all spins at the end of the burst. As shown in the phase simulations from Figure 6.5 **A**, the phase trajectories of the representative isochromats with $\frac{\Omega_z}{\hbar} = \pm 100$ Hz drift away from each other during the first half of the burst, under the influence of the term $+\lambda(\Omega_z + \Omega_P)I_{yT}$. However, this dephasing is undone by $-\lambda(\Omega_z - \Omega_P)I_{yT}$ during the second half of the burst. The only remaining effect is the global phase shift due

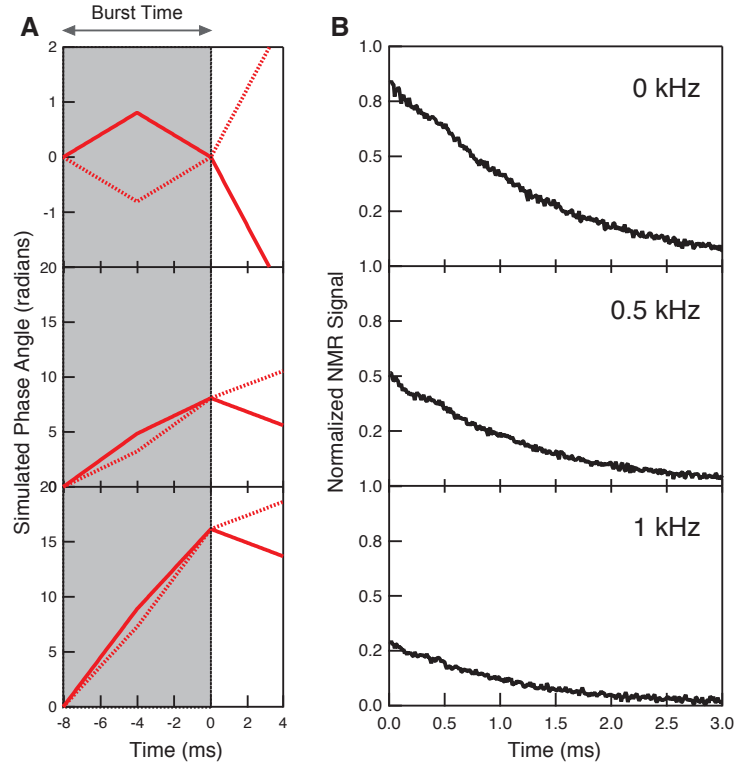


Figure 6.5: Linear echo experiments using the sequence $\{\bar{X}, X\}^{\frac{N}{2}}\{X, \bar{X}\}^{\frac{N}{2}} - 90_X - t_{free}$, where the frequency is jumped according to Figure 6.1. **A**. Simulated Zeeman phase angle during the linear echo burst in grey and during free evolution in white. Representative values of $\frac{\Omega_z}{h} = \pm 100$ Hz are shown (red solid/dashed). Resonance offset, ν_P , is increased from 0 kHz to 1 kHz. Free evolution begins at ($t = 0$ ms) where $\nu_P = 0$. **B**. Corresponding data taken for $t \geq 0$ ms is shown in black. Sample C₆₀. $N=100$, $\tau = 10\mu s$, and $\alpha \approx 0.5$.

to $+\Omega_P$ during both halves of the burst.

For larger values of Ω_P the overall phase shift only increases by the same amount for each spin. In all cases, the largest signal appears at the end of the burst, showing that our model is qualitatively correct. There is, however, a noticeable drop in amplitude as Ω_P is increased. Although this behavior is not predicted by the model, it is likely due to higher order terms proportional to Ω_P that were ignored in the analysis.

Chapter 7

Applications of the AHT model

The experiments shown so far are the first to demonstrate that the average Hamiltonian description outlined in Chapter 4 is quantitatively correct. In Chapter 5, using $\bar{\mathcal{H}}^{(0)}$ we developed a new class of spin echoes based on this model that would not work in the delta function pulse approximation. In Chapter 6, this approach was extended to include the non-zero $\bar{\mathcal{H}}^{(1)}$ using a combination of the pulse sequences $\{X, X\}$ and $\{\bar{X}, \bar{X}\}$. These experiments not only utilize small terms typically ignored when strong pulses are used, but emphasized these terms to great effect. With a solid understanding of the underlying finite pulse effects and a quantitative description, we can begin to ask what applications this approach might have in the many fields that utilize spin echoes in spin control.

Initially, some time was spent trying to use the average Hamiltonian expressions, $\bar{\mathcal{H}}^{(0)}$ of the burst in the magic echo analog experiment or $\bar{\mathcal{H}}^{(1)}$ of the quadratic echo, directly to control dipolar or Zeeman phase wrapping. In the end, the most progress was made using these as subunits in building much more complicated sequences. In this chapter, we will use these building blocks to develop exceptionally effective approaches to line narrowing and MRI of solids.

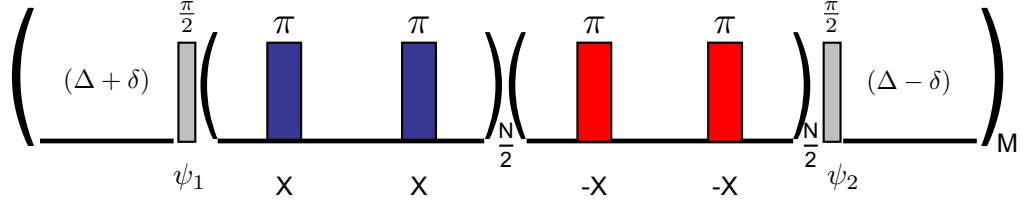


Figure 7.1: Schematic of the composite block pulse sequence $\{N, \delta, \psi_1, \psi_2\}^M$ based on the quadratic echo pulse sequence in Figure 6.1. The free evolution period $(\Delta + \delta)$ is followed by the burst, $90_{\psi_1} - \{X, X\}^{\frac{N}{2}} \{\bar{X}, \bar{X}\}^{\frac{N}{2}} - 90_{\psi_2}$ and then another free evolution period $(\Delta - \delta)$. The time interval $\Delta = \frac{Nt_c}{4}$ and $|\delta| \leq \Delta$. $\psi_i = \pm Y$ for $i = 1, 2$. The burst has a duration of $Nt_c = 4\Delta$, where $t_c = 4\tau + 2t_p$.

7.1 The Composite Block

In the previous chapter, the quadratic echo from Section 6.1 used non-zero $\bar{\mathcal{H}}^{(1)}$ terms to control the relative rate of both dipolar and Zeeman phase wrapping. To utilize this unique property, we designed the larger composite block

$$(\Delta + \delta) - 90_{\psi_1} - \{X, X\}^{\frac{N}{2}} \{\bar{X}, \bar{X}\}^{\frac{N}{2}} - 90_{\psi_2} - (\Delta - \delta)$$

where the time interval $\Delta = \frac{Nt_c}{4}$, $|\delta| \leq \Delta$, and $\psi_i = \pm Y$ for $i = 1, 2$. The burst, $90_{\psi_1} - \{X, X\}^{\frac{N}{2}} \{\bar{X}, \bar{X}\}^{\frac{N}{2}} - 90_{\psi_2}$, has a duration $Nt_c = 4\Delta$.¹ The total cycle time for larger composite block, which includes the duration of the burst and the two free evolution periods before and after the burst, is 6Δ . In shorthand notation, we will refer to this larger composite block as $\{N, \delta, \psi_1, \psi_2\}$.

If the wrapper pulses 90_Y and $90_{\bar{Y}}$ ($\psi_1 \neq \psi_2$) are used and $\Omega_z^{net} = \Omega_z + \Omega_P$ is held constant during the burst of duration 4Δ , equation (6.16) shows there will only be a

¹Including the finite time of 90_{ψ_i} wrapper pulses lengthens the burst duration to $Nt_c + t_p = 4\Delta + t_p$ and makes the average Hamiltonian description more complicated. In general, $t_p \ll Nt_c$, so we first try to ignore this term and assume that the 90_{ψ_i} are delta function rotations. However, we later found that the finite time of 90° wrapper pulses do have non-negligible effects over many repetitions, compared to the one or two inserted pulses of the experiments in Chapter 5. In order to achieve a quantitative description of the spin system behavior and optimize sequence performance, the finite pulse duration of these pulses must be taken into consideration.

net dipolar phase wrapping under $-\frac{1}{2}\mathcal{H}_{zz}$. This will be completely undone by $+\mathcal{H}_{zz}$ during the free evolution periods before and after the burst, with a total duration 2Δ .

The other case, $\psi_1 = \psi_2$, can be interpreted as a simplification of the sequence $90_Y - \{X, X\}^{\frac{N}{2}} \{\bar{X}, \bar{X}\}^{\frac{N}{2}} - 90_{\bar{Y}} - 180_Y$ where the last two pulses occur with no time delay between them. The combination $90_{\bar{Y}} - 180_Y$ can be simplified to 90_Y making both wrapper pulses the same. However, written in this expanded way, it is easier to see that average Hamiltonian of the burst has the same form for both cases $\psi_1 \neq \psi_2$ and $\psi_1 = \psi_2$, causing dipolar phase wrapping under $-\frac{1}{2}\mathcal{H}_{zz}$. What is left is the so-called ‘‘hidden’’ π -pulse which has no effect on the dipolar term. However, the hidden π -pulse does flip the sign of \mathcal{H}_Z during one of the free evolution periods outside the burst, leading to a different evolution.

If we ignore the finite duration of the 90° wrapper pulses for now and use the same approximations from the quadratic echo experiments, the corresponding unitary operators for the two composite repeating blocks are

$$e^{-\frac{i}{\hbar}(\Omega_z^{net} I_{zT})2\Delta} \quad \text{for } \psi_1 \neq \psi_2 \quad (7.1)$$

$$\mathcal{R}_{180_Y} e^{-\frac{i}{\hbar}(\Omega_z^{net} I_{zT})2\delta} \quad \text{for } \psi_1 = \psi_2 \quad (7.2)$$

From these equations, it is easily seen that this block design prevents net dipolar evolution over the total 6Δ cycle time. There is only a net Zeeman phase wrapping of either $+2\Omega_z^{net}\Delta$ or $+2\Omega_z^{net}\delta$, depending upon the choice of ψ_i .

7.2 Time Suspension Sequence

Inspection of equation (7.2) shows that both the dipolar and Zeeman dephasing will be completely refocused if $\psi_1 = \psi_2$ and $\delta = 0$. This pattern yields a time suspension sequence [54], which will result in a narrowed spectrum provided that the signal is

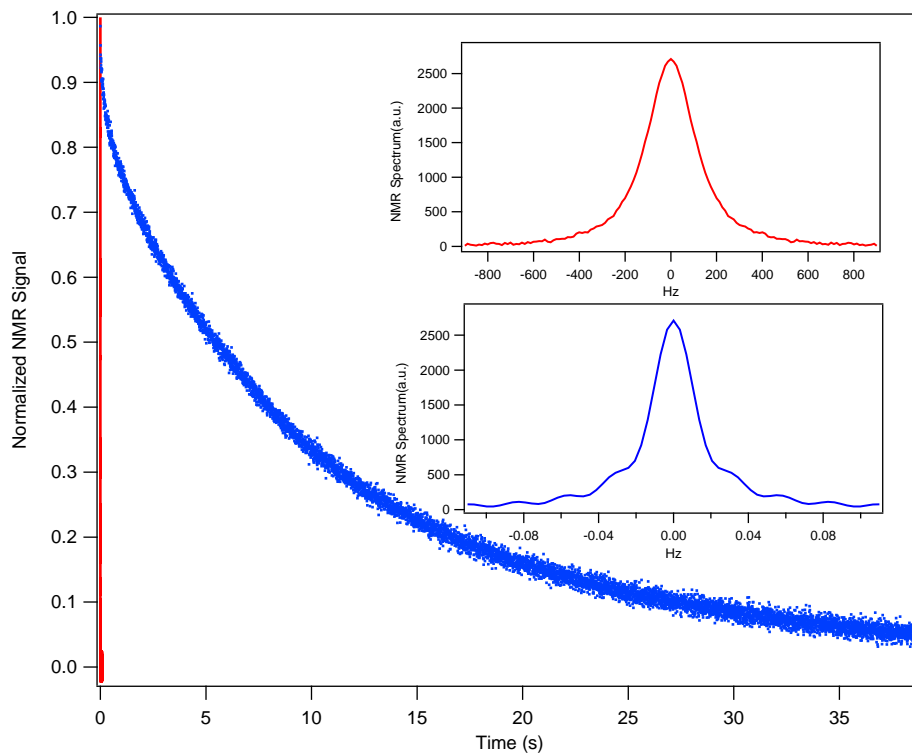


Figure 7.2: Time-suspension data on ^{13}C in C_{60} taken by Yanqun Dong using the sequence $90_X - \{2, 0, \bar{Y}, \bar{Y}\}^{9600}$ with $\tau = 22\mu\text{s}$, $\frac{\omega_1}{2\pi} \sim 25\text{kHz}$, $\nu_P = -3.5\text{ kHz}$ (blue) The line narrowed signal extends far beyond the normal C_{60} FID with $\nu_P = 0\text{ Hz}$ (red). The inset shows the 260 Hz normal spectrum (red) is narrowed to 0.03 Hz centered at ν_P . From reference [5].

acquired at the end of each $\{N, 0, \psi_1, \psi_1\}$ block.

The data in Figure 7.2 taken by Yanqun Dong shows the line narrowing sequence applied to ^{13}C in C_{60} [5]. Using a Tecmag LapNMR spectrometer with a “synth8” synthesizer, our time suspension narrows the normal line width from 260Hz to 0.03Hz. Much work was done to find the optimal parameters (N , ν_P , t_c , etc.) to overcome experimental roadblocks in order to achieve such extreme line narrowing, which Dr. Dong details in her thesis [5].

Encouraged by the successful application of these ideas to very clean and simple samples such C_{60} and ^{29}Si , we wondered if our sequences could help in the study of some important biomaterials, despite the more complicated spin environment. We

decided to use our model to investigate bone and tooth samples, since the \mathcal{H}_{int} studied in this dissertation is similar to that of ^{31}P in these materials [55, 56].

Figure 7.3 shows our line narrowing sequence used on a human deciduous (i.e. baby) tooth and cattle bone sample. Application of the sequence $90_X - \{2, 0, Y, Y\}^m$ on the tooth sample narrows the 3.4 kHz line width to 11 Hz and to 8 Hz in the bone sample. In these experiments both transmitter and receiver were set to a global resonance offset $\nu_P = 3\text{kHz}$ which is where the narrowed spectra are centered. The resonance offset helps improve the second averaging approximation we use in our model. However, increasing ν_P by too much results in decreased performance for $\nu_P > 3\text{kHz}$, as higher order corrections of $\bar{\mathcal{H}}^{(n)}$ or other error terms become larger and have greater impact on the spin evolution.

Removing the effects of \mathcal{H}_Z and \mathcal{H}_{zz} with the line narrowing sequence reveals a residual line width that is most likely due to small fluctuating fields in the sample [10, 14]. In bone samples, it is likely that the fluctuations are caused by random proton hopping near the phosphorus atoms [56] and are not refocused. The small amount of decay this causes does not necessarily detract from this method of line narrowing since it shows that our sequence is potentially helpful in measuring small interactions in a spin Hamiltonian that are normally obscured by the larger \mathcal{H}_Z and \mathcal{H}_{zz} interactions.

Achieving such long decay times in these samples pushed the limits of our older spectrometer. Through a series of experiments [5] and discussions with our spectrometer manufacturer, we realized our initial experiments were limited not by the fluctuating fields, but by random phase noise of the “synth5” pulse synthesizer in the Apollo spectrometer. To improve our experiments we eventually purchased a new generation spectrometer from Tecmag, an Apollo HF2, with a “synth8” pulse synthesizer that had a longer phase coherence time. With this spectrometer, Figure

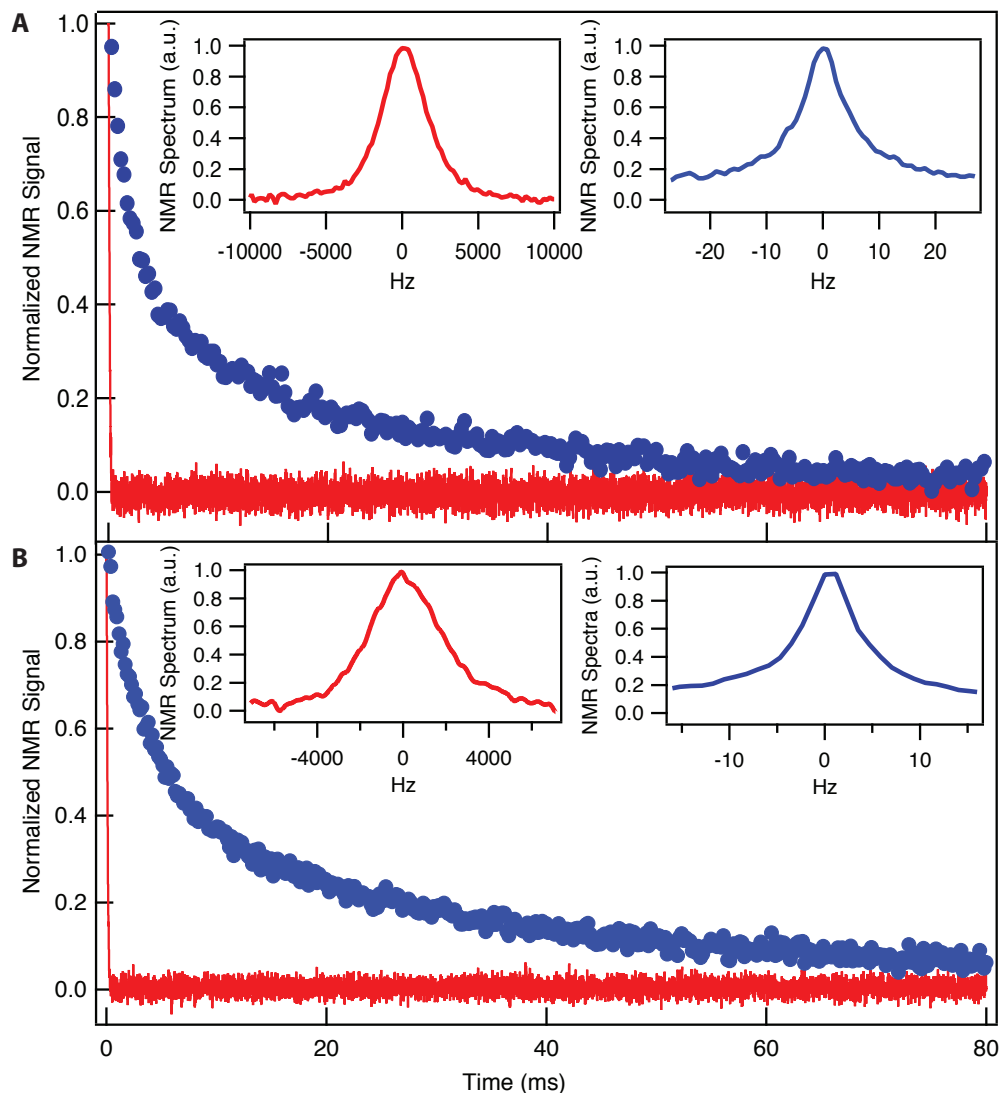


Figure 7.3: Line narrowing sequence $90_X - \{2, 0, Y, Y\}^{1500}$ applied to ^{13}P NMR of two biological samples: **(A)** a human deciduous tooth ($\tau = 20 \mu\text{s}$) and **(B)** a cattle bone ($\tau = 12 \mu\text{s}$) at room temperature. $\nu_P = 3 \text{ kHz}$, pulse strength $\frac{\omega_1}{2\pi} \approx 80 \text{ kHz}$ and $B_{ext} = 12 \text{ Tesla}$. The line narrowing sequence yields signal (blue) that extends well beyond the normal FID with $\nu_P = 0 \text{ Hz}$ (red). Insets show the Fourier transformations of the decay curves. The **(A)** 3.4 kHz (**(B)** 3.4 kHz) normal spectrum (red) is narrowed by a factor of $\sim 300(500)$, down to 11 Hz (8 Hz), centered at ν_P . These factors were limited by the phase noise of the Tecmag Apollo “synth5” spectrometer at this 206.95 MHz Larmor frequency.

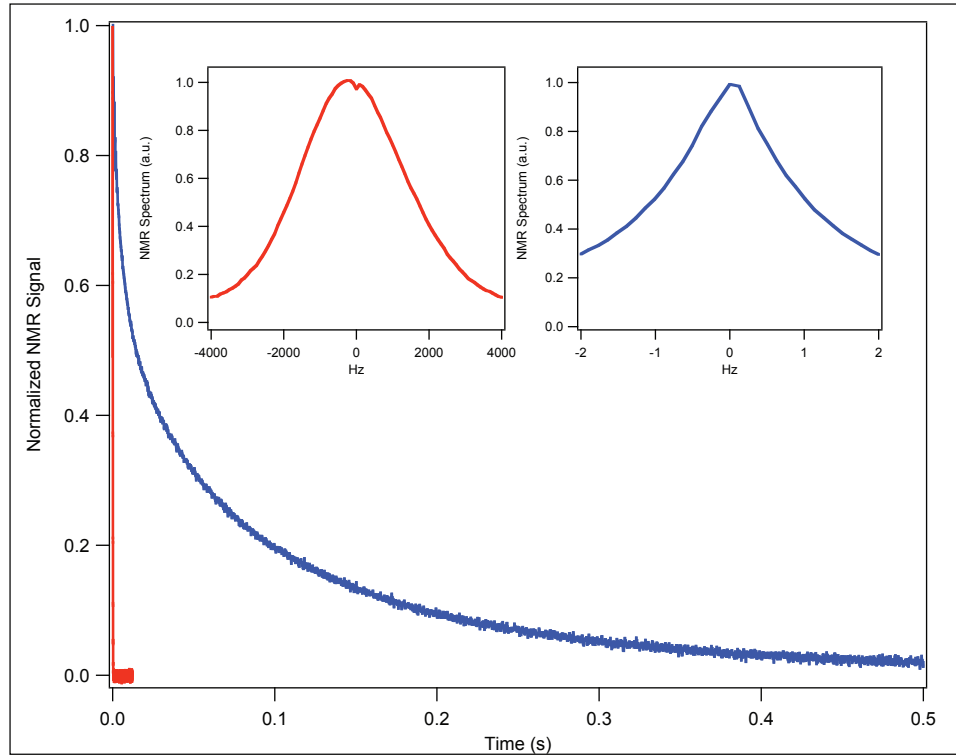


Figure 7.4: Line narrowing sequence $90_X - \{N, 2, Y, Y\}^{1500}$ applied to ^{13}P NMR of a human deciduous tooth using an improved Tecmag Apollo HF2 “synth8” spectrometer at a Larmor frequency of 206.95 MHz. Pulse strength $\frac{\omega_1}{2\pi} \approx 17$ kHz, $\tau = 5 \mu\text{s}$, $\nu_P = 7$ kHz, $B_{ext} = 12$ Tesla at room temperature. The line narrowing sequence improves by a factor of ~ 6 with upgraded equipment. Insets show the Fourier transformations of the decay curves. The 3.8 kHz normal spectrum (red) is narrowed by a factor of ~ 1900 , down to 3 Hz, centered at ν_P .

7.4 shows we were able to push the spectral line width in the tooth sample down by another factor of 5.

7.3 MRI sequence

A major challenge in the MRI of solids is to overcome line broadening effects from the strong dipole-dipole interaction. In liquid state NMR, extremely sharp lines are common due to motional narrowing [9, 10]. The rapid tumbling of molecules in the liquid state effectively averages the out line broadening mechanisms found in many solids. In imaging experiments, these types of line broadening interactions can overwhelm the smaller Zeeman shift which encodes the spatial information through field gradients, resulting in a wide structureless line and low spatial resolution. In the previous section, the composite block was designed to halt both Zeeman and dipolar evolution. Here we use the composite block $\{N, \delta, \psi_1, \psi_2\}$ where $\psi_1 \neq \psi_2$ from Section 7.1 which allows for Zeeman evolution. Because this composite block can measure pure Zeeman shift information without dipolar dephasing, we hoped it could be useful in the MRI [54, 57, 58] or MR microscopy [59] of solids.

Applying a linear magnetic field gradient across a uniform sample encodes the spatial information that will be used in creating an image. The local field, and therefore the resonance frequency, a nucleus experiences will depend on its position in the field gradient.

A magnetic field gradient across a uniform test sample produces a uniform spread in Ω_z^{net} . This results in a Zeeman spectrum with a box top or top-hat line shape. Measuring a spectrum like this is the first step toward imaging solids, using the back-projection technique [58, 60, 61]. To mimic a box top lineshape, we used a discrete set of Ω_P to move the narrow C_{60} spectrum to particular off-resonance positions.

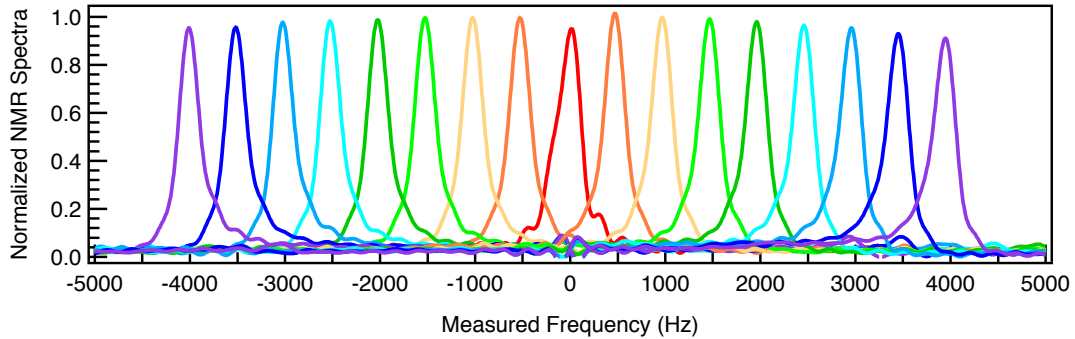


Figure 7.5: Reproduction of a top-hat line shape in C_{60} taken by Yanqun Dong using sequence $90_X - \{2, t_0, -Y, -Y\} - \{2, 0, -Y, Y\}^{30}$ with $\tau = 22\mu s$, and $t_0 = 0$. Each trace is the measured spectrum of a pseudo-FID [5] with different ν_P , for $-4 \text{ kHz} \leq \nu_P \leq +4 \text{ kHz}$ in steps of 500 Hz, covering the range $2\pi|\nu_P|/\omega_1 \leq 16\%$. To obtain this full bandwidth, the pseudo-FID interleaves a second data set using the same sequence, but with $t_0 = -(\frac{\Delta}{2} + \frac{1}{2\omega_1})$. From reference [62].

Figure 7.5 shows a faithful reproduction of the input top-hat spectrum taken by Yanqun Dong, where each spectrum is the Fourier transformation of the pseudo-FID resulting from two interlaced data sets [5]. Both the signal amplitude and the ν_P values have been accurately reconstructed using this approach. The individual peaks in the spectra are slightly narrowed compared to the input spectra since \mathcal{H}_{zz} has been removed. However, due to the small dipolar linewidth (FWHM = 38Hz) compared to the much larger Zeeman linewidth (FWHM = 260Hz), there is very little improvement on spatial resolution from removing dipolar evolution.

7.3.1 High Resolution MRI Sequence

Although the MRI sequence performed well, there was very little improvement over a traditional box top spectrum that would include both Zeeman and dipolar evolution. Somewhat unsatisfied with the top hat spectrum in C_{60} , we wondered if there was a way of improving the resolution. The limiting factor on the resolution in Figure 7.5 is

the width of the individual peaks. The width of each peak in Figure 7.5 is a measure of the internal Zeeman spread Ω_z^{loc} , while its position in the box top spectrum is determined by the global resonance offset Ω_P . We wanted to design a sequence that would refocus both the Zeeman and dipolar dephasing while retaining the global offset we impose with our spectrometer. The sequence we developed combines the refocussing properties of the time suspension sequence in Section 7.2 with the frequency jumping technique used in the quadratic echo sequence in Section 6.1.

In the time suspension sequence, the hidden π -pulse flips the sign of the Ω_z^{net} term. If the free evolution time before the burst is equal to the free evolution time after the burst ($\delta = 0$), there should be no net Zeeman phase wrapping. However, we want to preserve the Ω_P term in $\Omega_z^{net} = \Omega_z + \Omega_P$ to generate a box top spectrum.

Recall from Section 6.1 that we used phase coherent frequency jumping defined by

$$\Omega_{\text{net}}^+ = \Omega_z + \Omega_P \quad (7.3)$$

$$\Omega_{\text{net}}^- = \Omega_z - \Omega_P \quad (7.4)$$

to bring out the quadratic nature of the Ω_z^{net} term. To retain the resonance offset information while using the time suspension sequence, the frequency is jumped from $+\Omega_P$ to $-\Omega_P$ in every other 2Δ free evolution period. We also keep $\Omega_P \neq 0$ during the bursts since this magnifies the transverse field term we use in our model for second averaging. Figure 7.6 shows two phase jump patterns that preserve Ω_P while simultaneously eliminating the effects of $\Omega_z^{loc} I_{zT}$ and \mathcal{H}_{zz} in our model. Notice that the two schemes have the same resonance offset settings during the free evolution periods, but have opposite Ω_P during the bursts.

Our early attempts of the high resolution MRI experiment used the sequence

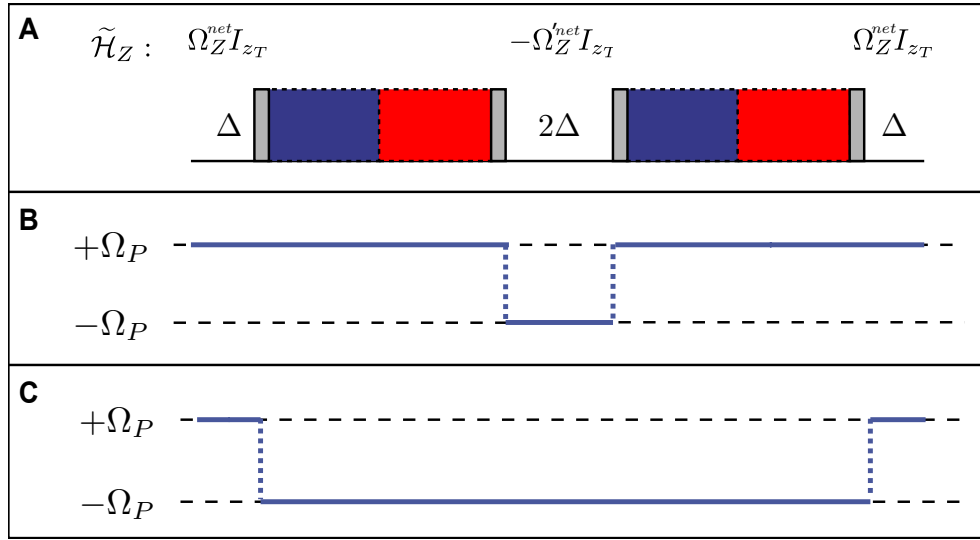


Figure 7.6: (A) Schematic of the high resolution MRI pulse sequence. To implement the phase jumping technique, at least two composite blocks of $\{N, 0, \psi, \psi\}$ are needed. The 90_ψ wrapper pulses are shown in grey, the $\{X, X\}^{\frac{N}{2}}$ is the block in blue and $\{\bar{X}, \bar{X}\}^{\frac{N}{2}}$ is the block in red. (Compare to Figure 7.1). Signal is acquired during the 2Δ free evolution time between bursts. Shown above the free evolution period is the toggling frame Hamiltonian expression for the Zeeman term, $\tilde{\mathcal{H}}_Z$. In our model, $\tilde{\mathcal{H}}_Z$ is not present during the bursts. (B) and (C) show two resonance offset jump patterns that preserve the resonance offset information, Ω_P .

$\{2, 0, \bar{Y}, \bar{Y}\}$ since that was successful in line narrowing experiments done on C_{60} (Figure 7.2) while the frequency jump pattern used $+\Omega_P$ during the first burst and $-\Omega_P$ during the second. However these attempts showed poor line narrowing or unpredictable behavior as Ω_P was varied.

In previous experiments we found that the 90_ψ wrapper pulses had non-negligible effects over many repetitions [5] and we suspected they might contribute to the loss of signal and strange behavior in these first high resolution MRI experiments. In our simplified model, it should not matter if the resonance offset is set to $+\Omega_P$ or $-\Omega_P$ since, during the bursts, we only use the offset to improve second averaging. In practice, the sign of the resonance offset had an impact on the performance of the 90_ψ wrapper pulses. With guidance from theory, but mostly through trial and error, we found that it was important for all four 90_ψ wrapper pulses to have the same ψ (e.g. all 90_Y as opposed to two 90_Y followed by $90_{\bar{Y}}$) and were applied with the same Ω_P setting.

Although it is hard to explain exactly why one pattern of wrapper pulses gives better performance than another, calculating an average Hamiltonian description for 90_ψ wrapper pulses could offer some guidance in optimizing the pulse sequence further. The AHT calculation using non-zero during 90_ψ wrappers showed some similarities between the repeating π -pulse sequence $\{Y, Y\}$ and the composite block $\{2, 0, Y, Y\}$. Likewise, a similar connection was found between $\{\bar{Y}, \bar{Y}\}$ and the composite block $\{2, 0, \bar{Y}, \bar{Y}\}$.¹ In all four of these cases, there is no effective transverse field term in $\bar{\mathcal{H}}^{(0)}$, only terms proportional to \mathcal{H}_{zz} and \mathcal{H}_{yy} , but there is one in $\bar{\mathcal{H}}^{(1)}$ proportional to $\Omega_z^2 I_{yT}$. This term switches sign when changing from $\{2, 0, Y, Y\}$ ² to $\{2, 0, \bar{Y}, \bar{Y}\}$ ².

¹The average Hamiltonian calculation for the 90_ψ wrapper pulses is actually over two composite blocks (i.e. The full cycle is $\{2, 0, Y, Y\} - \{2, 0, Y, Y\}$ or $\{2, 0, \bar{Y}, \bar{Y}\} - \{2, 0, \bar{Y}, \bar{Y}\}$) to satisfy the requirement in equation (4.8) that \mathcal{H}_{rf} is cyclic. It also uses the average Hamiltonian description of the quadratic echo sequence from Section 6.1 as \mathcal{H}_{int} between the wrapper pulses, treating the wrapper pulses as the only \mathcal{H}_{rf} .

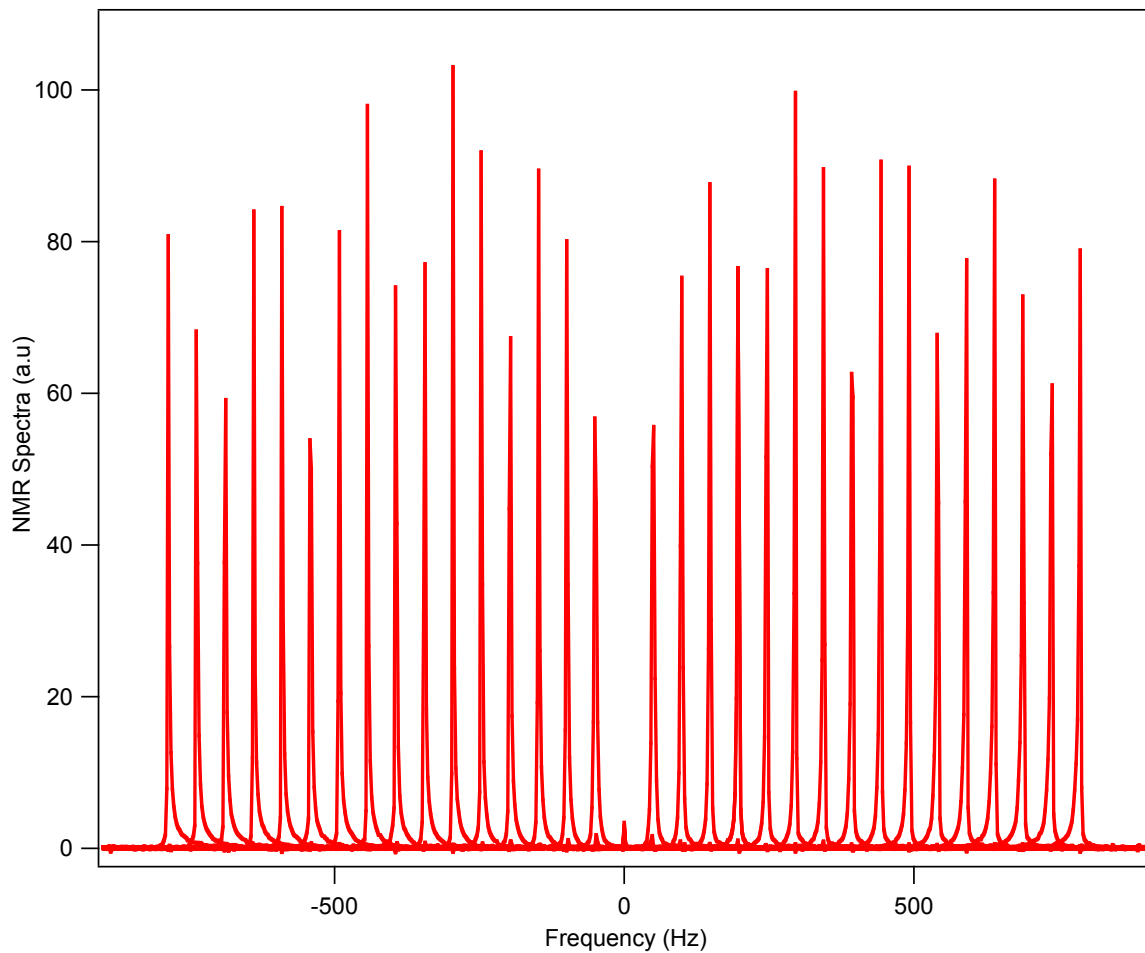


Figure 7.8: Reproduction of a high resolution top-hat lineshape in the C_{60} sample using the sequence $90_X - \left\{ \{2, 0, \bar{Y}, \bar{Y}\}^2 - \{2, 0, Y, Y\}^2 \right\}^{800}$ and the frequency jump pattern shown in Figure 7.7B. $\tau = 22 \mu\text{s}$ and $\frac{\omega_1}{2\pi} \approx 24 \text{ kHz}$. Each trace is the measured spectrum of an oscillating time suspension signal with different ν_P , for $-800\text{Hz} \leq \nu_P \leq +800 \text{ kHz}$ in steps of 50 Hz. Resolution is improved by a factor of > 50 over the box top spectrum in Figure 7.5.

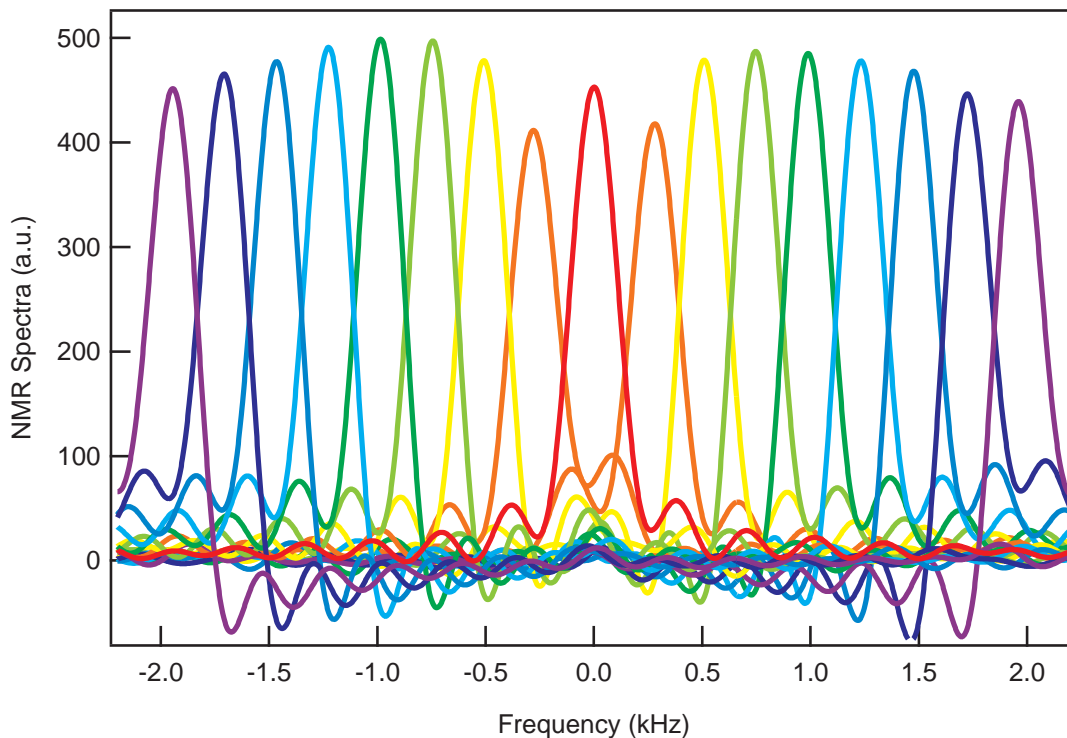


Figure 7.9: Reproduction of a high resolution top-hat line shape in human deciduous tooth sample using the sequence $90_X - \left\{ \{2, 0, \bar{Y}, \bar{Y}\}^2 - \{2, 0, Y, Y\}^2 \right\}^{1000}$ and the frequency jump pattern shown in Figure 7.7, with $\tau = 5 \mu\text{s}$ and $\frac{\omega_1}{2\pi} \approx 28.9 \text{ kHz}$. Each trace is the measured spectrum of an oscillating time suspension signal with different ν_P , for $-2 \text{ kHz} \leq \nu_P \leq +2 \text{ kHz}$ in steps of 250 Hz. ^{31}P NMR with a 206 MHz Larmor frequency at room temperature.

by factor of > 50 over the box top spectrum, which would result in a much higher spatial resolution when used in MRI.

This experiment was also done on the human deciduous tooth sample. Figure 7.9 shows the high resolution MRI box top spectrum. Each individual peak has a FWHM $\sim 250 \text{ Hz}$, a factor of 14 improvement over the full line width and worse by a factor of 80 compared to the line narrowing experiment.

It is difficult to say anything conclusive about why this particular pattern gave the best results. In the average Hamiltonian calculations for $\{Y, Y\}$, there were many terms that were very hard to interpret [3, 4, 5, 24], particularly those in $\bar{\mathcal{H}}^{(1)}$. The

sequences here are even more complex and we have made many assumptions to make the average Hamiltonian calculations more tractable. Many terms and interactions have been left out, which, no doubt, have an important role in the spin evolution.

7.4 Comparison to Current Methods and Future Challenges

Current approaches to the MRI of solids [54, 57, 63] require $\Omega_P = 0$ Hz during the burst to effectively eliminate dipolar dephasing. This constrains the timing and magnitude of gradient pulses used in these experiments [58]. In comparison, our approach does not need to switch off the applied Zeeman gradient during the bursts, which enables the slow ramping and application of large field gradients at moderate cost. It should also be possible to implement standard frequency- and phase-encoding methods using this approach [10, 58].

We are encouraged by the results of our sequences on the biological samples in this chapter and feel they may also have some potential applications in proton (^1H) NMR. However for protons, and many other important nuclei, the dipolar broadening dominates the magnetic broadening while our model works best in the opposite limit $\|\mathcal{H}_Z\| \geq \|\mathcal{H}_{ZZ}\|$.

To try to reach this limit a large Ω_P can be used, as demonstrated in the adamantane proton NMR experiment in Figure 7.10. Although these results are encouraging, the model used in this dissertation is not well suited for the adamantane system due to the larger scale of $\|\mathcal{H}_{int}\|$. To make our original model using only the first two terms of the average Hamiltonian expansion more applicable to this system, t_c would need to be reduced, which is not easy to do using a typical coil and our current spectrometer. Specifically, higher order corrections to $\bar{\mathcal{H}}$ are necessary for a good

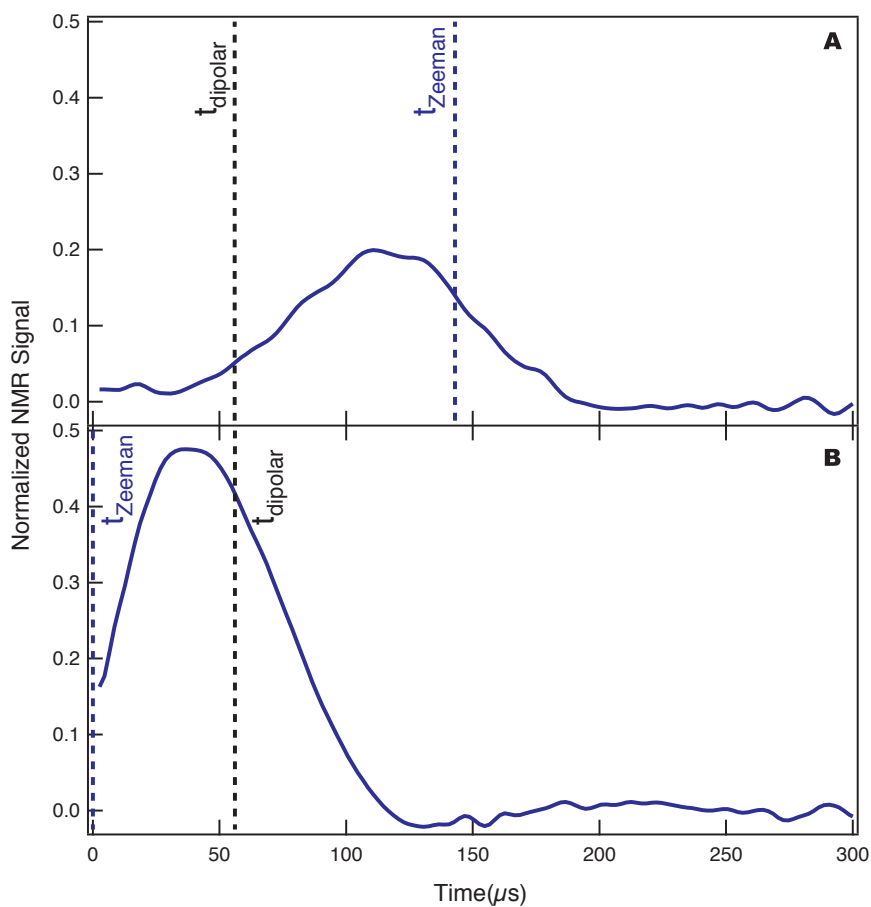


Figure 7.10: Proton NMR in Adamantane ($C_{10}H_{16}$) at room temperature. **A.** An echo using the magic echo analog sequence $\{\overline{X}, X\}^N - 90_X$ as in Figure 5.7, but with $\nu_P = -25$ kHz. **B.** Echo is improved using the composite sequence $\{\overline{X}, X\}^{\frac{N}{2}} \{X, \overline{X}\}^{\frac{N}{2}} - 90_{\overline{X}}$ and $\nu_P = 25$ kHz. The pulse strength $\frac{\omega_1}{2\pi} \approx 89.3$ kHz is approximately 6 times bigger than the 15 kHz linewidth of 1H in adamantane, with a 127.79 Larmor frequency at $B_{ext} = 3$ Tesla. $N = 20$ and $\tau = 5.6 \mu s$

description the behavior. As an alternative approach, microcoils [64, 65, 66] can be used to reach shorter t_p which also reduces t_c .

7.4.1 Concluding Remarks

While these limitations must be acknowledged, it should be clear that this work has potential in many areas in science. When pulses are strong, they are conventionally approximated as instantaneous delta functions, causing perfect rotations. However, after many years of close study and experimentation we have found that the finite duration of real pulses, even in the strong pulse limit, can contribute strikingly large effects when many phase-coherent pulses are applied. By identifying and exploiting the main Hamiltonian terms that arise from the finite duration of pulses, we were able to demonstrate new classes of spin echoes. The exploration of these typically ignored terms also guided us in the design of effective approaches to line narrowing and MRI of solids. Exploiting the internal structure of strong π -pulses provides experimentalists with yet another technique to control the coherent evolution of quantum systems, which has applications far beyond NMR. In quantum information processing, this may be a particularly useful tool to beat the limit on pulse control fidelity that is imposed by non-zero \mathcal{H}_{int} during any real pulse. It should also be noted that related effects can occur for a wider variety of \mathcal{H}_{int} and $\mathcal{H}_{\mathcal{P}_\phi}$ [3] than has been discussed in this dissertation, provided that $[\mathcal{H}_{int}, \mathcal{H}_{\mathcal{P}_\phi}] \neq 0$. Beyond NMR, the model Hamiltonian is common in ESR and in spectroscopy of pseudo-spins (e.g., superconducting qubits), making this work directly applicable to all these systems.

Appendix A

Phase Transients

Although the ideal square pulse has a perfectly square shape with a single frequency and single phase, sudden changes in amplitude or phase are hard to achieve without rf distortions. For this reason, phase transients at the beginning and end of pulses are always present and can lead to unintentional spin rotations [67, 68, 69].

To measure the real pulses in our experiments, a pick up loop was positioned near the NMR coil and the signal from the pick up coil was measured while pulses were applied (Figure A.1). Although the sign and phase of the transients are highly dependent on the individual tank circuit, resonance frequency and tuning, the phase transients in our Hahn echo analog experiment most likely had the asymmetric form shown in Figure A.1.

This phase pattern was confirmed by using average Hamiltonian theory to analyze the effect the phase transients during the $\{\bar{Y}, Y\}$ and $\{Y, \bar{Y}\}$ repeating blocks and observing these effects in the experiments. The phase transients in our Hahn echo analog experiment can be approximated in an average Hamiltonian analysis by including a small angle X -phase pulse before the 180_Y pulse and a small \bar{X} -phase pulse afterward [69], both of time duration ϵ . Similarly, for the $180_{\bar{Y}}$ pulses, a small angle \bar{X} -phase pulse is added before the π -pulse and a small angle X -phase pulse

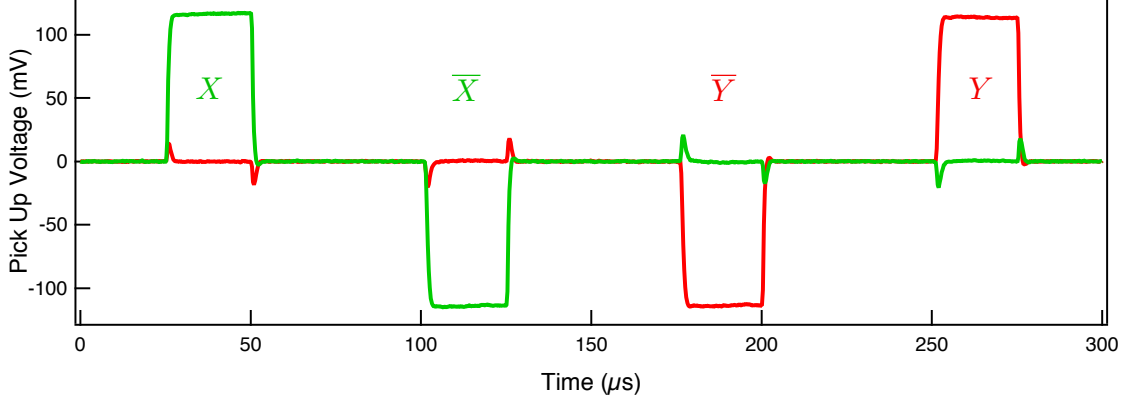


Figure A.1: Measured pulse shapes of X , \bar{X} , \bar{Y} and Y -phase pulses at radio frequency 128.56 MHz with pulse strength $\frac{\omega_1}{2\pi} = 25\text{kHz}$. Pulse length of $25\mu\text{s}$ is comparable in length to the π pulses used throughout this dissertation.

afterward, also with time duration ϵ . In the toggling frame of the π -pulses, all four phase transients in a repeating block have the same phase, (i.e. \bar{X} for $\{\bar{Y}, Y\}$ and X for $\{Y, \bar{Y}\}$). Because the effect of the phase transients adds constructively, the spins feel the effect of a constant field pointing along either $-\hat{x}$ or \hat{x} , causing the oscillations present in Figures 5.1 to 5.5. Interestingly, in the other pulse sequences these effects either cancel out over a full cycle or do not cause any rotations.

The inclusion of phase transients adds an extra term proportional to ϵ to original expression of the zeroth order average Hamiltonian. For example, for $\{\bar{Y}, Y\}$ the zeroth order average Hamiltonian expression from equation (5.15) becomes

$$\bar{\mathcal{H}}_{\{\bar{Y}, Y\}}^{(0)} = \bar{\mathcal{H}}_{\{Y, Y\}}^{(0)} - \frac{4t_p}{\pi t_c} \Omega_z I_{x_T} - \frac{4\epsilon}{t_c} \hbar \omega_1 I_{x_T}. \quad (\text{A.1})$$

To test this description, the racetrack Hahn echo analog experiment was performed at different off resonance settings (Figure A.2). If a pulse transmitter offset is introduced, $\Omega_z \rightarrow \Omega_z + \Omega_P$, the signal will appear to be on-resonance under the condition

$$\frac{4t_p}{\pi t_c} \Omega_P I_{x_T} = \frac{4\epsilon}{t_c} \hbar \omega_1 I_{x_T}. \quad (\text{A.2})$$

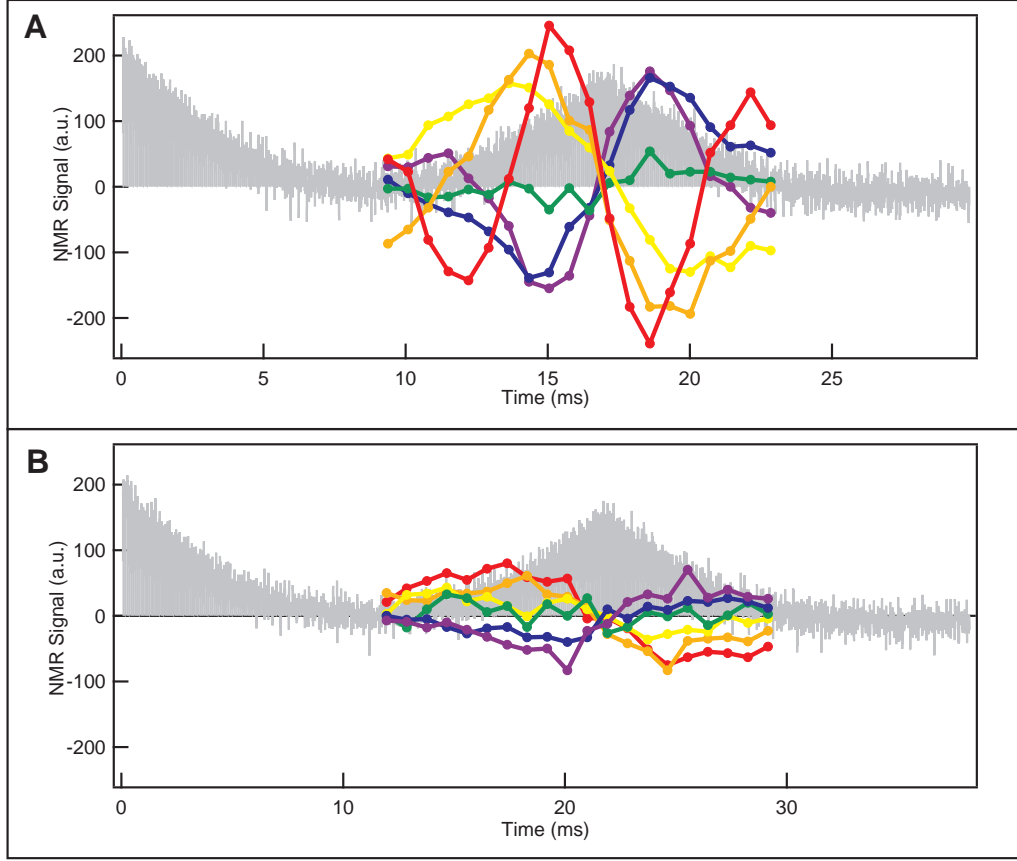


Figure A.2: Quadrature detection in the Hahn echo analog experiment at varying resonance offsets. Original Hahn echo analog experiment, $90_X - \{\bar{Y}, Y\}^{N_1} \{Y, \bar{Y}\}^{N_2}$ in grey and detection along z -axis, $90_X - \{\bar{Y}, Y\}^{N_1} \{Y, \bar{Y}\}^{N_2} - 90_X$, in color. **A.** “On resonance” signal occurs at $\nu_P \approx 500\text{Hz}$. $t_p = 20.9\mu\text{s}$. Rainbow traces taken from $+250\text{Hz}$ to -1000Hz in steps of $+250\text{Hz}$. **B.** “On resonance” signal occurs at $\nu_P \approx 100\text{Hz}$. $t_p = 40.5\mu\text{s}$. Rainbow traces taken from -25Hz to -150Hz in steps of $+25\text{Hz}$. Sample C_{60} . $\tau = 25\mu\text{s}$, and $\alpha \approx 0.5$ $N_1 = 100$, $N_2 = 100$ for Hahn echo analog experiment and $N_2 = 5, 10, 15, \dots, 100$ for detection along the z -axis.

Using the fact $\omega_1 = \frac{\pi}{t_p}$, the signal would appear to be on-resonance when

$$\Omega_P = \frac{\pi^2 \hbar \epsilon}{t_p^2}. \quad (\text{A.3})$$

When this off resonance setting was equal and opposite to the average field generated by the phase transients, the signal observed along the y -axis, Figure A.2 in grey, no longer had the oscillations observed for $\Omega_P = 0$ in Figure 5.5.

As another test, changing the pulse strength should change the offset frequency needed to satisfy the condition in equation (A.3). Since the length of the phase transients is constant, determined by the Q of the circuit, the small average field produced by the phase transients should decrease with decreasing pulse strength. Also, reducing the pulse strength lengthens t_p to satisfy the condition $\pi = \frac{\omega_1}{t_p}$. These two effects combined will effect the transmitter frequency needed to produce a signal that appears on-resonance. As shown by the $\frac{1}{t_p^2}$ dependence in equation (A.3), reducing the pulse strength by half should reduce the the transmitter frequency by a factor of four. In Figure A.2 **B**, grey, the pulse strength was reduced by a factor of two, which resulted in a reduction of Ω_P from ~ 500 Hz to ~ 100 Hz to produce a signal that appeared to be on resonance. This reduction is close to the expected factor of four.

In color, z -channel measurements (see Section 5.3) are also shown in varying resonance offsets. Oscillations along the z -axis are present when the resonance offset is larger or smaller than average field generated by phase transients and no oscillation (green) is present when the resonance offset cancels the phase transient field. In combination, z -channel and y -channel measurements show the nutation of the magnetization about the small average field along the x -axis produced by the phase transients.

Bibliography

- [1] B. E. Kane. A Silicon-Based Nuclear Spin Quantum Computer. *Nature*, **393**(6681), 133–137 (1998).
- [2] A. E. Dementyev, D. Li, K. MacLean, and S. E. Barrett. Anomalies in the NMR of Silicon: Unexpected Spin Echoes in a Dilute Dipolar Solid. *Physical Review B*, **68**(15), 1–4 (2003).
- [3] D. Li, A. Dementyev, Y. Dong, R. Ramos, and S. Barrett. Generating Unexpected Spin Echoes in Dipolar Solids with pi Pulses. *Physical Review Letters*, **98**(19), 190401–4 (2007).
- [4] D. Li. *Unexpected Spin Echoes in Dipolar Solids: Intrinsic Effects of Finite Pi Pulses on Quantum Coherence*. Ph.D. thesis, Yale University (2007).
- [5] Y. Dong. *Effects of Hard but Finite π Pulses: From Uncontrolled Coherence Flow to Extreme Line-narrowing and MRI of Solids*. Ph.D. thesis, Yale University (2009).
- [6] E. Purcell, H. Torrey, and R. Pound. Resonance Absorption by Nuclear Magnetic Moments in a Solid. *Physical Review*, **69**(1-2), 37 (1946).
- [7] F. Bloch. Nuclear Induction. *Physical Review*, **70**(7-8), 460 (1946).

- [8] F. Bloch, W. W. Hansen, and M. Packard. The Nuclear Induction Experiment. *Phys. Rev.*, **70**(7-8), 474–485 (1946).
- [9] A. Abragam. *The Principles of Nuclear Magnetism*. The International series of monographs on physics. Clarendon Press, Oxford (1983).
- [10] C. P. Slichter. *Principles of Magnetic Resonance*. Springer Verlag, Berlin, 3rd edition (1996).
- [11] B. Cowan. *Nuclear Magnetic Resonance and Relaxation*. Cambridge University Press, Cambridge, United Kingdom (1997).
- [12] I. Rabi, N. Ramsey, and J. Schwinger. Use of Rotating Coordinates in Magnetic Resonance Problems. *Reviews of Modern Physics*, **26**(2), 167–171 (1954).
- [13] R. R. Ernst, G. Bodenhausen, and A. Wokaun. *Principles of Nuclear Magnetic Resonance in One and Two Dimensions*, volume 14. Clarendon Press, Oxford (1987).
- [14] E. Fukushima and S. B. Roeder. *Experimental Pulse NMR: a Nuts and Bolts Approach*. Addison-Wesley Pub. Co., Advanced Book Program, Reading, Mass. (1981).
- [15] F. Bloch and A. Siegert. Magnetic Resonance for Nonrotating Fields. *Physical Review*, **57**(6), 522–527 (1940).
- [16] R. R. Ernst and W. A. Anderson. Application of Fourier Transform Spectroscopy to Magnetic Resonance. *Review of Scientific Instruments*, **37**(1), 93–102 (1966).
- [17] D. DiVincenzo. Two-Bit Gates are Universal for Quantum Computation. *Physical Review A*, **51**(2), 1015–1022 (1995).

- [18] D. DiVincenzo and D. Loss. Quantum Computers and Quantum Coherence. *Journal of Magnetism and Magnetic Materials*, **200**(1-3), 202 – 218 (1999).
- [19] M. A. Nielsen and I. L. Chuang. *Quantum Computing and Quantum Information*. Cambridge University Press (2000).
- [20] B. E. Kane. Silicon-Based Quantum Computation. *Fortschritte Der Physik-Progress of Physics*, **48**(9-11), 1023–1041 (2000).
- [21] R. Vrijen, E. Yablonovitch, K. Wang, H. W. Jiang, A. Balandin, V. Roychowdhury, T. Mor, and D. DiVincenzo. Electron-Spin-Resonance Transistors for Quantum Computing in Silicon-Germanium Heterostructures. *Physical Review A*, **62**(1), art. no.–012306 (2000).
- [22] T. D. Ladd, J. R. Goldman, F. Yamaguchi, Y. Yamamoto, E. Abe, and K. M. Itoh. All-Silicon Quantum Computer. *Physical Review Letters*, **89**(1), 017901 (2002).
- [23] A. E. Dementyev. *Spin in the Quantum Hall Effect: OPNMR Studies of Skyrmions and Composite Fermions*. Ph.D. thesis, Yale University (2004).
- [24] D. Li, Y. Dong, R. Ramos, J. Murray, K. MacLean, A. Dementyev, and S. Barrett. Intrinsic Origin of Spin Echoes in Dipolar Solids Generated by Strong π pulses. *Physical Review B*, **77**(21), 214306–26 (2008).
- [25] M. Mehring. *Principles of High-Resolution NMR in Solids*. Springer-Verlag, Berlin, 2nd edition (1983).
- [26] U. Haeberlen and J. Waugh. Coherent Averaging Effects in Magnetic Resonance. *Physical Review*, **175**(2), 453 (1968).
- [27] E. Hahn. Spin Echoes. *Physical Review*, **80**(4), 580 (1950).

- [28] H. Y. Carr and E. M. Purcell. Effects of Diffusion on Free Precession in Nuclear Magnetic Resonance Experiments. *Physical Review*, **94**(3), 630–638 (1954).
- [29] S. Meiboom and D. Gill. Modified Spin-Echo Method for Measuring Nuclear Relaxation Times. *Review of Scientific Instruments*, **29**(8), 688–691 (1958).
- [30] R. Freeman. *Spin Choreography: Basic Steps in High Resolution NMR*. Spektrum, Oxford (1997).
- [31] S. Watanabe and S. Sasaki. ^{29}Si Nuclear-Spin Decoherence Process Directly Observed by Multiple Spin-Echoes for Pure and Carrier-Less Silicon. *Jpn. J. Appl. Phys.*, **42**(Part 2, No. 11B), L1350–L1352 (2003).
- [32] M. B. Franzoni and P. R. Levstein. Manifestations of the Absence of Spin Diffusion in Multipulse NMR Experiments on Diluted Dipolar Solids. *Phys. Rev. B*, **72**(23), 235410 (2005).
- [33] E. Ostroff and J. Waugh. Multiple Spin Echoes and Spin Locking in Solids. *Physical Review Letters*, **16**(24), 1097 (1966).
- [34] M. M. Maricq. Thermodynamics for Many-Body Systems Evolving Under a Periodic Time-Dependent Hamiltonian: Application to Pulsed Magnetic Resonance. *Physical Review B*, **31**(1), 127–141 (1985).
- [35] M. M. Maricq. Equilibrium in Periodically Time-Dependent Two-Level Systems. *Physical Review Letters*, **56**(14), 1433–1436 (1986).
- [36] D. Suwelack and J. S. Waugh. Quasistationary Magnetization in Pulsed Spin-Locking Experiments in Dipolar Solids. *Physical Review B*, **22**(11), 5110–5114 (1980).

- [37] S. Hudgens, M. Kastner, and H. Fritzsche. Diamagnetic Susceptibility of Tetrahedral Semiconductors. *Physical Review Letters*, **33**(26), 1552–1555 (1974).
- [38] U. Haeberlen. *High Resolution NMR in Solids : Selective Averaging*, volume 1. Academic Press, New York (1976).
- [39] J. S. Waugh, C. Wang, L. Huber, and R. Vold. Multiple-Pulse NMR Experiments. *The Journal of Chemical Physics*, **48**(2), 662–670 (1968).
- [40] J. S. Waugh, L. Huber, and U. Haeberlen. Approach to High-Resolution NMR in Solids. *Physical Review Letters*, **20**(5), 180 (1968).
- [41] P. Mansfield and D. Ware. Nuclear Resonance Line Narrowing in Solids by Repeated Short Pulse R.F. Irradiation. *Physics Letters*, **22**(2), 133–135 (1966).
- [42] W.-K. Rhim, A. Pines, and J. S. Waugh. Violation of the Spin-Temperature Hypothesis. *Physical Review Letters*, **25**(4), 218–220 (1970).
- [43] W.-K. Rhim, A. Pines, and J. S. Waugh. Time-Reversal Experiments in Dipolar-Coupled Spin Systems. *Physical Review B*, **3**(3), 684–696 (1971).
- [44] W. Magnus. On the Exponential Solution of Differential Equations for a Linear Operator. *Communications on Pure and Applied Mathematics*, **7**(4), 649–673 (1954).
- [45] U. Haeberlen, J. E. Jr, and J. Waugh. Resonance Offset Effects in Multiple-Pulse NMR Experiments. *The Journal of Chemical Physics*, **55**(1), 53–62 (1971).
- [46] P. A. Heiney, J. E. Fischer, A. R. McGhie, W. J. Romanow, A. M. Denenstein, J. P. McCauley Jr., A. B. Smith, and D. E. Cox. Orientational Ordering Transition in Solid C₆₀. *Phys. Rev. Lett.*, **66**(22), 2911–2914 (1991).

- [47] R. Tycko, R. C. Haddon, G. Dabbagh, S. H. Glarum, D. C. Douglass, and A. M. Muzsice. Solid-State Magnetic Resonance Spectroscopy of Fullerenes. *The Journal of Physical Chemistry*, **95**(2), 518–520 (1991).
- [48] C. S. Yannoni, R. D. Johnson, G. Meijer, D. S. Bethune, and J. R. Salem. Carbon-13 NMR Study of the C60 Cluster in the Solid State: Molecular Motion and Carbon Chemical Shift Anisotropy. *The Journal of Physical Chemistry*, **95**(1), 9–10 (1991).
- [49] I. Solomon. Rotary Spin Echoes. *Physical Review Letters*, **2**(7), 301–302 (1959).
- [50] M. Lee and W. Goldburg. Nuclear-Magnetic-Resonance Line Narrowing by a Rotating rf Field. *Physical Review*, **140**(4A), A1261–A1271 (1965).
- [51] W. Goldburg and M. Lee. Nuclear Magnetic Resonance Line Narrowing by a Rotating rf Field. *Physical Review Letters*, **11**(6), 255–258 (1963).
- [52] K. Takegoshi and C. A. McDowell. A Magic Echo Pulse Sequence for the High-Resolution NMR Spectra of Abundant Spins in Solids. *Chemical Physics Letters*, **116**(2-3), 100 – 104 (1985).
- [53] A. Pines and J. Waugh. Quantitative Aspects of Coherent Averaging. Simple Treatment of Resonance Offset Processes in Multiple-Pulse NMR. *Journal of Magnetic Resonance*, **8**(4), 354–365 (1972).
- [54] S. Matsui. Solid-State NMR Imaging by Magic Sandwich Echoes. *Chemical Physics Letters*, **179**(1-2), 187–190 (1991).
- [55] Y. Wu, D. A. Chesler, M. J. Glimcher, L. Garrido, J. Wang, H. J. Jiang, and J. L. Ackerman. Multinuclear Solid-State Three-Dimensional MRI of Bone and Synthetic Calcium Phosphates. *Proceedings of the National Academy of Sciences of the United States of America*, **96**(4), 1574–1578 (1999).

- [56] Y. Wu, J. L. Ackerman, H.-M. Kim, C. Rey, A. Barrough, and M. J. Glimcher. Nuclear Magnetic Resonance Spin-Spin Relaxation of the Crystals of Bone, Dental Enamel, and Synthetic Hydroxyapatites. *Journal of Bone and Mineral Research*, **17**(3), 472–480 (2002).
- [57] J. Miller, D. Cory, A. Garroway, P. Mansfield, D. Greenslade, K. Packer, R. Far-rant, J. Strange, J. Frahm, and E. Hahn. Line-Narrowing Approaches to Solid State NMR Imaging: Pulsed Gradients and Second Averaging [and Discussion]. *Philosophical Transactions: Physical Sciences and Engineering*, **333**(1632), 413–426 (1990).
- [58] D. Demco and B. Blumich. Solid-State NMR Imaging Methods. Part II: Line Narrowing. *Concepts in Magnetic Resonance*, **12**(5), 269–288 (2000).
- [59] P. Glover and S. P. Mansfield. Limits to Magnetic Resonance Microscopy. *Reports on Progress in Physics*, **65**(10), 1489–1511 (2002).
- [60] P. Lauterbur. Image Formation by Induced Local Interactions: Examples Em-ploying Nuclear Magnetic Resonance. *Nature* (1973).
- [61] P. Mansfield and P. Grannell. NMR Diffraction in Solids. *Journal of Physics C: Solid State Physics*, **6**, L422–L426 (1973).
- [62] Y. Dong, R. Ramos, D. Li, and S. Barrett. Controlling Coherence Using the Internal Structure of Hard π Pulses. *Physical Review Letters*, **100**(24), 247601–4 (2008).
- [63] D. Demco and B. Bluemich. Solid-State NMR Imaging Methods. Part I: Strong Field Gradients. *Concepts in Magnetic Resonance*, **12**(4), 188–206 (2000).

- [64] T. L. Peck, R. L. Magin, and P. C. Lauterbur. Design and Analysis of Microcoils for NMR Microscopy. *Journal of Magnetic Resonance, Series B*, **108**(2), 114 – 124 (1995).
- [65] K. Yamauchi, J. W. G. Janssen, and A. P. M. Kentgens. Implementing Solenoid Microcoils for Wide-Line Solid-State NMR. *Journal of Magnetic Resonance*, **167**(1), 87 – 96 (2004).
- [66] D. Sakellariou, G. Goff, and J.-F. Jacquinot. High-Resolution, High-Sensitivity NMR of Nanolitre Anisotropic Samples by Coil Spinning. *Nature*, **447**(7145), 694–697 (2007).
- [67] W.-K. Rhim, D. D. Elleman, L. B. Schreiber, and R. W. Vaughan. Analysis of Multiple Pulse NMR in Solids. II. *The Journal of Chemical Physics*, **60**(11), 4595–4604 (1974).
- [68] M. Mehring and J. Waugh. Phase Transients in Pulsed NMR Spectrometers. *Review of Scientific Instruments* (2003).
- [69] A. J. Vega. Controlling the Effects of Pulse Transients and RF Inhomogeneity in Phase-Modulated Multiple-Pulse Sequences for Homonuclear Decoupling in Solid-State Proton NMR. *Journal of Magnetic Resonance* (2004).